NON-EQUILIBRIUM DYNAMICS OF ULTRACOLD ATOMS IN OPTICAL LATTICES

BY

DAVID CHEN

DISSERTATION

Submitted in partial fulfillment of the requirements
for the degree of Doctor of Philosophy in Physics
in the Graduate College of the
University of Illinois at Urbana-Champaign, 2015

Urbana, Illinois

Doctoral Committee:

Professor Paul Kwiat, Chair
Professor Brian DeMarco, Director of Research
Professor Lance Cooper
Associate Professor Smitha Vishveshwara

Abstract

This thesis describes experiments focused on investigating out-of-equilibrium phenomena in the Bose-Hubbard Model and exploring novel cooling techniques for ultracold gases in optical lattices.

In the first experiment, we study quenches across the Mott-insulator-to-superfluid quantum phase transition in the 3D Bose-Hubbard Model. The quench is accomplished by continuously tuning the ratio of the Hubbard energies. We observe that the degree of excitation is proportional to the fraction of atoms that cross the phase boundary, and that the amount of excitations and energy produced during the quench have a power-law dependence on the quench rate. These phenomena suggest an excitation process analogous to the mechanism for defect generation in non-equilibrium classical phase transitions. This experiment constitutes the first observation of the Kibble-Zurek mechanism in a quantum quench. We have reported our findings in Ref. [1].

In a second experiment, published in Ref. [2], we investigate dissipation as a method for cooling a strongly interacting gas. We introduce dissipation via a bosonic reservoir to a strongly interacting bosonic gas in the Mott-insulator regime of a 3D spin-dependent optical lattice. The lattice atoms are excited to a higher energy band using laser-induced Bragg transitions. A weakly interacting superfluid comprised of atoms in a state that does not experience the lattice potential acts as a dissipative bath that interacts with the lattice atoms through collisions. We measure the resulting bath-induced decay using the atomic quasimomentum distribution, and we compare the decay rate with predictions from a weakly interacting model with no free parameters. A competing intrinsic decay mechanism arising from collisions between lattice atoms is also investigated. The presence of intrinsic decay can not be accommodated within a non-interacting framework and signals that strong interactions may play a central role in the lattice-atom dynamics. The intrinsic decay process we observe may negatively impact the success of cooling via dissipation because a fraction of intrinsic decay events can deposit a large amount of energy into the lattice gas.

In a third experiment, we develop and carry out the first demonstration of cooling an atomic quasimomentum distribution. Our scheme, applied in a proof-of-principle experiment to 3D Bose-Hubbard gas in the superfluid regime, involves quasimomentum-selective Raman transitions. This experiment is motivated

by the search of new cooling techniques for lattice-trapped gases. Efficient cooling exceeding heating rates is achieved by iteratively removing high quasimomentum atoms from the lattice. Quasimomentum equilibration, which is necessary for cooling, is investigated by directly measuring rethermalization rates after bringing the quasimomentum distribution of the gas out of equilibrium. The measured relaxation rate is consistent at high lattice depths with a short-range, two-particle scattering model without free parameters, despite an apparent violation of the Mott-Ioffe-Regel bound. Our results may have implications for models of unusual transport phenomena in materials with strong interactions, such as heavy fermion materials and transition metal oxides. The cooling method we have developed is applicable to any species, including fermionic atoms. Our results are available in Ref. [3].

Acknowledgements

I am extremely grateful to my mentor Brian DeMarco for his academic guidance and support, for encouraging me to be a better experimentalist and communicator, and for giving me the freedom to learn from my mistakes.

It has also been a great pleasure to work with the other members of the DeMarco lab including Matthew White, Matthew Pasienski, Stanimir Kondov, David McKay, William McGehee, Joshua Zirbel, Carolyn Meldgin, Philip Russ, Wen-Chao Xu, Paul Koehring, William Morong, Pei-Wen Tsai, and Laura Wadleigh (in chronological order). Special thanks go to Matthew White for building most of the Rb apparatus from which I benefited, and to David McKay for his insight and advice, and whose enthusiasm for science has always been a source of inspiration. I would like to extend my gratitude to the entire physics community at UIUC for providing an exceptional work environment.

I was fortunate to start my journey in graduate school with Leonardo Sepulveda. I am thankful for his friendship and support throughout the years, which have made my life more enjoyable and colorful. I would like to thank Marcos Sotomayor for his hospitality upon my arrival in Urbana-Champaign. I am grateful for his constant academic advice and encouragement. I also want to thank Aditya Sharma for his friendship since the first day of class. I will never forget our trip in the Midwest and I hope there will be more trips to come.

Throughout graduate school, I have met many wonderful people outside the physics department who have truly enriched my life. I would like to thank the past and present members of the Chilean community in Urbana-Champaign. I also want to thank my friends from salsa dancing and Portuguese class. You all will be sorely missed.

I want to thank Evangeline Reynolds for bringing new joy into my life. She has been a continuous source of companionship and support. I thank her for her understanding and patience during long working hours in the lab. I am looking forward to having new adventures together!

Finally, I am grateful for generous financial support from the University of Illinois, NSF, ARO, and DARPA.

Table of Contents

List of Figures

List of Abbreviations

BEC	Bose-Einstein condensate
SF	Superfluid
MI	Mott insulator
BdG	Bogoliubov-de-Gennes
GPE	Gross-Pitaevskii equation
EOM	Electro-optic modulator
AOM	Acousto-optic modulator
TOF	Time of flight
KZM	Kibble-Zurek mechanism
BH	Bose-Hubbard
RF	Radio-frequency
RWA	Rotating-wave approximation
BZ	Brillouin zone
TWA	Truncated Wigner Approximation
1D, 2D, 3D	One, two and three-dimensional
MIR	Mott-Ioffe-Regel

List of Symbols

Numerical values of the fundamental constants are in S.I. units [4].

h	Planck's constant ($h = 6.626\ 069\ 57(29) \times 10^{-34}$ J s, $\hbar = h/2\pi$)
e	Elementary charge ($e = 1.602\ 176\ 565(35) \times 10^{-19}$ C)
m_e	Electron mass ($m_e = 9.109\ 382\ 91(40) \times 10^{-31}$ kg)
c	Speed of light ($c = 299792458$ m s^{-1})
μ_0	Magnetic permeability ($\mu_0 = 4\pi \times 10^{-7}$ N A^{-2})
ε_0	Electric permittivity ($\varepsilon_0 = 1/\mu_0 c^2 = 8.854\ 187\ 817 \times 10^{-12}$ F m^{-1})
k_B	Boltzmann constant ($k_B = 1.380\ 648\ 8(13) \times 10^{-23}$ J K^{-1})
a_0	Bohr radius ($a_0 = 4\pi\varepsilon_0\hbar^2/m_e e^2 = 0.529\ 177\ 210\ 92(17) \times 10^{-10}$ m)
μ_B	Bohr magneton ($\mu_B = e\hbar/2m_e = 927.400\ 968(20) \times 10^{-26}$ J T^{-1})
μ_N	Nuclear magnetic moment ($e\hbar/2m_p = 5.050\ 783\ 53(11) \times 10^{-27}$ J T^{-1})
α	Fine-structure constant ($\alpha = e^2/4\pi\varepsilon_0\hbar c = 7.297\ 352\ 569\ 8(24) \times 10^{-3}$)
g	s-wave scattering interaction parameter ($g = 100.4(1)\, a_0$ [5])
H	Hamiltonian
τ	Time
$\mathbf{r}, x, y, z$	Spatial coordinates
V	Volume
D	Spatial dimensionality
p, q	Momentum and quasimomentum
g	Gravitational acceleration
K	Kinetic energy
V	Potential energy
f	Frequency
ω	Angular frequency
Δ, δ	Frequency detuning

λ	Wavelength
k	Wavevector ($k = 2\pi/\lambda$)
$\mathbf{E}$	Electric field
$\mathbf{B}$	Magnetic field
$\mathcal{V}$	Voltage
$\mathcal{F}$	Fourier transform
$\mathcal{FFT}$	Fast Fourier transform
$\hat{a}^\dagger$ ($\hat{a}$)	Creation (annihilation) operator
T_c	Critical temperature for Bose-Einstein condensation
ν, z	Critical exponents
m	Atomic mass of ^{87}Rb
F (m_F)	Atomic hyperfine quantum number (hyperfine projection)
g_F	Lande g-factor
a_s	s-wave scattering length ($a_s = 98a_0$ for ^{87}Rb)
$\mathbf{d}$	Electric dipole
$\mathrm{E_R}$	Recoil energy ($\mathrm{E_R} = \hbar^2k^2/2m = \hbar^2\pi^2/2md^2$)
s	Lattice potential depth
d	Lattice spacing
N_s	Number of lattice sites
N	Number of particles
$\mathbb{n}$	Lattice filling (number of particles per lattice site)
$\mathbb{z}$	Coordination number
t	Hubbard tunneling energy
U	Hubbard interaction energy
E_{bg}	Bandgap
w	Wannier function
q_B	Quasimomentum constant ($q_B = \hbar\pi/d$)
λ_R	Raman/Bragg beams wavelength
Ω	Coupling strength (Rabi rate)
T	Temperature
λ_T	De Broglie thermal wavelength ($\lambda_T = h/\sqrt{2\pi m k_B T}$)
z	Fugacity ($z = e^{\mu/k_BT}$)
μ	Chemical potential
β	Thermodynamic beta ($\beta = 1/k_BT$)

Chapter 1

Introduction

Despite the success of quantum statistical mechanics to describe equilibrium states, little is known about dynamics in strongly correlated systems. How do open and closed quantum many-body systems reach equilibrium? How do these systems thermalize given that they comprise a large number of degrees of freedom? These questions were posed many decades ago, but most have remained largely unsolved. It was not until relatively recently that they have re-gained momentum thank to the immense progress in experimental techniques and advances in theoretical methods [6].

The standard approach to understanding many-body systems involves simplified models that are believed to reproduce the relevant interactions responsible for the observed physics. Given a specific model, one traditionally relies on numerical methods to determine their properties (with the exception of a few cases that are exactly solvable) [7]. However, the Hilbert space of many-body systems is a really big place! For example, for a system of N spin-1/2 particles, the dimension of the Hilbert space is 2^N, which is exponentially large in the number of states and already intractable at $N \sim 50$ by a classical computer. Furthermore, complexity in strongly correlated systems still remains poorly understood [8]. Several numerical methods have been developed to solve these problems, but all the existing techniques have their own limitations. For example, mean field theories fail at describing effects of quantum correlation [9], tensor network methods for one-dimensional (1D) systems (e.g. density matrix renormalization group) are efficient only for short times [10], and quantum Monte Carlo methods for static fermionic systems suffer from the sign problem.

Fortunately, experiments in optical lattices have enabled the possibility of investigating static and dynamical properties in strongly correlated systems by creating well understood quantum systems with microscopic parameters and controlled initial conditions [11–17]. In particular, optical lattices can almost ideally realize the Bose-Hubbard and Fermi-Hubbard Hamiltonians [18], which are minimal models of electronic solids that exhibit many-body quantum effects. For examples, the Mott-insulator (MI) phase has been observed for bosonic and fermionic atoms in 3D lattices [19–21], Anderson and many-body localization have been detected in disordered lattices [22, 23], interaction has been studied in Bose-Fermi mixtures [24], antiferromagnetic ordering has been achieved in 1D pseudo-spin chains, 2D dimerized lattices [25, 26], and 3D simple

cubic lattices [27], and quantum criticality in a superfluid-MI transition has been measured via atomic gas microscopy [28, 29].

A particular topic that has recently become a focus of attention is quantum phase transitions [30], which have important fundamental and practical implications (e.g. for adiabatic quantum computing [31]). A key theoretical model for understanding the dynamics of quantum phase transitions has been provided by the Kibble-Zurek mechanism (KZM) [32–35]. The KZM predicts scaling laws for defect generation in classical and quantum phase transitions moving from a gapped phase to criticality. In Chapter 3, I describe how we captured, for the first time, the KZM in a quantum quench and how we investigated the scaling laws predicted by this mechanism.

Another interesting topic on its own is how strongly correlated systems relax and thermalize toward equilibrium. Studies have been done on correlation dynamics in a quenched MI in 1D [36, 37], equilibration dynamics in a tilted lattice in a 1D Ising chain [38, 39], and lattice transport in interacting bosonic and fermionic gases in 1D, 2D, and 3D [40, 41]. In Chapter 5, I present the first thermalization measurement in a strongly correlated 3D atomic gas. Interestingly, we find a discrepancy with predictions based on weakly interacting physics, which may be evidence of an effect analogue to the non-Fermi liquid behavior in strongly correlated fermionic systems [42]. Understanding the origin of such breakdown is an outstanding challenge in strongly correlated physics.

Despite the wide success of optical lattices as quantum simulators, ultra-low entropy regimes are still out of reach and, consequently, more complex quantum phases, such as spin liquids in frustrated geometries and the Néel state in the Fermi-Hubbard Hamiltonian at half filling, are currently unrealizable. The latter example is of particular importance for investigating high-T_c superconductivity [43,44], since it is conjectured that a doped Néel state [45] (realizable in a Fermi gas by creating an initial spin imbalance) undergoes a quantum phase transition to a d-wave superconducting state [46]. Currently, temperatures below the bandwidth of the ground band and the interaction energy U are routinely achieved. The next lower energy scale is set by the superexchange energy t^2/U (associated with virtual tunneling processes) [18]. For ^{87}Rb, magnetically ordered states in the MI are expected to arise at temperatures around 100–200 pK [47], which is significantly below the temperatures presently accessible in ultracold atoms. On the other hand, for a fermionic gas, the estimated temperature needed to observe antiferromagnetic and d-wave superfluidity is $T/T_F \sim 0.01$ (T_F is the Fermi temperature of the trapped gas) [46], and numerical simulations predict a Néel temperature of $T_{\text{Néel}}/t \approx 0.3$ and a critical entropy of $S_{\text{Néel}} \approx 0.3\,k_B$ [48]. These value, even though small, are close to being achieved in current experiments, in which incipient short-range magnetic ordering has been observed [27].

Several cooling schemes have been suggested as new routes to reach lower temperatures and entropies in optical lattices. For example, it has been proposed to selectively address and remove defects in the lattice [49], or to localize regions of low entropy and isolate them from the rest of the system [49–55]. Experimental demonstrations, however, have been scarce [56, 57]. In Chapter 4, I explore the method proposed in Refs. [58,59] to perform cooling through dissipation. This so-called "immersion" cooling consists of a low entropy, dissipative bath that interacts with a strongly correlated gas and carries entropy away as excitations.

Motivated by the search of new cooling methods, in Chapter 5 I discuss a novel cooling technique that we have developed which works for any atomic species. The scheme uses stimulated Raman excitation to selectively remove atoms with high kinetic energy from a strongly correlated atomic gas. In a proof-of-principle experiment, we demonstrate quasimomentum-selective Raman cooling as a method to reduce the temperature and entropy of a strongly correlated bosonic gas. This promising technique may pave the way towards realization of exotic quantum states that may exist at low entropies [60–65].

This thesis is organized as follows. In the remaining sections of this chapter, I will give a brief overview of our ^{87}Rb apparatus. Chapter 2 introduces the implementation of an optical system for driving stimulated Raman and Bragg excitations in ultracold atomic gases. Chapters 3 to 5 report three different experiments. Chapter 3 describes the observation of excitation generation in a quantum quench. Chapter 4 explores dissipation effects in an open strongly correlated atomic gas. Chapter 5 presents measurements on thermalization and cooling in a strongly correlated atomic gas.

1.1 Apparatus Overview

The experiments reported in this thesis were performed using a ^{87}Rb apparatus that is thoroughly described in Ref. [66]. In this section, I briefly present a few aspects of the apparatus relevant to this thesis.

1.1.1 Optical and Magnetic Traps

We start our experiments with the preparation of a ^{87}Rb Bose-Einstein condensate (BEC) in the $|F = 1, m_F = -1\rangle$ hyperfine state with $\sim 10^5$ atoms and $T_c \sim 100$ nK. For experiments with spin mixtures (Chapter 4), we use an adiabatic rapid passage driven by a radio-frequency magnetic field to partially transfer atoms to a different magnetic state m_F. In this thesis, two different trap configurations are employed. The first configuration is a hybrid trap formed by an optical trap superimposed on a magnetic trap. The second configuration consists of a purely optical trap formed by two crossing laser beams. The advantage of using

an all-optical trap over a hybrid trap is in its capability of trapping atoms of arbitrary magnetic states m_F. In Chapter 3, I discuss experiments performed in the hybrid trap, whereas in Chapters 4 and 5, I discuss experiments carried out in the crossed trap. The experiments presented in this thesis are performed in traps with geometric mean of the trap frequencies $\bar{\omega}$ in the range $2\pi \times (40 - 75)$ Hz (the traps provide approximately harmonic confinement).

The hybrid trap is formed by an optical dipole trap superimposed on a quadrupole magnetic trap [67]. The dipole trap mainly provides radial confinement, whereas the magnetic trap provides axial confinement. The optical dipole trap is generated from a fiber laser (IPG Photonics YLR-20-1064-LP) which provides 20W, 1064 nm, single mode, multi-frequency, linearly polarized light. The light field has a gaussian intensity profile in the form

$$I(x, y, z) = \frac{2P}{\pi \mathrm{w}(z)^2} e^{-\frac{2(x^2+y^2)}{\mathrm{w}^2(z)}}, \tag{1.1}$$

where z is the direction of light propagation, P is the beam power, $\mathrm{w}(z) = \mathrm{w}_0[1 + (z/z_0)^2]^{1/2}$ is the beam waist, $z_0 = \pi \mathrm{w}_0^2/\lambda$ is the Rayleigh length, w_0 is the beam waist at $z = 0$, and λ is the wavelength. The light intensity is regulated using a servo-controlled acousto-optic modulator[1] (AOM). The laser light interacts with the induced electric dipole moment of the atoms through the potential [68–72]

$$V_{\mathrm{d}}(x, y, z) = -\frac{\pi c^2 I(x, y, z)}{2} \left[\frac{2\Gamma_{3/2}}{\omega_{3/2}^3} \left(\frac{1}{\omega_{3/2} - \omega} + \frac{1}{\omega_{3/2} + \omega} \right) + \frac{\Gamma_{1/2}}{\omega_{1/2}^3} \left(\frac{1}{\omega_{1/2} - \omega} + \frac{1}{\omega_{1/2} + \omega} \right) \right] \tag{1.2}$$

where $I(x, y, z)$ is given by Eq. 1.1, ω is the laser frequency, $\Gamma_{1/2}$ and $\Gamma_{3/2}$ are the natural linewidths of the electronic transitions D_1 and D_2, respectively, and $\omega_{1/2}$ and $\omega_{3/2}$ are the corresponding resonance frequencies (Fig. 1.1). The spontaneous scattering rate associated with the optical radiation is

$$\Gamma_{\mathrm{D}} = \frac{\pi c^2 \omega^3 I(x, y, z)}{2\hbar} \left[\frac{2\Gamma_{3/2}^2}{\omega_{3/2}^6} \left(\frac{1}{\omega_{3/2} - \omega} + \frac{1}{\omega_{3/2} + \omega} \right)^2 + \frac{\Gamma_{1/2}^2}{\omega_{1/2}^6} \left(\frac{1}{\omega_{1/2} - \omega} + \frac{1}{\omega_{1/2} + \omega} \right)^2 \right]. \tag{1.3}$$

When the laser is far detuned from the D_1 and D_2 transitions (which is the case of 1064 nm light), the counter-rotating terms $1/(\omega_{3/2} + \omega)$ and $1/(\omega_{1/2} + \omega)$ in Eqs. 1.2 and 1.3 are not negligible.

The magnetic field is generated by quadrupole coils in an anti-Helmholtz configuration. In order to characterize the magnetic field, it is convenient to define the coordinate basis $\{\hat{x}_1, \hat{x}_2, \hat{x}_3\}$ shown in Fig. 1.2, where $\hat{x}_1$ lies along the imaging axis and $\hat{x}_2$ points in the opposite direction of gravity. In this basis, the

[1] AOMs use a traveling RF acoustic wave in a crystal to diffract an incoming beam. They are utilized throughout the apparatus to control light intensity (by changing the RF power), to steer beams (by changing the RF frequency), and to shift the frequency of beams (via diffraction from the traveling wave, which results in a Doppler shift).

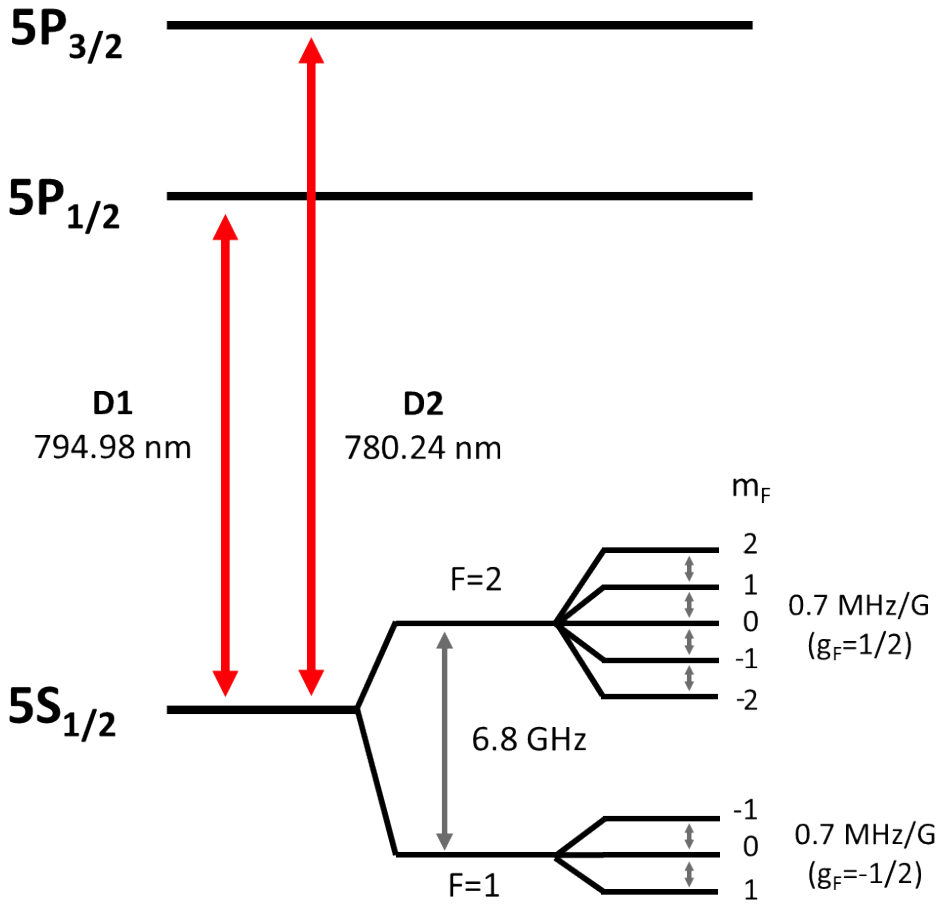

Figure 1.1: Fine and hyperfine energy levels in ^{87}Rb relevant to this thesis (not to scale). The value 0.7 MHz/G represents the Zeeman splitting. Details can be found in Ref. [73].

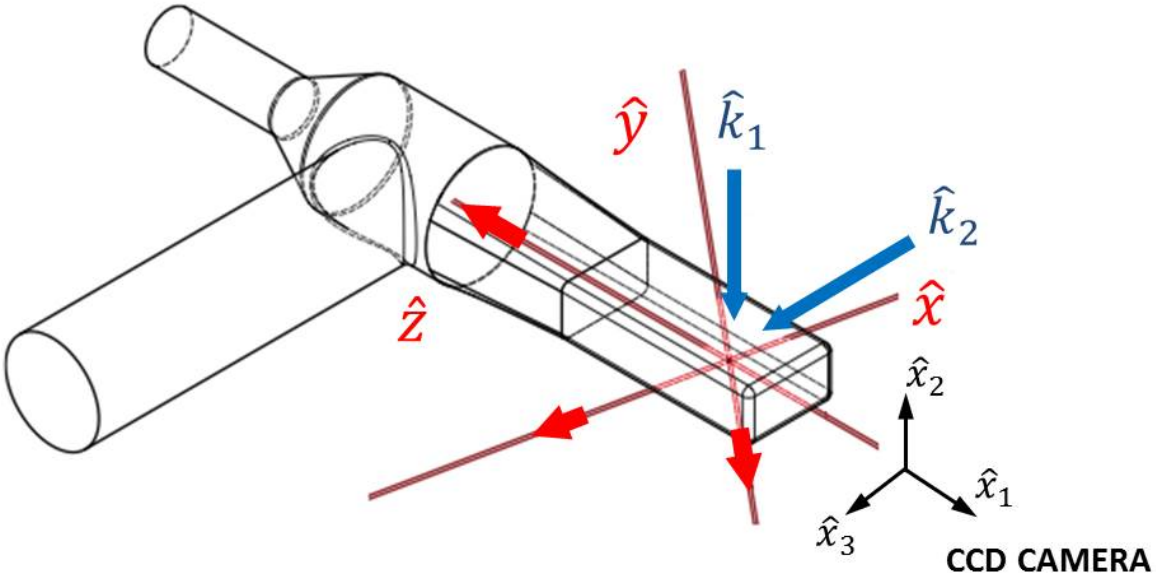

Figure 1.2: Atomic chamber. The imaging axis is parallel to $\hat{x}_1$ and gravity points in the $-\hat{x}_2$ direction. None of the three lattice directions $\hat{x}$, $\hat{y}$, and $\hat{z}$ (red lines) are parallel to the imaging axis. Projection of the lattice wavevectors onto the imaging plane are shown in Fig. 1.5. The red arrows indicate the sign convention for the lattice wavevectors used throughout this thesis. The blue arrows show the Raman beams (described in Chapter 2), which propagate along $\hat{k}_1 = -\hat{x}_2$ and $\hat{k}_2 = \hat{x}_3$, and their wavevector difference lies along $\hat{z}$. Figure adapted from Ref. [66].

magnetic field is expressed as

$$\mathbf{B}(x_1, x_2, x_3) = B_0 \left(\frac{x_1}{2}\hat{x}_1 + \frac{x_2 - x_2'}{2}\hat{x}_2 + -x_3\hat{x}_3 \right), \tag{1.4}$$

where the zero of the field is offset a distance $x_2' \approx 100$ μm above the overall trap center to suppress Majorana losses [74]. Atoms interact with this field through the potential

$$V_{\mathrm{QP}}(x_1, x_2, x_3) = m_F g_F \mu_B |\mathbf{B}(x_1, x_2, x_3)|, \tag{1.5}$$

where m_F is the projection of the total atomic spin F onto the quantization axis, g_F is the Lande g-factor, and $\mu_B = e\hbar/2m_e$ is the Bohr magneton.

The laser beam for the optical dipole trap propagates along the $-(\hat{x}_1 + \hat{x}_3)$ direction. The total potential acting on the atoms, including gravity and the magnetic trap, is therefore

$$V_{\mathrm{trap}}(x_1, x_2, x_3) = V_{\mathrm{d}} \left(x_2, \frac{x_1 - x_3}{\sqrt{2}}, -\frac{x_1 + x_3}{\sqrt{2}} \right) + V_{\mathrm{QP}}(x_1, x_2, x_3) + mgx_2, \tag{1.6}$$

with $V_{\mathrm{d}}(x, y, z)$ given by Eq. 1.2

In the crossed configuration, the laser is double passed though the atomic chamber. The forward and crossed beams lie in the horizontal plane and intersect in approximately 90°[2]. The total trap potential is given by

$$V_{\mathrm{trap}}(x_1, x_2, x_3) = V_{\mathrm{d}} \left(x_2, \frac{x_1 - x_3}{\sqrt{2}}, -\frac{x_1 + x_3}{\sqrt{2}} \right) + V_{\mathrm{d}} \left(x_2, -\frac{x_1 + x_3}{\sqrt{2}}, \frac{x_3 - x_1}{\sqrt{2}} \right) + mgx_2, \tag{1.7}$$

where $V_{\mathrm{d}}(x, y, z)$ is defined in Eq. 1.2. Because of gravity, atoms sit below the intersection point of the two beams. The position of the gas can be estimated by minimizing Eq. 1.7 under the harmonic approximation $I(x, y, z) = 2P/\pi \mathrm{w}_0^2[1 - 2(x^2 + y^2)/\mathrm{w}_0^2]$ (since $x, y, z \ll \mathrm{w}_0$), which results in a vertical offset of $mg\mathrm{w}_0^2/8V_{\mathrm{d}}$. Under the same harmonic approximation, the trap frequencies are $\omega \approx \sqrt{-8V_{\mathrm{d}}/m\mathrm{w}_0^2}$ in the vertical direction and $\omega \approx \sqrt{-4V_{\mathrm{d}}/m\mathrm{w}_0^2}$ in the two horizontal directions.

A magnetic field ranging from a few G to 60 G is generally present during the experiments to suppress spin exchange. The Zeeman shift induced by the magnetic field can be calculated using the Breit-Rabi Formula [76].

[2]For this thesis, the beam configuration, described in Refs. [66, 72, 75], was modified in two ways. The laser beam path was shortened to enhance the point stability of the trap, and the crossed beam was translated to the horizontal plane to improve the optical transmittance through the atomic chamber. The beam alignment was performed according to the procedure detailed in Refs. [66, §2.12.3] and [72, §C.7].

1.1.2 Optical Lattice

After creating a BEC, we slowly superimpose a simple cubic optical lattice onto the hybrid or crossed dipole trap. The lattice potential is formed by three mutually orthogonal, near infrared, linearly polarized, gaussian laser beams which are retro-reflected using gold mirrors [66]. The spatial configuration of the beams relative to the atomic chamber is illustrated in Fig. 1.2. The lattice vectors $\hat{x}, \hat{y}$, and $\hat{z}$ are expressed in terms of the coordinate system $\{\hat{x}_1, \hat{x}_2, \hat{x}_3\}$ shown in Fig. 1.2 as

$$\begin{aligned} \hat{x} &= -\frac{\hat{x}_1}{\sqrt{2}} - \frac{\hat{x}_2}{2} + \frac{\hat{x}_3}{2} \\ \hat{y} &= \frac{\hat{x}_1}{\sqrt{2}} - \frac{\hat{x}_2}{2} + \frac{\hat{x}_3}{2} \\ \hat{z} &= \frac{\hat{x}_2}{\sqrt{2}} + \frac{\hat{x}_3}{\sqrt{2}}. \end{aligned} \tag{1.8}$$

Details of the implementation of the optical lattice are addressed in Refs. [66, 72].

A single lattice laser with its retro-reflected beam (Fig. 1.3) creates an intensity and polarization gradient potential of the form [72, §C.2]

$$\begin{aligned} V_{\text{lat}}(\mathbf{r}) = -2\frac{\pi c^2}{2} I_0 \Bigg[&\left(\frac{2\Gamma_{3/2}}{\omega_{3/2}^3} \frac{1}{\omega_{3/2} - \omega} + \frac{\Gamma_{1/2}}{\omega_{1/2}^3} \frac{1}{\omega_{1/2} - \omega} \right) [1 + \cos(\theta)\cos(2\mathbf{k}\cdot\mathbf{r})] + \\ &+ g_F m_F \left(\frac{\Gamma_{3/2}}{\omega_{3/2}^3} \frac{1}{\omega_{3/2} - \omega} - \frac{\Gamma_{1/2}}{\omega_{1/2}^3} \frac{1}{\omega_{1/2} - \omega} \right) (\hat{k}\cdot\hat{B}) \sin(\theta)\sin(2\mathbf{k}\cdot\mathbf{r}) \Bigg], \end{aligned} \tag{1.9}$$

where $\mathbf{k}$ is the forward-going wavevector, $I_0 = 2P/(\pi \mathrm{w}_0^2)$ is the light intensity, P is the light power, F and m_F are the atomic hyperfine quantum numbers, θ is the relative polarization angle between the forward-going and the retro-reflected beams, g_F is the Lande g-factor, and $\hat{B}$ is a unitary vector along the quantization magnetic field. The counter-rotating terms in Eq. 1.9 have been ignored, since their contribution to the potential is negligible at the laser wavelengths 790 nm and 812 nm used in this thesis. The second line on the right side of Eq. 1.9 is proportional to m_F, which implies that atoms with different spin states m_F experience a different lattice potential. We refer to this potential as a spin-dependent lattice. The dependence on m_F arises because light couples the atomic ground and excited electronic states with different strength depending on the atomic spin state and light polarization. In contrast, the first line on the right side of Eq. 1.9 is spin-independent, which means that all the spin states interact with the same potential. The ratio between the spin-dependent and spin-independent components is determined by the relative polarization angle θ. We experimentally modify θ using a quarter waveplate positioned in front of each mirror, as shown in Fig. 1.3.

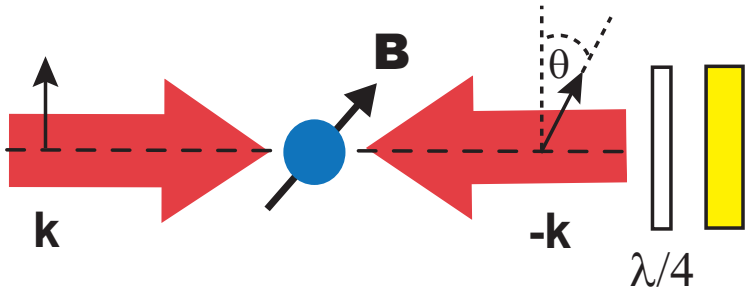

Figure 1.3: Optical lattice generation. Each linearly polarized lattice beam is retro-reflected using a gold mirror (yellow). The polarization of the retro-reflected beam can be rotated in θ using a quarter waveplate ($\lambda/4$) to form a spin-dependent lattice. The magnetic field **B** defines the quantization axis for the atomic gas (blue).

In the experiments presented in Chapters 3 and 5, we use optical lattices in the spin-independent configurations ($\theta = 0°$). In the experiments performed in Chapter 4, we employ a spin-dependent lattice ($\theta = 90°$) to form a spin mixture of a lattice-confined spin state in thermal contact with a different spin state that does not interact with the lattice potential.

The energy transferred to the atomic gas per unit time due to spontaneous scattering from the lattice beams is given by

$$\dot{E} = 4\mathrm{E_R}\Gamma, \tag{1.10}$$

where Γ is given by Eq. 1.3 [77]. This rate is independent of m_F, g_F, θ and the direction of the quantization field. Understanding heating of a strongly correlated lattice gas is an outstanding problem [78].

1.1.3 Band Structure

The superposition of three mutually orthogonal potentials in the form of Eq. 1.9 creates a simple 3D cubic lattice. The frequency of each lattice beam is slightly offset to prevent effects from interference between orthogonal beams[3]. The total lattice potential for any particular m_F state can be express as (ignoring the overall energy offset and phase shift)

$$V_{\mathrm{lat}}(\mathbf{r}) = s \sum_{i=x,y,z} \cos^2(kx_i) \tag{1.11}$$

where $k = 2\pi/\lambda = \pi/d$ is the wavevector of the lattice beams, λ is the wavelength, $d = \lambda/2$ is the lattice spacing, and s is the lattice depth (which is usually expressed in units of the photon recoil energy $\mathrm{E_R}$).

[3]The frequency shifts for the lattice beams $\hat{x}, \hat{y}$, and $\hat{z}$ are 80 MHz, -80 MHz, and 100 MHz, respectively.

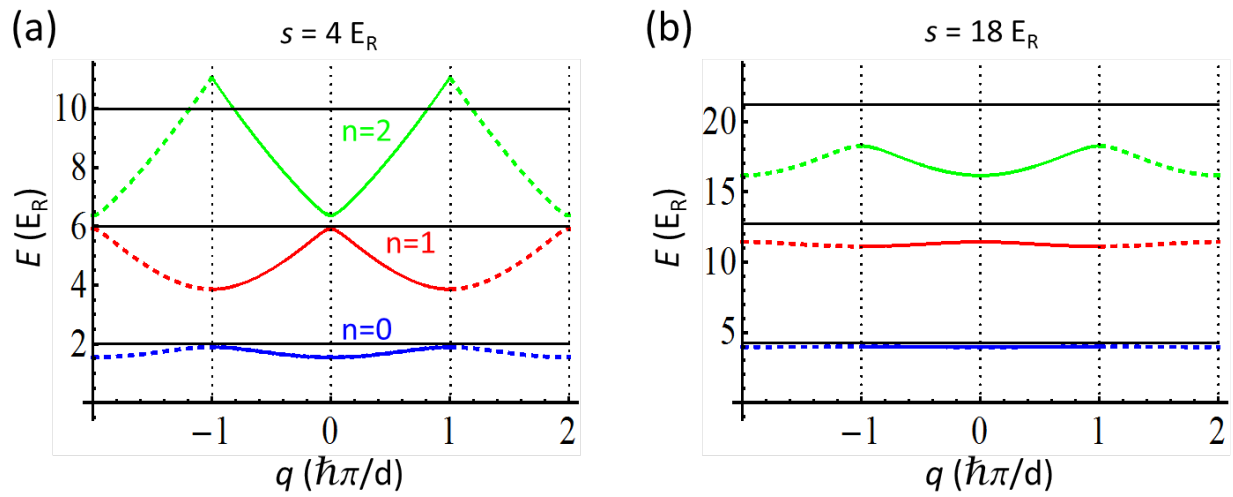

Figure 1.4: Energy bands in 1D induced by the lattice potential 1.11 at (a) $s = 4\ \mathrm{E_R}$ and (b) $s = 18\ \mathrm{E_R}$. Only the ground ($n = 0$), first-excited ($n = 1$) and second-excited ($n = 2$) bands are shown over the first (solid) and second (dotted) Brillouin zones. At low lattice depths ($s \sim 4\ \mathrm{E_R}$), difference in curvature between bands enables quasimomentum-selective Raman transitions (Chapter 2). The black horizontal lines indicate the energy levels treating each site as a harmonic well.

The Schrödinger equation with the potential 1.11 leads to a single-particle solution with energy bands $\epsilon_n(\mathbf{q})$ and Bloch states $\phi_{n,\mathbf{q}}(\mathbf{r})$, where $\mathbf{q}$ is quasimomentum, and n is the band index [19, 66, 72, 79]. Energy bands in 1D for $s = 4\ \mathrm{E_R}$ and $s = 18\ \mathrm{E_R}$ are shown in (a) and (b) of Fig. 1.4, respectively. At low lattice depths ($\sim 4\ \mathrm{E_R}$), the gap between bands (or bandgap) depends on the quasimomentum state $\mathbf{q}$, as shown in (a). In Chapter 5, we employ such quasimomentum dependence of the bandgap to perform quasimomentum-selective Raman excitation; this technique is introduced in Chapter 2. In the deep lattice limit, the energy bands become flat, since each lattice site resembles a harmonic oscillator, as shown in (b). However, due to anharmonicity of the lattice potential, the bands remain unequally spaced even for very deep lattices. This observation has important implications for the band decay experiment in Chapter 4, since it implies that weakly interacting particles in the first-excited band can not experience two-body collisions at high lattice depths because of energy conservation.

Beyond a single-particle picture, second quantization is used to describe many-body systems. The second-quantized representation of an interacting gas in a 3D cubic lattice-plus-parabolic potential is given by

$$\hat{H} = -t \sum_{\langle i,j \rangle} \hat{a}_i^\dagger \hat{a}_j + \frac{U}{2} \sum_i \hat{n}_i(\hat{n}_i - 1) + \sum_i (\varepsilon_i - \mu)\hat{n}_i, \tag{1.12}$$

which is known as the the Bose-Hubbard (BH) Hamiltonian [13, 18, 80]. Here, i and j index the lattice sites, $\langle i, j \rangle$ stands for nearest-neighbor sites, $\hat{a}_i$ and $\hat{a}_i^\dagger$ are the annihilation and creation operators, respectively,

$\hat{n}_i = \hat{a}_i^\dagger \hat{a}_i$ is the particle number operator, μ is the chemical potential, t is the tunneling energy between neighbor sites

$$t = -\int d^3r\, w_{\mathbf{R}}^*(\mathbf{r}) \left[-\frac{\hbar^2}{2m}\nabla^2 + V_{\text{lat}}(\mathbf{r}) \right] w_{\mathbf{R}+d\,\hat{x}}(\mathbf{r}), \tag{1.13}$$

d is the lattice spacing, U is the on-site interaction energy

$$U = \frac{4\pi\hbar^2 a_s}{m} \int d^3r\, |w_{\mathbf{R}}(\mathbf{r})|^4, \tag{1.14}$$

a_s is the s-wave scattering length, m is the atomic mass, $\varepsilon_i = V_{\text{trap}}(\mathbf{r}_i)$ is the local energy offset that arises from the overall external parabolic confinement, and $w_{\mathbf{R}}(\mathbf{r})$ are the Wannier wavefunctions localized at the lattice site $\mathbf{R}$. We have restricted ourselves to the lowest band (i.e., $n = 0$ only), since higher bands are typically frozen out in the ultracold regime. The Wannier wavefunctions are defined as

$$w_{n,\mathbf{R}}(\mathbf{r}) = \frac{1}{\sqrt{N_s}} \sum_{\mathbf{q}\,\in\,1\text{BZ}} e^{-i\mathbf{q}\cdot\mathbf{R}/\hbar} \phi_{n,\mathbf{q}}(\mathbf{r}), \tag{1.15}$$

where n is the band index [81].

For a non-interacting gas in the ground band, the second-quantized Hamiltonian leads to the tight-binding dispersion

$$\epsilon_0(\mathbf{q}) = 2t \sum_{i=x,y,z} \left[1 - \cos\left(\pi \frac{q_i}{q_B} \right) \right], \tag{1.16}$$

where t is the tunneling energy defined in Eq. 1.13, q_i is quasimomentum in the lattice direction i, and $q_B = \hbar\pi/d$. This equation is derived in Appendix D.

1.1.4 Overall Harmonic Confinement

In the lattice potential 1.9, the gaussian profile of the lattice beams were approximated as plane waves. This is a good approximation on the length scale of the lattice spacing, since the size of the atomic gas is usually much smaller than the beam waist (≈ 120 μm). For example, 20 μm off-center, the lattice depth is 5% less than in the middle. In terms of the Hubbard parameters t and U (Eq. 1.12), a 5% decrease in lattice depth corresponds to a $\approx 10\%$ increase in t and a 2% decrease in U. By contrast, on the length scale of the entire gas size, the gaussian shape of each lattice beam gives rise to an additional gaussian potential transverse to the direction of propagation $\mathbf{k}$. This additional potential alters the gas density, and therefore, must be considered.

The gaussian potential could be confining or de-confining depending on the sign of Eq. 1.9 [19, 72]. If

Eq. 1.9 is positive, the additional harmonic confinement from a cubic lattice is

$$\omega_{\mathrm{lat}}^2 = \frac{8s}{\mathrm{w}^2 m}\left(1 - \frac{1}{2\sqrt{s/\mathrm{E_R}}}\right), \tag{1.17}$$

where w is the beam waist, s is the lattice depth, and $\mathrm{E_R} = \hbar^2 k^2/2m$ is the photon recoil energy. If Eq. 1.9 is negative, the de-confining potential is instead

$$\omega_{\mathrm{lat}}^2 = -\frac{4}{\mathrm{w}^2 m}\sqrt{s/\mathrm{E_R}}. \tag{1.18}$$

As an example, in ^{87}Rb at $\lambda = 812$ nm and $\theta = 0°$, the confining potential from the lattice beams is $\omega_{\mathrm{lat}}/2\pi \approx 30$ Hz at $s = 5$ $\mathrm{E_R}$ and $\omega_{\mathrm{lat}}/2\pi \approx 60$ Hz at $s = 18$ $\mathrm{E_R}$, which are comparable to the frequencies of the dipole trap

The confining (or de-confining) frequency ω_{lat} must be added in quadrature to the dipole trap frequency $\bar{\omega}_0$, namely [72, §D]

$$\bar{\omega} = \sqrt{\bar{\omega}_0^2 + \omega_{\mathrm{lat}}^2}. \tag{1.19}$$

1.1.5 Time-of-Flight Imaging

In order to image the ultracold gas with enough resolution (the gas has typically an in-trap size of ~ 10 μm and our imaging system has a resolution of ≈ 3 μm/pix), all the confining potentials are quickly turned off and the gas is allowed to freely expand (typically for 20 ms) for subsequent absorption imaging [66]. Absorption imaging is a destructive technique, and therefore, a full experimental sequence has to be repeated every time a measurement is performed.

In the particular case of a harmonically-trapped BEC, the gas density has a bimodal distribution with a Thomas-Fermi profile for the condensed component and a Bose-Einstein distribution for the thermal atoms [71]. The Thomas-Fermi profile is given by

$$n\left(x, y, z\right) = n_0\left(1 - \frac{x^2}{\sigma_x^2} - \frac{y^2}{\sigma_y^2} - \frac{z^2}{\sigma_z^2}\right), \tag{1.20}$$

where n_0 is the peak density. During time of flight (TOF), it has been shown that free expansion rescales the width of the Thomas-Fermi profile [82]. On the other hand, TOF imaging reveals the momentum distribution of the thermal component, since the in-trap wavefunction $\Psi(\mathbf{r})$ of a single particle evolves in time under a

ballistic approximation as [83]

$$\Psi(\mathbf{p},\tau) = \left(\frac{m}{2\pi i\hbar\tau}\right)^{3/2} e^{im\mathbf{r}^2/2\hbar\tau} \int d^3r'\ \Psi(\mathbf{r}')e^{-i\mathbf{p}\cdot\mathbf{r}'/\hbar}, \tag{1.21}$$

which represents the Fourier transform of $\Psi(\mathbf{r}')$ with $\mathbf{p} = m\mathbf{r}/\tau$. Even though this result is only valid in the single-particle picture, information about many-body states can be extracted from higher order correlations in the momentum distribution [84].

In the quench experiment presented in Chapter 3, long expansion times (~ 50 ms) are required to resolve quasiparticle excitations and topological defects in the gas. We therefore employ a magnetic field gradient to hold the gas against gravity. This magnetic field is also used in Chapter 4 to separate different spin components for individual imaging.

1.1.6 Bandmapping

Immediately before releasing the gas from the trap for TOF imaging, we ramp down the lattice potential adiabatically with respect to its vibrational frequencies to avoid exciting atoms to higher bands, but quickly compared with h/t such that the population in each band is conserved. This procedure is called "bandmapping", and it is used to image the quasimomentum distribution of the lattice-confined gas by projecting it onto free particle states [19]. In this thesis, we are mostly interested in imaging atoms in the ground and first-excited bands which, after bandmapping, appear in the first and second Brillouin zones (BZ), respectively. Atoms in higher excited bands appear outside the second BZ.

Part (a) of Fig. 1.5 shows the reciprocal space of a 3D simple cubic lattice. The red and blue dots indicate nearest-neighbor and next-nearest-neighbor points with respect to the origin. The solid black cube is the first BZ, and the dashed lines indicate the second BZ. Atoms promoted to the first-excited band along the lattice direction $\hat{z}$ appear inside the shaded areas after bandmapping, as we experimentally observe in Chapters 4 and 5. Figure (b) shows the reciprocal lattice projected onto the imaging plane. Quasimomentum redistribution during bandmapping can lead to systematic errors in the condensate fraction and in the quasimomentum population close to the edge of the Brillouin zones [85, 86].

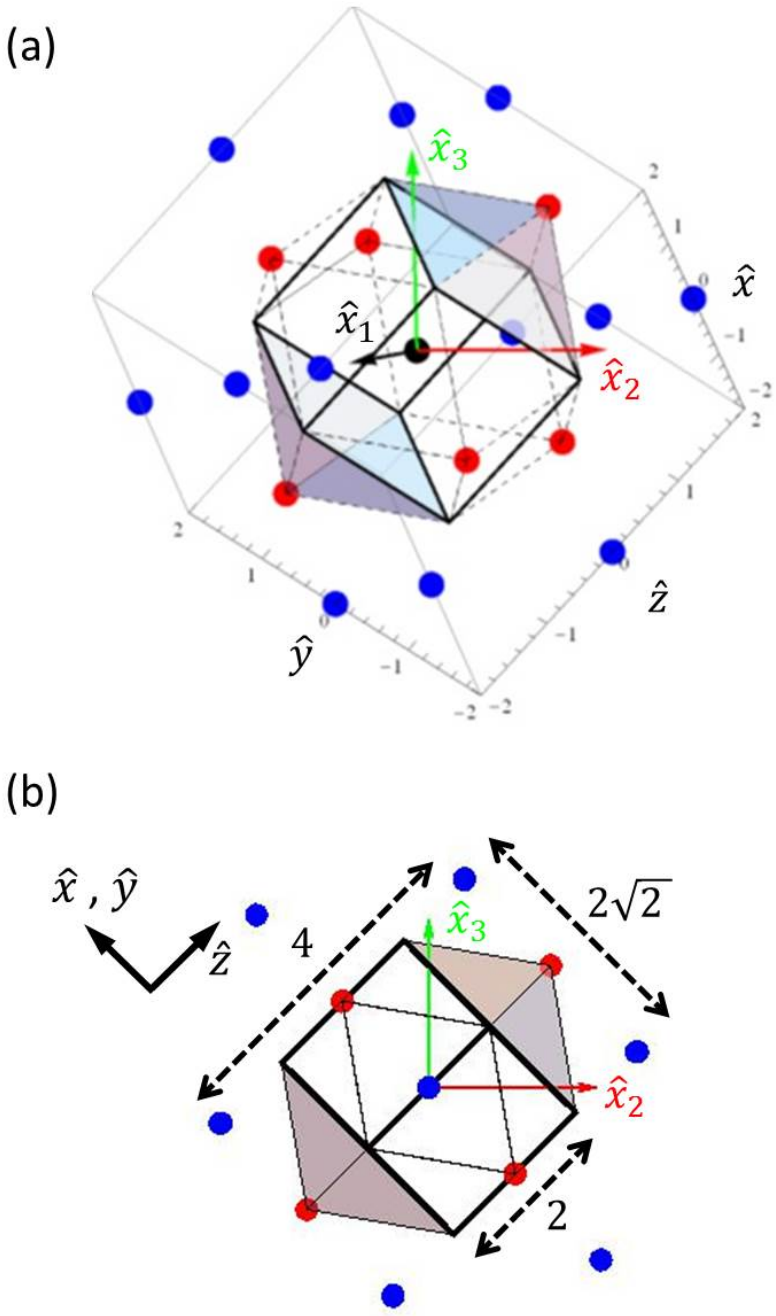

Figure 1.5: Reciprocal space of a simple cubic lattice. Red and blue dots indicate nearest-neighbor and next-nearest-neighbor points to the origin. The lattice wavevectors lie along $\hat{x}$, $\hat{y}$, and $\hat{z}$ (see also Figs. 1.2 and E.1). Distances are in units of $q_B = \hbar\pi/d$. (a) The first BZ is a cube of length $2\,q_B$ (bold lines) and the second BZ is formed by six square pyramids (dotted lines) attached to each face of the first BZ. (b) In TOF imaging, the reciprocal lattice is projected onto the imaging plane along $\hat{x}_1$. None of the three lattice directions $\hat{x}$, $\hat{y}$, and $\hat{z}$ are parallel to the imaging axis $\hat{x}_1$. On the imaging plane, the first BZ appear as a rectangle of length $2\,q_B$ by $2\sqrt{2}\,q_B$ and the second BZ partially overlaps with the first BZ. After bandmapping, atoms promoted to the first-excited band along the lattice direction $\hat{z}$ are mapped onto the shaded areas in the second BZ. Typical images after bandmapping are shown in (b) and (c) of Fig. 4.5.

Chapter 2

Stimulated Raman Transitions

Stimulated Raman transitions are a coherent two-photon process in an atom or molecule driven by two applied radiation fields. The fields induce absorption and stimulated emission between two ground states and an intermediate excited state, as shown in Fig. 2.1. In ultracold gas experiments, stimulated transitions are "Raman" when they couple two different hyperfine levels, whereas they are "Bragg" when they couple states in the same hyperfine levels. The two cases are described by the same theoretical framework, and therefore, both will be referred to as Raman transitions in this chapter.

Stimulated Raman transitions have been extensively applied to ultracold gas experiments. Raman beams have been used for cooling the motional [87] and vibrational [88, 89] degrees of freedom of a atomic gas, probing a low-temperature BEC via Bragg filtering [90], performing Bragg spectroscopy in strongly correlated phases [91], preparing higher orbital states in a lattice [92], detecting antiferromagnetism [27, 93], generating synthetic gauge fields [94–98], spin-orbit coupling [99–101] and spin-Hall effect [102, 103], and preparing the Hofstadter, Harper, and Haldane Hamiltonians [104–106]. Furthermore, Raman transitions have been proposed for detecting topological phases of matter [107–113].

In this chapter, we present the general theory of stimulated Raman transitions. Specifically, we derive the transition probability and coupling strength associated with Raman processes. In the experiments in Chapters 4 and 5, we employ this technique to prepare a gas in the first-excited band and to bring a strongly correlated gas out of equilibrium, respectively.

2.1 Three-Level Systems

A three-level system in a "Λ" configuration represents the atomic energy levels relevant to stimulated Raman transitions, as illustrated in Fig. 2.1, where $|1\rangle$ and $|2\rangle$ are two ground states, and $|e\rangle$ is an excited electronic state. Without loss of generality, we set the energy of $|1\rangle$ to zero. We denote the energy difference between the states $|e\rangle$ and $|1\rangle$ as $\hbar\omega_e$, and the energy difference between $|2\rangle$ and $|1\rangle$ as $\hbar\omega_0$. The Hamiltonian of the

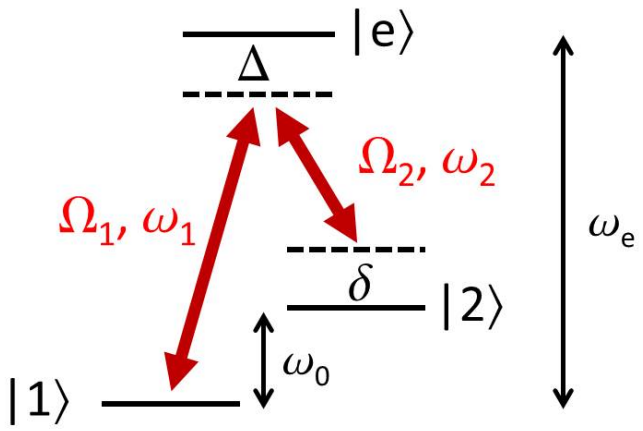

Figure 2.1: A three-level system in a "Λ" configuration. The electric fields $\mathbf{E}^{(1)}$ and $\mathbf{E}^{(2)}$ couple $|1\rangle$ with $|e\rangle$ and $|2\rangle$ with $|e\rangle$, respectively. The frequency offset ω_0 could be positive or negative depending on the relative energy levels of $|1\rangle$ and $|2\rangle$. When the detuning Δ is large compared with the coupling constants Ω_1 and Ω_2, the system behaves as an effective two-level system.

system is therefore

$$\hat{H} = \hbar\omega_e|e\rangle\langle e| + \hbar\omega_0|2\rangle\langle 2|. \tag{2.1}$$

By convention, we only consider situations where $\omega_e > 0$. The frequency offset ω_0 could be positive or negative depending on the relative energies of $|1\rangle$ and $|2\rangle$. In atomic systems, ω_e is in the optical range, whereas ω_0 can span from a few kHz to a few GHz depending on the transition under consideration.

To drive Raman transitions in this Λ system, we consider classical external electric fields in the form

$$\mathbf{E}(\mathbf{r},\tau) = \mathbf{E}^{(1)}\cos(\mathbf{k}_1\cdot\mathbf{r} - \omega_1\tau) + \mathbf{E}^{(2)}\cos(\mathbf{k}_2\cdot\mathbf{r} - \omega_2\tau). \tag{2.2}$$

We assume that the electric field 1 only couples $|1\rangle$ with $|e\rangle$ and the electric field 2 only couples $|2\rangle$ with $|e\rangle$. Under the electric dipole approximation $e^{i\mathbf{k}_i\cdot\hat{\mathbf{r}}} \approx 1$ —valid when the wavelength of the electric field is much longer than the length scale of the electronic wavefunctions [114, 115]—the electric fields interact with the atomic gas via the Hamiltonian

$$\hat{H}_I = -\hat{\mathbf{d}}\cdot\mathbf{E}(0,\tau), \tag{2.3}$$

where $\hat{\mathbf{d}} = -e\hat{\mathbf{r}}$ is the induced electric dipole moment [116].

We look for solutions to the full Hamiltonian of the system

$$\hat{H} = \hat{H}_0 + \hat{H}_I \tag{2.4}$$

with the ansatz

$$|\psi(\tau)\rangle = c_1(\tau)|1\rangle + c_e(\tau)e^{-i\omega_e\tau}|e\rangle + c_2(\tau)e^{-i\omega_2\tau}|2\rangle, \tag{2.5}$$

which leads to (in the basis ordering $\{|1\rangle, |e\rangle, |2\rangle\}$)

$$i\hbar\frac{d}{d\tau}\begin{pmatrix} c_1 \\ c_e \\ c_2 \end{pmatrix} = \frac{\hbar}{2}\begin{pmatrix} 0 & \Omega_1^* e^{i\Delta\tau} & 0 \\ \Omega_1 e^{-i\Delta\tau} & 0 & \Omega_2 e^{-i(\Delta-\delta)\tau} \\ 0 & \Omega_2^* e^{i(\Delta-\delta)\tau} & 0 \end{pmatrix}\begin{pmatrix} c_1 \\ c_e \\ c_2 \end{pmatrix}. \tag{2.6}$$

The fast oscillating counter-rotating terms $e^{\pm i(\omega_1+\omega_e)\tau}$ and $e^{\pm i(\omega_2+\omega_e-\omega_0)}$ have been neglected under the rotating-wave approximation [117].

The Rabi rates Ω_1 and Ω_2 in Eq. 2.6 quantify the strength of the one-photon dipole coupling between the ground and excited electronic states, and they are defined as

$$\Omega_i = \langle e|e\hat{\mathbf{r}}\cdot\mathbf{E}^{(i)}|i\rangle/\hbar \qquad i = 1, 2. \tag{2.7}$$

The frequency

$$\Delta = \omega_1 - \omega_e \tag{2.8}$$

is the detuning of the electric field 1 from the transition $|1\rangle \leftrightarrow |e\rangle$, and the frequency

$$\delta = \omega_1 - \omega_2 - \omega_0 \tag{2.9}$$

is the detuning of the two-photon transition from $|1\rangle \leftrightarrow |2\rangle$ (see Fig. 2.1). In our experiments, Δ is typically a few hundreds of GHz, whereas δ usually ranges from 0 to a few tens of kHz.

In order to eliminate the time dependence in the matrix in Eq. 2.6, we switch the system to a co-rotating frame using the unitary transformation

$$U = \begin{pmatrix} 1 & 0 & 0 \\ 0 & e^{-i\Delta\tau} & 0 \\ 0 & 0 & e^{-i\delta\tau} \end{pmatrix}, \tag{2.10}$$

where the wavefunctions transform as $|\tilde{\psi}\rangle = U^\dagger|\psi\rangle$, and the Hamiltonian transforms as $\tilde{H} = U^\dagger H U -$

$i\hbar U^\dagger \partial U/\partial\tau$. The system therefore becomes

$$i\hbar\frac{d}{d\tau}\begin{pmatrix}\tilde{c}_1\\ \tilde{c}_e\\ \tilde{c}_2\end{pmatrix} = \frac{\hbar}{2}\begin{pmatrix}0 & \Omega_1^* & 0\\ \Omega_1 & -2\Delta & \Omega_2\\ 0 & \Omega_2^* & -2\delta\end{pmatrix}\begin{pmatrix}\tilde{c}_1\\ \tilde{c}_e\\ \tilde{c}_2\end{pmatrix} \tag{2.11}$$

Even though there is an exact analytical solution to Eq. 2.11 [118], a practical approximation can be obtained when Δ is large compared with Ω_1, Ω_2 and δ, which is usually the case in our experiments. In such approximation, the dynamics of $\tilde{c}_e$ is much faster than that of $\tilde{c}_1$ and $\tilde{c}_2$, and thus, $\tilde{c}_e$ instantly follows the slow dynamics of $\tilde{c}_1$ and $\tilde{c}_2$. Therefore, $\tilde{c}_e$ can be "adiabatically eliminated"[1] from Eq. 2.11 by setting $\dot{\tilde{c}}_e \approx 0$, which results in

$$\tilde{c}_e(\tau) \approx \frac{\Omega_1}{2\Delta}\tilde{c}_1(\tau) + \frac{\Omega_2}{2\Delta}\tilde{c}_2(\tau) \tag{2.12}$$

and the effective two-level system

$$i\hbar\frac{d}{d\tau}\begin{pmatrix}\tilde{c}_1\\ \tilde{c}_2\end{pmatrix} = \hbar\begin{pmatrix}\frac{|\Omega_1|^2}{4\Delta} & \frac{\Omega_1^*\Omega_2}{4\Delta}\\ \frac{\Omega_1\Omega_2^*}{4\Delta} & -\delta+\frac{|\Omega_2|^2}{4\Delta}\end{pmatrix}\begin{pmatrix}\tilde{c}_1\\ \tilde{c}_2\end{pmatrix}. \tag{2.13}$$

The terms $\hbar|\Omega_1|^2/4\Delta$ and $\hbar|\Omega_2|^2/4\Delta$ represent the light shift (a.c. Stark shift) induced by weak electric dipole coupling with $|e\rangle$, and the off-diagonal elements are the coupling strength between the states $|1\rangle$ and $|2\rangle$.

The probability of exciting an atom from $|1\rangle$ to $|2\rangle$ is obtained from solving Eq. 2.13. If we assume the initial conditions $\tilde{c}_1(0) = 1$ and $\tilde{c}_2(0) = 0$, the solution is

$$|\tilde{c}_2(\tau)|^2 = \frac{|\Omega|^2}{|\Omega|^2 + \left(\delta - \frac{|\Omega_2|^2-|\Omega_1|^2}{4\Delta}\right)^2}\sin^2\left[\sqrt{\left(\delta - \frac{|\Omega_2|^2-|\Omega_1|^2}{4\Delta}\right)^2 + |\Omega|^2}\,\frac{\Delta\tau}{2}\right], \tag{2.14}$$

where

$$\Omega = \frac{\Omega_1\Omega_2^*}{2\Delta} \tag{2.15}$$

is the effective Rabi rate of the two-photon transition [121, 122], Ω_1 and Ω_2 are the one-photon Rabi rates defined in Eq. 2.7, and $\Delta\tau$ is the duration of the light pulse. The frequency shift $(|\Omega_2|^2 - |\Omega_1|^2)/4\Delta$ in Eq. 2.14 represents the relative light shift between $|2\rangle$ and $|1\rangle$. As a way of simplifying the notation, the frequency ω_0 in Eq. 2.9 can be re-defined to include such frequency shift.

[1] For a discussion on the validity of adiabatic elimination, see Refs. [119, 120].

2.2 Multi-Level Systems

So far we have only considered Raman excitations in a simple Λ model. In a real atomic system, however, multiple energy levels are involved in the process.

In order to derive the Rabi rate in a multi-level system, we consider the fine and hyperfine structure of an atomic system, such as that shown in Fig. 1.1 for ^{87}Rb. The quantum numbers J, F, and m_F are the total electronic angular momentum, the total electronic-plus-nuclear angular momentum[2], and the projection of F onto the quantization axis. The primed symbols J', F', m'_F label quantum numbers in the excited electronic states. Because δ is usually small compared with the hyperfine energy splitting, it is a good approximation to assume that the Raman fields drive transitions between two specific hyperfine states. On the other hand, the detuning Δ is usually large compared with the hyperfine energy splitting, and therefore, all the excited levels within a hyperfine manifold have to be taken into account to determine the effective Rabi rate.

If we consider two ground atomic states $|J_1\, F_1\, m_{F_1}\rangle$ and $|J_2\, F_2\, m_{F_2}\rangle$, the multi-level effective Rabi rate results from summing over all the adiabatically eliminated[3] excited states $|J'\, F'\, m'_F\rangle$, namely

$$\begin{aligned}\Omega &= \sum_{F',m'_F} \frac{\Omega_1 \Omega_2^*}{2\Delta} \\ &= \frac{1}{2\hbar^2\Delta} \sum_{F',m'_F} \langle J_2\, F_2\, m_{F_2}|e\hat{\mathbf{r}}\cdot\mathbf{E}^{(2)}|J'\, F'\, m'_F\rangle\langle J'\, F'\, m'_F|e\hat{\mathbf{r}}\cdot\mathbf{E}^{(1)}|J_1\, F_1\, m_{F_1}\rangle. \end{aligned} \tag{2.16}$$

The dipole matrix elements are more easily computed in the spherical basis[4] $\hat{\epsilon}_{\pm1} = \mp(\hat{x}\pm i\hat{y})/\sqrt{2}$ and $\hat{\epsilon}_0 = \hat{z}$. In this basis, $\hat{\mathbf{d}}\cdot\mathbf{E} = \sum_q \hat{d}_q^* E_q = \sum_q \hat{d}_q E_q^* = \sum_q (-1)^q \hat{d}_{-q} E_q$ and the spherical components of the electric field are given by

$$\begin{aligned} E_{\pm1} &= \mp\frac{1}{\sqrt{2}}(E_x \pm iE_y) \\ E_0 &= E_z. \end{aligned} \tag{2.17}$$

By definition, $\hat{\epsilon}_0$ is parallel to the quantization magnetic field $\hat{B}$, which lies along $\hat{x}_1$ in our apparatus.

The effective Rabi rate is therefore

$$\Omega = \frac{1}{2\hbar^2\Delta} \sum_{q_1,q_2} E_{q_1}^{(1)*} E_{q_2}^{(2)} (-1)^{q_2} \sum_{F',m'_F} \langle J_2\, F_2\, m_{F_2}|e\hat{r}_{-q_2}|J'\, F'\, m'_F\rangle\langle J'\, F'\, m'_F|e\hat{r}_{q_1}|J_1\, F_1\, m_{F_1}\rangle. \tag{2.18}$$

The second matrix element is nonzero only if $m'_F = m_{F_1} + q_1$, and the first matrix element is nonzero only if

[2] $F = J + I$, with I the nuclear spin ($I = 3/2$ for ^{87}Rb).

[3] An alternative derivation without adiabatic elimination is presented in Ref. [122].

[4] In the spherical basis, an arbitrary vector $\mathbf{A}$ is decomposed as $\mathbf{A} = \sum_q \mathrm{A}_q \hat{\epsilon}_q^* = \sum_q \mathrm{A}_q^* \hat{\epsilon}_q = \sum_q (-1)^q \mathrm{A}_{-q} \hat{\epsilon}_q$, where $A_{\pm1} = \mp(A_x \pm iA_y)/\sqrt{2}$ and $A_0 = A_z$ (they are the $\sigma^\pm$ and π-polarization components, respectively).

$m_{F_2} = m'_F - q_2$. Consequently, a two-photon transition must satisfy the momentum conservation condition $m_{F_2} = m_{F_1} + q_1 - q_2$. Each matrix element in Eq. 2.18 can be expressed as the product of a geometrical factor with a reduced dipole matrix $\langle J' \| e\hat{\mathbf{r}} \| J \rangle$, namely

$$\langle JFm_F | e\hat{r}_q | J'F'm'_F \rangle = \langle J' \| e\hat{\mathbf{r}} \| J \rangle (-1)^{J+I-m_F} \sqrt{(2F+1)(2F'+1)} \begin{Bmatrix} J & F & I \\ F' & J' & 1 \end{Bmatrix} \begin{pmatrix} F' & 1 & F \\ m'_F & q & -m_F \end{pmatrix}, \tag{2.19}$$

where { } and ( ) denote the Wigner six and three-J symbols, respectively. The reduced dipole matrix element depends on the internal structure of the atom and is not easily calculated. However, it can be experimentally determined from measurements of spontaneous decay from the excited level J' to the ground level J [73,123] via

$$\Gamma = \frac{\omega_0^3}{3\pi\varepsilon_0 \hbar c^3} \frac{|\langle J' \| e\hat{\mathbf{r}} \| J \rangle|^2}{2J'+1}. \tag{2.20}$$

The effective Rabi rate then becomes

$$\hbar\Omega = \frac{3\pi\varepsilon_0 c^3 \Gamma}{2\omega_0^3 \Delta} \sum_{q_1, q_2} E^{(1)*}_{q_1} E^{(2)}_{q_2} (-1)^{q_2} \sum_{F', m'_F} G^{J'\,F'\,m'_F}_{J_2\,F_2\,m_{F_2}}(-q_2) G^{J_1\,F_1\,m_{F_1}}_{J'\,F'\,m'_F}(q_1), \tag{2.21}$$

where we have defined the geometrical factor

$$G^{J'\,F'\,m'_F}_{J\,F\,m_F}(q) = (-1)^{J+I-m_F} \sqrt{(2J'+1)(2F+1)(2F'+1)} \begin{Bmatrix} J & F & I \\ F' & J' & 1 \end{Bmatrix} \begin{pmatrix} F' & 1 & F \\ m'_F & q & -m_F \end{pmatrix}. \tag{2.22}$$

Eq. 2.21 is valid for any stimulated two-photon transition between two ground hyperfine states $|J_1\, F_1\, m_{F_1}\rangle$ and $|J_2\, F_2\, m_{F_2}\rangle$. In particular, Eq. 2.21 reduces to the formula for light shift when $E^{(1)}_{q_1} = E^{(2)}_{q_2}$, $q_1 = q_2$, $|J_1\, F_1\, m_{F_1}\rangle = |J_2\, F_2\, m_{F_2}\rangle$ and an additional factor of $1/2$ is included (the light-shift formula has an extra factor of $1/2$ in the definition), namely

$$\frac{\hbar|\Omega_1|^2}{4\Delta} = \frac{3\pi\varepsilon_0 c^3 \Gamma}{4\omega_0^3 \Delta} \sum_{q_1} E^{(1)}_{q_1} E^{(1)*}_{q_1} \sum_{F', m'_F} |G^{J_1\,F_1\,m_{F_1}}_{J'\,F'\,m'_F}(q_1)|^2. \tag{2.23}$$

This expression can be further simplified using $I^{(1)}_q = c\varepsilon_0 E^{(1)}_q E^{(1)*}_q/2$ and the identity

$$\sum_{F', m'_F} |G^{J_1\,F_1\,m_{F_1}}_{J'\,F'\,m'_F}(q)|^2 = \frac{J'+1/2+2(J'-1)qg_F m_F}{3}. \tag{2.24}$$

The equation reduces to

$$\frac{\hbar|\Omega_1|^2}{4\Delta} = \frac{\pi c^2 \Gamma}{2\omega_0^3 \Delta} \sum_q I_q^{(1)} \left[J' + 1/2 + 2(J'-1) q g_{F1} m_{F_1}\right]. \tag{2.25}$$

For linearly polarized light ($q = 0$), this formula leads to the dipole potential given by Eq. 1.2 (when the counter-propagating terms are ignored).

2.3 Motional Degrees of Freedom

In this section, we include in the theoretical framework the motional degrees of freedom of the atoms, such as their position, momentum or quasimomentum. Specifically, we will calculate the Rabi rate of a free and lattice-bound gas. For the sake of simplicity, we will only consider a three-level system, although the result can be straightforwardly extended to a multi-level system by summing over the excited electronic states. Furthermore, we will make the assumption that the dynamics of the gas is frozen out during the Raman process, since the Raman fields are on for a short period of time (< 1 ms) compared with the motional time scales.

2.3.1 Stimulated Raman Transitions in Free Space

We consider stimulated Raman transitions in a free gas, which is also applicable to a harmonically-trapped gas, since the duration of the Raman process is usually much shorter than the time associated with the trap frequencies. We include the atomic kinetic energy $\hat{\mathbf{p}}^2/2m$ into the Hamiltonian 2.4, and we label the atomic states by their internal state and momentum, namely $|1, \mathbf{p}\rangle, |2, \mathbf{p}'\rangle$, and $|e, \mathbf{p}_e\rangle$. Moreover, we consider the center of mass coordinate $\hat{\mathbf{R}}$ in addition to the internal coordinate $\mathbf{r}$.

The atomic system is now solved using the ansatz [121]

$$|\psi(\tau)\rangle = \sum_{i=1,2,e} c_{i,\mathbf{p}}(\tau) e^{-i\left(\omega_i + \frac{p^2}{2m\hbar}\right)\tau} |i, \mathbf{p}\rangle, \tag{2.26}$$

which, under the dipole approximation $e^{i\mathbf{k}_i \cdot (\hat{\mathbf{r}} + \hat{\mathbf{R}})} \approx e^{i\mathbf{k}_i \cdot \hat{\mathbf{R}}}$, leads to the effective Rabi rate [124]

$$\Omega(\mathbf{p}', \mathbf{p}) = \frac{1}{2\hbar^2 \Delta} \langle 2, \mathbf{p}' | e\hat{\mathbf{r}} \cdot \mathbf{E}^{(2)} e^{-i\mathbf{k}_2 \cdot \hat{\mathbf{R}}} | e, \mathbf{p}_e \rangle \langle e, \mathbf{p}_e | e\hat{\mathbf{r}} \cdot \mathbf{E}^{(1)} e^{i\mathbf{k}_1 \cdot \hat{\mathbf{R}}} | 1, \mathbf{p} \rangle. \tag{2.27}$$

The first matrix element is equal to $\langle 2 | e\hat{\mathbf{r}} \cdot \mathbf{E}^{(2)} | e \rangle \langle \mathbf{p}' | e^{-i\mathbf{k}_2 \cdot \hat{\mathbf{R}}} | \mathbf{p}_e \rangle = \hbar \Omega_2^* \langle \mathbf{p}' | \mathbf{p}_e - \hbar \mathbf{k}_2 \rangle$, and the second matrix

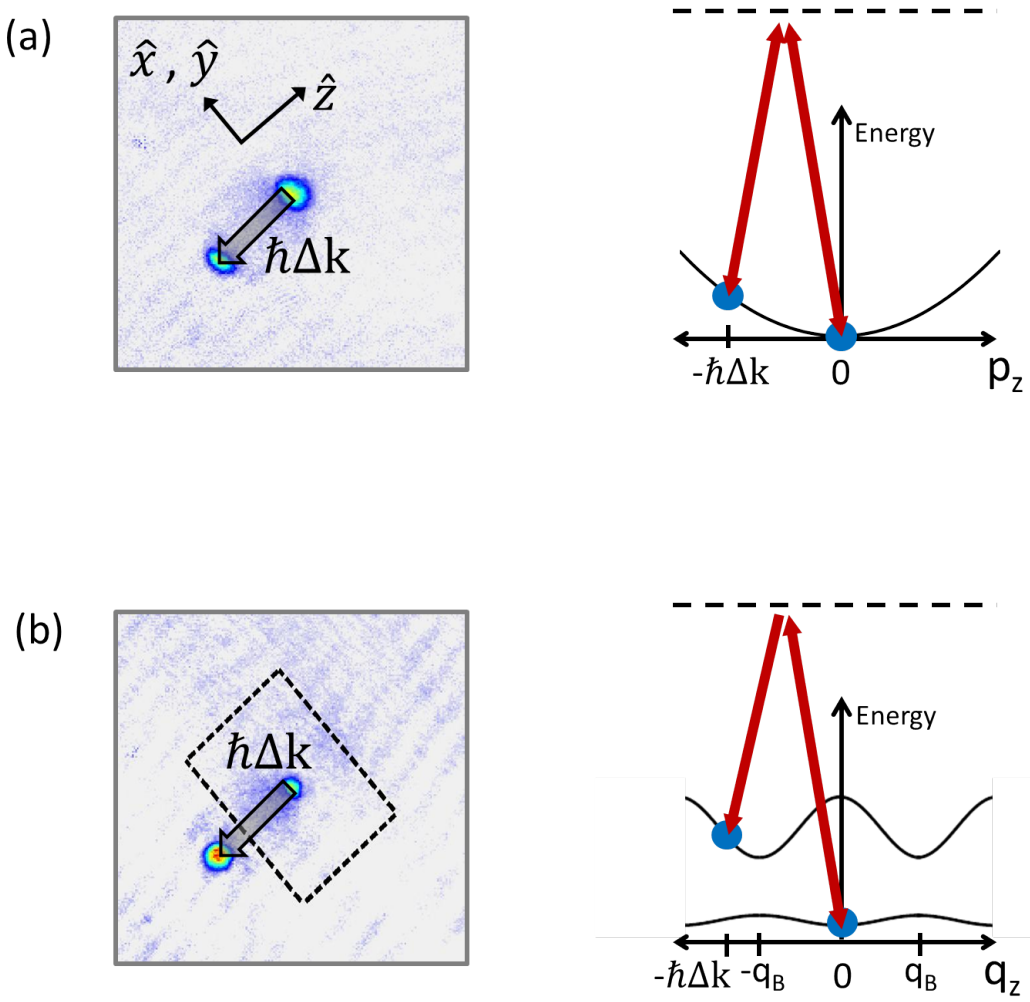

Figure 2.2: TOF images of a BEC after stimulated Raman excitation. Energy diagrams along $\hat{z}$ are shown on the right. The Raman beams give a momentum impulse $\hbar\Delta k = \hbar k_1 - \hbar k_2$ to the gas. (a) The gas is confined in a harmonic trap. (b) The gas is confined in a lattice-plus-harmonic trap. In this particular example, atoms are transferred to the first-excited band. After bandmapping, the excited atoms appear outside the first BZ (the dotted rectangle marks the first BZ projected onto the imaging plane, as detailed in Appendix E). Only the ground and first-excited bands are shown in the energy diagram. The quasimomenta $\pm q_B$ mark the edge of the first BZ, where $q_B = \hbar\pi/d$.

element has a similar expression. The effective Rabi rate is therefore

$$\Omega(\mathbf{p}', \mathbf{p}) = \frac{\Omega_1 \Omega_2^*}{2\Delta} \langle \mathbf{p}' | \mathbf{p} + \hbar\mathbf{k}_1 - \hbar\mathbf{k}_2 \rangle, \tag{2.28}$$

which ensures the condition $\mathbf{p}' = \mathbf{p} + \hbar\mathbf{k}_1 - \hbar\mathbf{k}_2$ for momentum conservation. Part (a) of Fig. 2.2 shows a TOF image of a BEC after stimulated Raman excitation in a harmonic trap.

The Raman detuning δ in Eq. 2.9 is modified by the free-particle dispersion relation as

$$\delta = \omega_1 - \omega_2 - \left[\omega_0 + \frac{1}{\hbar} \left(\frac{\mathbf{p}'^2}{2m} - \frac{\mathbf{p}^2}{2m} \right) \right]. \tag{2.29}$$

The terms inside the innermost brackets are equal to $\mathbf{p}(\mathbf{k}_1 - \mathbf{k}_2)/m + \hbar(\mathbf{k}_1 - \mathbf{k}_2)^2/2m$, where the first term is the Doppler shift that arises from the atomic motion along $\mathbf{k}_1 - \mathbf{k}_2$, and the second term is the recoil shift from the two-photon absorption-emission process [121]. The Doppler and recoil shifts also modify the detuning Δ in Eq. 2.8 [121], but the change is negligible compared with $\omega_1 - \omega_e$ (in ultracold gas experiments, $\omega_1 - \omega_e$ is typically a few hundred of GHz, whereas the Doppler and recoil shifts are just a few kHz).

2.3.2 Stimulated Raman Transitions in a Lattice Potential

For a gas confined in a lattice potential, we include the term $\hat{\mathbf{p}}^2/2m + V_{\text{lat}}(\hat{\mathbf{R}})$ in the Hamiltonian 2.4, where the lattice potential is given by Eq. 1.11. We consider Bloch states with band index n and quasimomentum $\mathbf{q}$. Specifically, we consider two ground states and one intermediate excited state in the form $|1, n, \mathbf{q}\rangle, |2, n', \mathbf{q}'\rangle$, and $|e, n_e, \mathbf{q}_e\rangle$, respectively.

Because Δ is large compared with the vibrational energies, we consider the same detuning Δ for all the sublevels $|e, n_e, \mathbf{q}_e\rangle$. On the other hand, we assume δ small compared with the vibrational energies so that the Raman fields couple individual vibrational states $|n\rangle$ and $|n'\rangle$.

To solve the system, we consider the ansatz

$$|\psi(\tau)\rangle = \sum_{i=1,2,e} c_{i,\mathbf{q}}(\tau) e^{-i\left[\omega_i + \epsilon^{(n)}(\mathbf{q})/\hbar\right]\tau} |i, n, \mathbf{q}\rangle, \tag{2.30}$$

where $\epsilon^{(n)}(\mathbf{q})$ is the energy of the n-th band. The resulting effective Rabi rate, under the dipole approxima-

tion, is given by Eq. 2.15 under summation over all the vibrational states in $|e\rangle$, namely

$$\begin{aligned}\Omega_{n',n}(\mathbf{q}',\mathbf{q}) &= \frac{1}{2\hbar^2\Delta}\sum_{n_e}\langle 2,n',\mathbf{q}'|e\hat{\mathbf{r}}\cdot\mathbf{E}^{(2)}e^{-i\mathbf{k}_2\cdot\hat{\mathbf{R}}}|e,n_e,\mathbf{q}_e\rangle\langle e,n_e,\mathbf{q}_e|e\hat{\mathbf{r}}\cdot\mathbf{E}^{(1)}e^{i\mathbf{k}_1\cdot\hat{\mathbf{R}}}|1,n,\mathbf{q}\rangle \\ &= \frac{\Omega_1\Omega_2^*}{2\Delta}\sum_{n_e}\langle n',\mathbf{q}'|e^{-i\mathbf{k}_2\cdot\hat{\mathbf{R}}}|n_e,\mathbf{q}_e\rangle\langle n_e,\mathbf{q}_e|e^{i\mathbf{k}_1\cdot\hat{\mathbf{R}}}|n,\mathbf{q}\rangle \\ &= \frac{\Omega_1\Omega_2^*}{2\Delta}\langle n',\mathbf{q}'|e^{i(\mathbf{k}_1-\mathbf{k}_2)\cdot\hat{\mathbf{R}}}|n,\mathbf{q}\rangle. \end{aligned} \tag{2.31}$$

This Rabi rate is zero unless $\mathbf{q}' = \mathbf{q}+\hbar\mathbf{k}_1-\hbar\mathbf{k}_2$ (besides a vector of the reciprocal lattice), which is consistent with momentum conservation. Part (b) of Fig. 2.2 shows a TOF image of a BEC after stimulated Raman excitation in a lattice-plus-harmonic potential.

The matrix element in Eq. 2.31 is the analogous to the Franck-Condon factor for molecular physics, and it determines the strength of the Raman coupling between different vibrational states [125]. The exponential term in Eq. 2.31 modifies the spatial overlap between the Bloch states $|n,\mathbf{q}\rangle$ and $|n',\mathbf{q}'\rangle$. In order to understand the effect of the Franck-Condon factor on the effective Rabi rate, we approximate the lattice sites by harmonic oscillators to obtain the explicit formula (in 1D) [124, 126]

$$|\langle n'|e^{i\Delta k\,\hat{z}}|n\rangle| = e^{-\frac{(\Delta k z_0)^2}{2}}\left(\frac{n_<!}{n_>!}\right)^{1/2}|\Delta k\, z_0|^{|n'-n|}L_{n_<}^{|n'-n|}(\Delta k^2 z_0^2), \tag{2.32}$$

where $n_<$ ($n_>$) is the lesser (greater) of n' and n, $z_0 = \sqrt{\hbar/(2m\omega_z)}$, $\hbar\omega_z$ is the bandgap, and L_n^α is the generalized Laguerre polynomial

$$L_n^\alpha(x) = \sum_{m=0}^{n}(-1)^m\binom{n+\alpha}{n-m}\frac{x^m}{m!}. \tag{2.33}$$

In our experiments, we usually start from the ground vibrational state ($n = 0$), for which the Laguerre polynomial simplifies to $L_0^\alpha(x) = 1$. In the particular case of $n = n' = 0$, the Franck-Condon factor reduces to the Debye-Waller factor $e^{-(\Delta k z_0)^2/2}$ familiar from the studies of x-ray scattering in solids [126].

In Fig. 2.3, we plot $|\langle n'|e^{i\Delta k\,\hat{z}}|0\rangle|$ versus the Raman wavevector Δk and versus the bandgap $\hbar\omega_z$. We observe in (a) that, in order to couple $n = 0$ to a higher vibrational state ($n' \neq 0$), the wavelength of the excitation field must be comparable to the lattice spacing d [5]. For this reason, long wavelength radiation, such as radio and microwave-frequency fields, can not change the vibrational state of particles confined in an optical lattice (where $d \sim \mu$m). This limitation can be overcome by spatially displacing the wavefunctions of the excited vibrational state, for example, by using a spin-dependent optical lattice [127, 128].

[5] This is generally true for any transition with $n \neq n'$, since $|\langle n'|e^{i\Delta k\,\hat{z}}|n\rangle| \approx |\langle n'|n\rangle| = 0$ when $\Delta k\, z \ll 1$.

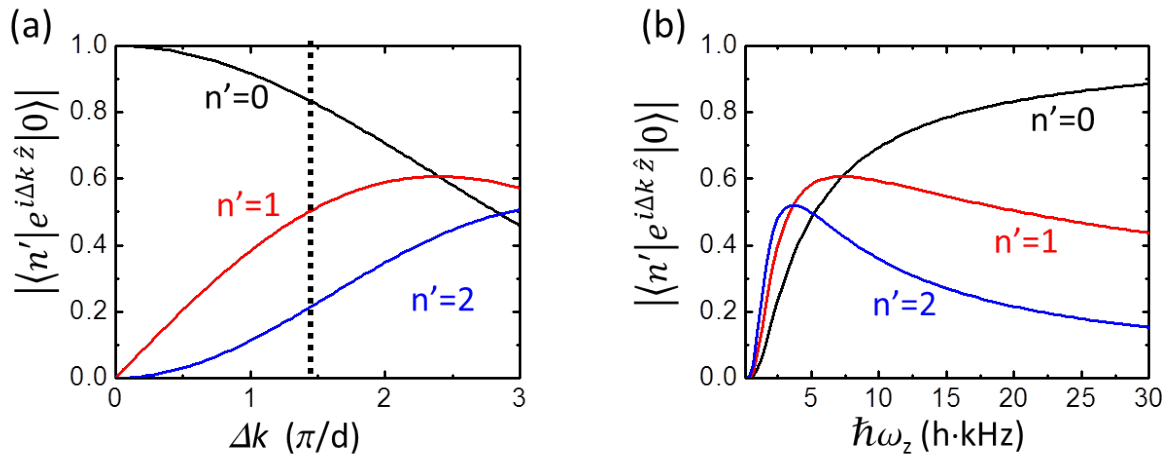

Figure 2.3: Coupling strength between vibrational levels. (a) Plot of the Franck-Condon factor in Eq. 2.32 versus Δk between $n = 0$ and $n' = 0, 1, 2$. The bandgap used is $\hbar\omega_z = 20$ kHz $\times\, h$. The dotted vertical line indicates $\Delta k = 1.45\,\pi/d$, which is approximately the wavevector used in the experiments in Chapters 4 and 5. (b) Plot of the Franck-Condon factor versus $\hbar\omega_z$ using $\Delta k = 1.45\,\pi/d$.

The Raman detuning δ in Eq. 2.9 is modified by the band structure as

$$\delta = \omega_1 - \omega_2 - \left[\omega_0 + \frac{\epsilon^{(n')}(\mathbf{q}') - \epsilon^{(n)}(\mathbf{q})}{\hbar}\right], \tag{2.34}$$

where $\mathbf{q}' = \mathbf{q} + \hbar\mathbf{k}_1 - \hbar\mathbf{k}_2$. The momentum impulse $\Delta\mathbf{q} = \mathbf{q}' - \mathbf{q} = \hbar\mathbf{k}_1 - \hbar\mathbf{k}_2$ is set by the spatial configuration of the Raman beams and is usually fixed in an experiment.

The relative Raman detuning $\omega_1 - \omega_2$ can be adjusted to target different quasimomenta. At sufficiently low lattice depths, the curvature of the energy bands can be used to address different quasimomentum states, as shown in Fig. 2.4. We refer to this process as quasimomentum-selective stimulated Raman transition. In (b) of Fig. 2.4, the excitation probability is calculated using

$$P(q) = \frac{|\Omega|^2}{|\Omega|^2 + \delta(q)^2} \sin^2\left[\sqrt{\delta(q)^2 + |\Omega|^2}\,\frac{\Delta\tau}{2}\right], \tag{2.35}$$

where Ω is the effective Rabi rate defined in Eq. 2.31 and $\delta(q)$ is defined in Eq. 2.34. Eq. 2.35 follows directly from Eq. 2.14. The degree of quasimomentum selectivity in $P(q)$ is controlled by the pulse length $\Delta\tau$. Indeed, the profile $P(q)$ becomes narrower for longer pulses. In practice, however, Raman pulses are chosen to be short compared with the time scale of the gas dynamics.

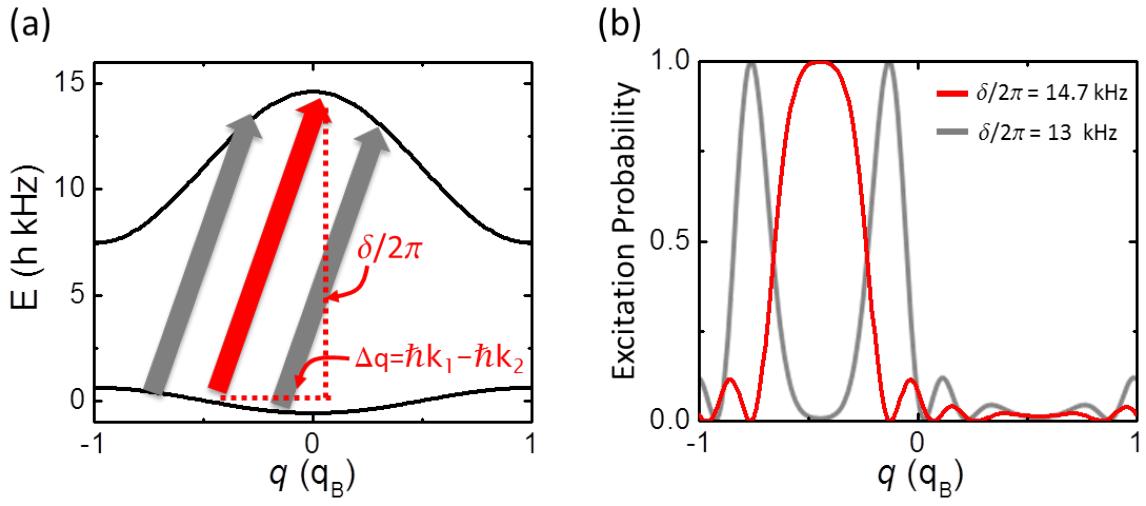

Figure 2.4: Quasimomentum-selective Raman transition. (a) Ground and first-excited energy bands in a $s = 4$ E_R lattice for ^{87}Rb (black curves). The red and grey arrows represent effective Raman transitions for two different detunings: $\delta = (2\pi) \times 14.7$ kHz and $\delta = (2\pi) \times 13$ kHz, respectively. Here, we consider transitions with $\omega_0 = 0$ in Eq. 2.34. (b) Excitation probabilities for the detunings aforementioned calculated using Eq. 2.35 with $\Delta q = 0.5\, q_B$, $\Omega = (2\pi) \times 1$ kHz, and $\Delta\tau = 0.5$ ms. Different quasimomenta can be targeted by varying δ.

2.4 Implementation

The Raman beams are generated from a CW single frequency titanium-sapphire laser (Tekhno Scan TIS-SF-07) similar to the laser used for the lattice beams (Section 1.1.2). A schematic diagram of the Raman beam setup is shown in Fig. 2.5.

2.4.1 Sideband Modulation

The Ti:Sa laser is phase-modulated by an electro-optic modulator (EOM) to create sidebands to drive the Raman transitions. An EOM is a birefringent crystal that changes the phase of an incoming light proportionally to the applied voltage $\mathcal{V}(t)$ [129], namely[6]

$$\phi(\tau) = \phi_0 - \pi \frac{\mathcal{V}(\tau)}{\mathcal{V}_\pi}, \tag{2.36}$$

where $\mathcal{V}_\pi$ is the voltage at which the phase of the light field shifts by π. In our experiments, we use a fiber coupled lithium niobate EOM (EOspace PM-0K5-00-PFA-PFA-800-S)[7].

[6] The phase constant ϕ_0 is irrelevant for our calculation and will be ignored.

[7] The specifications are: $\mathcal{V}_\pi \approx 1$ V_{rms}, wavelength: 800 nm, bandwidth: DC to $>$ 500 MHz, no internal termination (capacitive): $\pm 20 - 25$ V, insertion loss < 5 dB, input and output: PM 5 μm PANDA, polarization crosstalk: -18 dB. The EOM is not properly terminated. The voltage on the EOM depends on ω and is not simply related to the power setting on the generator.

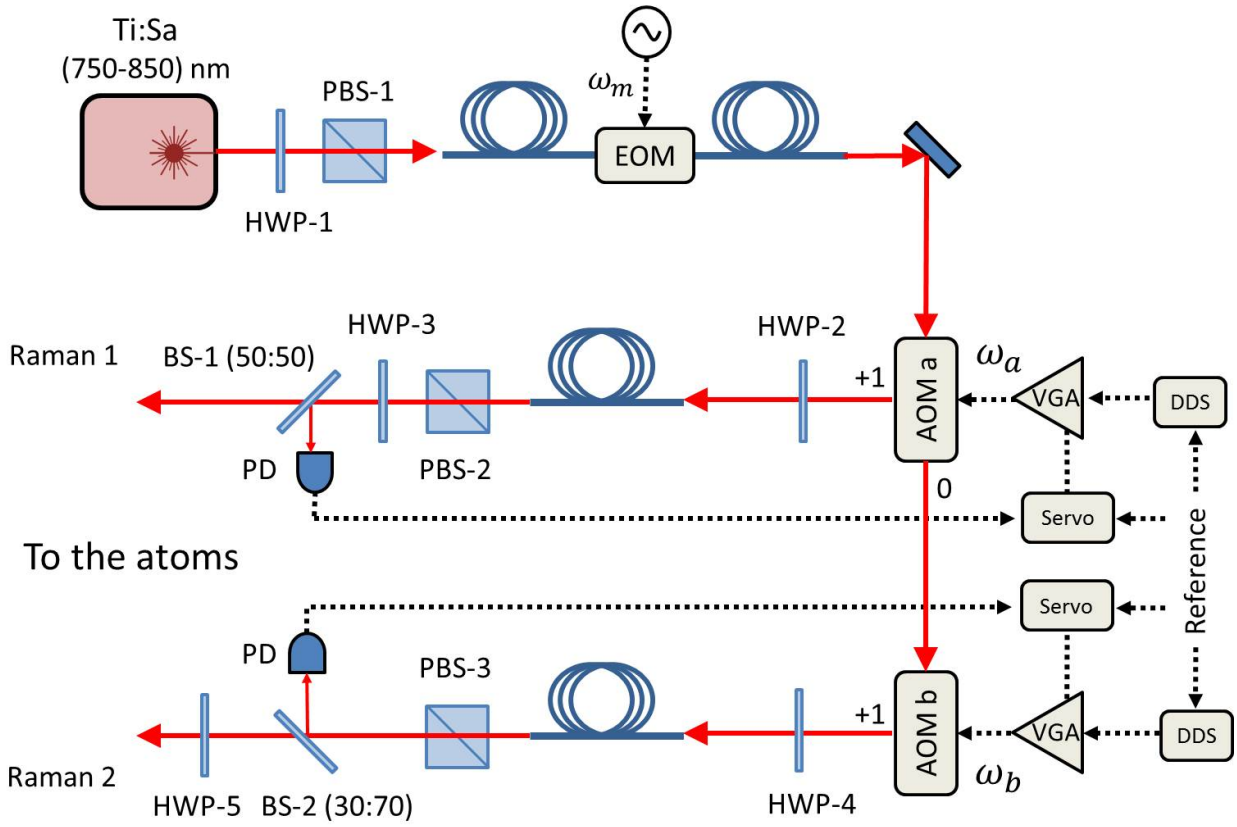

Figure 2.5: Simplified schematic of the optical setup for the Raman beams. The system is composed of a titanium:sapphire (Ti:Sa) laser, an electro-optic modulator (EOM), beam splitters (BS), polarizing beam splitters (PBS), half waveplates (HWP), photodiodes (PD), and single-mode polarization maintaining optical fibers. The PBSs are used to filter the laser polarization. HWP-3 and HWP-5 are used to change the light polarization from pure σ to pure π. Focusing lenses are not shown. Each acousto-optical modulator (AOM) is driven by a direct digital synthesizer (DDS). Each Raman beam is intensity-regulated using a PI servo and a variable-gain amplifier (VGA). A control computer dynamically sets the reference for the AOM frequency and the light intensity. Dotted lines indicate electrical connections.

The implementation of Raman beams via sideband modulation is relatively simpler than using other techniques, such as phase-locked lasers or high frequency AOMs. The disadvantage of using sidebands is that part of the optical power is unused. Nevertheless, power limitation is rarely a concern, since the power requirement rarely exceeds 1 mW per beam. Using sideband modulation, we have demonstrated stimulated Raman transitions in the range kHz–GHz.

We modulate the EOM using a voltage source (SRS SG384) able to generate a broadband sine wave from DC to 4 GHz with μHz resolution. For concreteness, we consider a modulation voltage in the form

$$\mathcal{V}(t) = \mathcal{V}_0 \sin \omega_m t \tag{2.37}$$

with the modulation frequency ω_m. The phase-modulated laser light has an electric field given by (ignoring the spatial coordinate)

$$\begin{aligned} E(\tau) &= E\cos(-\omega\tau + \phi(\tau)) \\ &= E\cos(\omega\tau + \phi_1 \sin\omega_m\tau) \\ &= E\sum_{j=-\infty}^{\infty} J_j(\phi_1)\cos[(\omega + j\,\omega_m)\tau] \end{aligned} \tag{2.38}$$

where ω is the frequency of the Ti:Sa laser, $\phi_1 = \pi\mathcal{V}_0/\mathcal{V}_\pi$ is the amplitude of the phase modulation, and J_j are Bessel functions of the first kind. This electric field has sidebands at multiples of ω_m about the carrier frequency ω, and the weight of each sideband can be adjusted through the modulation voltage $\mathcal{V}_0$. In Fig. 2.6, we plot the sideband power $J_j^2(\pi\mathcal{V}_0/\mathcal{V}_\pi)$ versus the modulation voltage $\mathcal{V}_0$ measured using a Fabry-Perot interferometer. We observe that the carrier ($j = 0$) is entirely suppressed at approximately $\mathcal{V}_0 = 13$ dBm $= 1$ $\mathrm{V_{rms}}$.

The phase-modulated light from the EOM is subsequently split into two Raman beams, as illustrated in Fig. 2.5. Each beam is then passed through an AOM (NEOS 23080-1 for beam 1 and NEOS 23120-1 for beam 2) to servo-control the light intensity. The AOMs also shift the laser frequencies by ω_a in beam 1 and ω_b in beam 2[8]. The Raman fields after the AOMs are therefore expressed as

$$\begin{aligned} E^{(1)}(\tau) &= E^{(1)}\sum_{j=-\infty}^{\infty} J_j(\phi_1)\cos[(\omega + j\,\omega_m + \omega_a)\tau] \\ E^{(2)}(\tau) &= E^{(2)}\sum_{j'=-\infty}^{\infty} J_{j'}(\phi_1)\cos[(\omega + j'\,\omega_m + \omega_b)\tau], \end{aligned} \tag{2.39}$$

[8]In our setup, the nominal frequencies of the AOMs are $\omega_a = (2\pi) \times 80$ MHz and $\omega_b = (2\pi) \times 120$ MHz (the +1 diffracted beam is used in both cases).

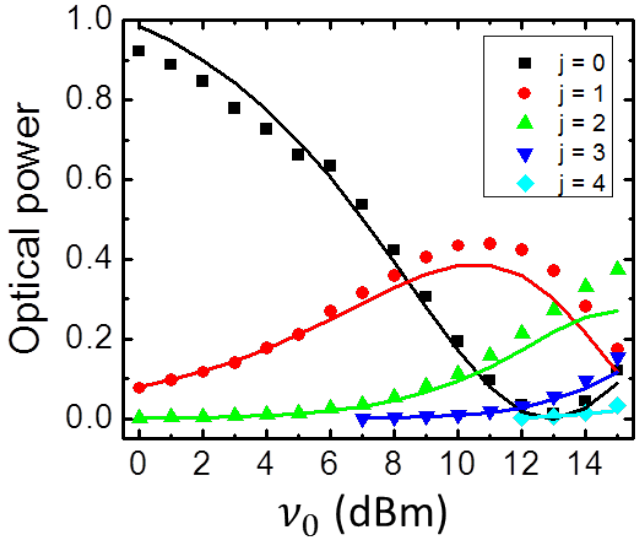

Figure 2.6: Fractional sideband power versus the modulation amplitude $\mathcal{V}_0$ in Eq. 2.37. The EOM is driven at $\omega_m = (2\pi) \times 3337.351305$ MHz. The solid lines are Bessel fits $A\,J_j^2(\pi\mathcal{V}_0/\mathcal{V}_\pi)$ to the experimental data with only two fit parameters (A and $\mathcal{V}_\pi$) for all the sidebands shown. The fit gives $\mathcal{V}_\pi = 1.3$ V_{rms}. Deviation of the fit from the experimental data may arise from nonlinear effects.

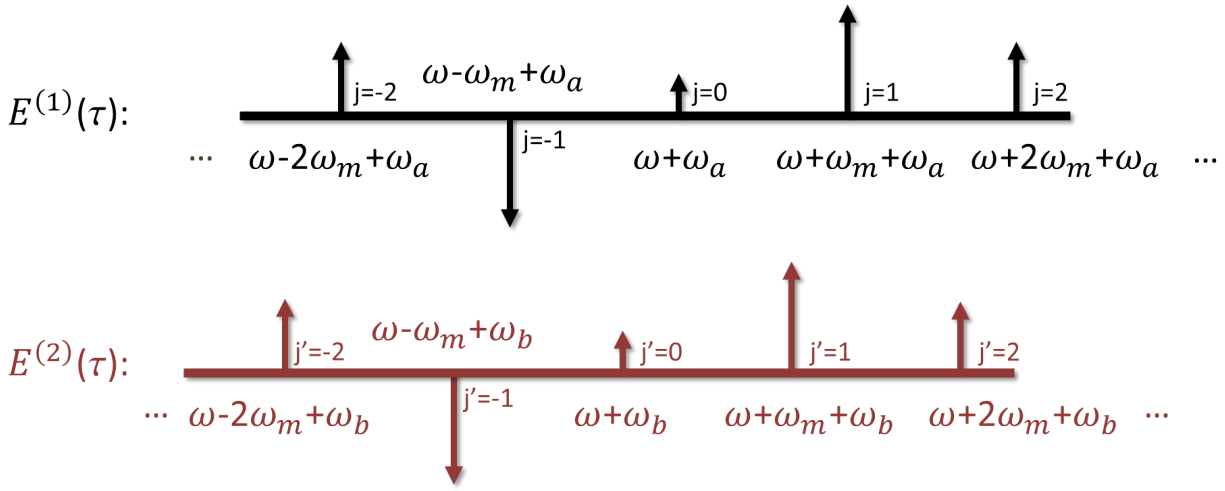

Figure 2.7: Spectrum of the Raman light after phase modulation. The carrier frequency ω is generated by a single-frequency Ti:Sa laser, ω_m is the modulation frequency, and ω_a and ω_b are the frequency shifts induced by the AOMs. The weight of each sideband is $E^{(1)}J_j(\phi_1)/2$ for beam 1 and $E^{(2)}J_{j'}(\phi_1)/2$ for beam 2 (sidebands are not drawn to scale). Negative arrows indicate sidebands out of phase, since $J_{-j}(\phi_1) = (-1)^j J_j(\phi)$.

which have frequency components in the form $\omega_1 = \omega_0 + j\omega_m + \omega_a$ and $\omega_2 = \omega_0 + j'\omega_m + \omega_b$, respectively. The sidebands can be better visualized in the frequency domain. Fig. 2.7 illustrates the Fourier transform of the electric fields in Eq. 2.39. The weight of each sideband is proportional to J_j which, in some cases, is 180° out of phase (indicated by the negative arrows).

In principle, any sideband pair j, j' can be used to drive Raman transitions, as long as their relative frequency $\omega_1 - \omega_2 = (j - j')\omega_m + \omega_a - \omega_b$ matches the targeted frequency ω_0. The resonance frequency ω_0 could represent, for example, the dispersion relation of a free particle, the bandgap between energy bands, the Zeeman shift between magnetic states, or the energy splitting between hyperfine levels. In Chapters 4 and 5, we drive Raman transitions between hyperfine states separated by $\approx (2\pi) \times 6.8$ GHz. In particular, we chose to modulate the EOM at $\omega_m \approx (2\pi) \times 3.4$ and employ sideband pairs with $j - j' = \pm 2$.

In practice, the relative frequency $\omega_1 - \omega_2$ is matched to ω_0 by adjusting ω_m, ω_a, and ω_b. To find the resonant condition, we set $\delta = \omega_1 - \omega_2 - \omega_0$ to zero in Eq. 2.9. If $\omega_0 > 0$, we require that $\omega_1 > \omega_2$, and therefore, $\omega_1 - \omega_2 = 2\omega_m + \omega_a - \omega_b - |\omega_0|$. In the opposite case, if $\omega_0 < 0$, we require that $\omega_1 < \omega_2$, and therefore, $\omega_1 - \omega_2 = -2\omega_m + \omega_a - \omega_b + |\omega_0|$. Both results can be combined as

$$\omega_m = \frac{|\omega_0| \pm (\omega_b - \omega_a)}{2}, \tag{2.40}$$

where the $\pm$ sign corresponds to the case $\omega_1 \gtrless \omega_2$.

We have experimentally optimized the modulation voltage $\mathcal{V}_0$ by driving Raman transitions in a BEC in the dipole trap. The modulation frequency ω_m was set according to Eq. 2.40 and $\mathcal{V}_0$ was adjusted to maximize the excitation fraction. We find that the optimal voltage is $\mathcal{V}_0 = 13$ dBm, which coincides with the voltage at which the carrier vanishes, as shown in Fig. 2.6. We measured the phase noise of the Raman beams by looking at the spectrum of the beat signal. The phase noise is smaller than 1 Hz at FWHM.

2.4.2 Spatial Configuration

In this subsection, we describe the particular spatial beam configuration employed in the experiments reported in Chapters 4 and 5.

The two Raman beams are mutually perpendicular and do not coincide with any of the three lattice directions $\hat{x}$, $\hat{y}$, and $\hat{z}$ (see Figs. 1.2 and 1.5). The beams were aligned to the gas using the same method employed for the lattice beams [66]. The total Raman field from both beams in the $\{\hat{x}_1, \hat{x}_2, \hat{x}_3\}$ basis (see

Section 1.1.1 and Figs. 1.2 and 1.5) is

$$\mathbf{E}(\mathbf{r},\tau) = \sqrt{\frac{2I^{(1)}}{c\varepsilon_0}}\hat{x}_3\cos(k_R\,\hat{x}_2\cdot\mathbf{r}-\omega_1\tau) + \sqrt{\frac{2I^{(2)}}{c\varepsilon_0}}\hat{x}_2\cos(-k_R\,\hat{x}_3\cdot\mathbf{r}-\omega_2\tau), \tag{2.41}$$

where $k_R = 2\pi/\lambda$ is the Raman wavevector and λ_R is the corresponding wavelength. The relative Raman wavevector

$$\Delta\mathbf{k} = \mathbf{k}_1 - \mathbf{k}_2 = k_R\,\hat{x}_2 - (-k_R\,\hat{x}_3) = \sqrt{2}k_R\,\hat{z} \tag{2.42}$$

lies along the lattice direction $\hat{z}$.

Using Eq. 2.17, we decompose the electric fields into spherical components

$$\begin{aligned}
\mathbf{E}^{(1)} &= \sqrt{\frac{2I^{(1)}}{c\varepsilon_0}}\frac{i(\hat{\epsilon}_1+\hat{\epsilon}_{-1})}{\sqrt{2}} \implies E^{(1)}_{\pm1} = i\sqrt{\frac{I^{(1)}}{c\varepsilon_0}} \\
\mathbf{E}^{(2)} &= \sqrt{\frac{2I^{(2)}}{c\varepsilon_0}}\frac{-\hat{\epsilon}_1+\hat{\epsilon}_{-1}}{\sqrt{2}} \implies E^{(2)}_{\pm1} = \mp\sqrt{\frac{I^{(2)}}{c\varepsilon_0}}.
\end{aligned} \tag{2.43}$$

We observe that the electric fields only have $\sigma^{\pm}$ components. The quantization magnetic field $\hat{B}$ in our apparatus is parallel to the vector $\hat{x}_1$ (see Fig. 1.5) and sets the direction $\hat{\epsilon}_0$ of the spherical basis.

The Raman beam waists are approximately 180 μm and 50 μm for beams 1 and 2, respectively. The second beam was recycled from a previous experimental setup which required a beam waist comparable with the gas size (~ 10 μm). Limited optical access along $\hat{x}_2$ has made difficult to upgrade the beam. Variation in the beam intensity across the gas is not ideal for driving Raman transitions because different parts of the gas experience different Rabi rates. Using a numerical calculation that averages over the beam profile, we found that inhomogeneity in the beam intensity results in damping in the Rabi oscillations. Nevertheless, the Raman pulses employed in this thesis are much shorter than the damping time constant observed.

We have experimentally tested the Rabi rate predicted by Eq. 2.21. The measured Rabi rate with $P_1 = 930$ μW, $P_2 = 72$ μW, and $\Delta = 200$ GHz (from D_1) is $\Omega = (2\pi)\times 2$ kHz. The rate calculated from Eq. 2.21 is $\Omega = (2\pi)\times 4.7$ kHz. The discrepancy may be explained by uncertainty in the beam waists and loss of optical power on optical elements, such as the surface of the atom chamber.

In Fig. 2.8, we show Rabi oscillations in a BEC in both a harmonic trap and a lattice potential. The gas is driven by a pair of Bragg beams which couple states in the same hyperfine level $|F=1, m_F=-1\rangle$. In these plots, the spatial configuration of the Bragg beams is $\hat{k}_1 = -(\hat{x}_1+\hat{x}_3)/\sqrt{2}$ and $\hat{k}_2 = -\hat{x}_1$, which differs from that used throughout this thesis (described in Eq. 2.41). The momentum impulse experienced by the gas is $\Delta k = 0.5\,\pi/d$ and does not lie along any of the three lattice directions. In part (a), the BEC is

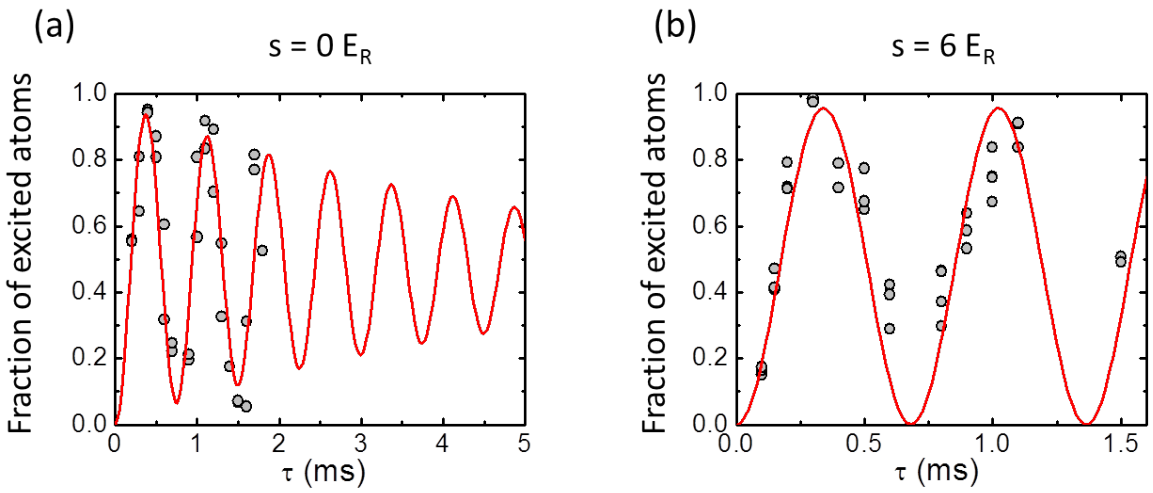

Figure 2.8: Rabi oscillations experienced by a BEC in $|F = 1, m_F = -1\rangle$ driven by Bragg beams. The beams change the momentum of the gas by $\Delta k = 0.5\,\pi/d$. (a) Rabi oscillation in a harmonic trap. The measured Rabi rate with $\Delta = 1000$ GHz, $\delta = 0$, $P_1 = 170$ μW, and $P_2 = 220$ μW is $\Omega = (2\pi) \times 1.3$ kHz. (b) Rabi oscillation in a $s = 6$ E_R lattice potential. The measured Rabi rate between $n = 0$ and $n' = 1$ with $\Delta = 500$ GHz, $\delta = 0$, $P_1 = 390$ μW, and $P_2 = 530$ μW is $\Omega = (2\pi) \times 1.5$ kHz. Both Rabi rates (normalized by $\sqrt{P_1 P_2}/\Delta$ to account for different power and detuning) differ by a factor of 0.23, which is approximately the Franck-Condon factor at $\Delta k = 0.5\,\pi/d$ shown in (a) of Fig. 2.3. A damped sine-squared function is fit to the data points.

confined in a harmonic trap. The gas is initial centered around $|p = 0\rangle$ and is coupled by the Bragg beams with the momentum states around $|p = \hbar\Delta k\rangle$. In (b), the BEC is confined in a 6 E_R lattice potential. The gas is initially centered around $|n = 0, q = 0\rangle$ and coupled with the quasimomentum states around $|n' = 1, q = \hbar\Delta k\rangle$. Inhomogeneity in the Bragg beam intensity damps the Rabi oscillations.

Chapter 3

Quantum Quench of a Mott Insulator

3.1 Introduction

The study of non-equilibrium phase transitions is wide ranging, touching on topics as diverse as the formation of structures in the early Universe [32] and the practicality of adiabatic quantum computing [31]. The so-called Kibble-Zurek mechanism (KZM) has been used to understand some universal features—principally the rate of topological defect formation—of quenches across classical phase transitions [32,34]. "Quench" in this context refers to rapidly varying a thermodynamic parameter in order to drive the system across the critical point of a phase transition and out of equilibrium for a finite time. The KZM has successfully been tested for classical transitions by numerical simulations of the time-dependent Ginzburg-Landau model [130–137] and by experiments in a wide range of condensed matter systems, such as liquid crystals [138], superfluid ^{3}He [139,140], superconductors [141,142], non-equilibrium convection systems [143,144], and dilute atomic gases driven through the Bose-Einstein condensation transition [145,146]. The Kibble-Zurek theory has recently been extended to quantum phase transitions [147–158] (for reviews articles, see Refs. [30,159–162]). In contrast to the classical case, quantum phase transitions involve closed quantum mechanical evolution at zero temperature, for which quenches are accomplished by varying a parameter in the Hamiltonian in order to tune between different quantum phases [163].

3.2 The Quantum Kibble-Zurek Mechanism

When a system undergoes a continuous phase transition from a disordered symmetric phase to an ordered broken-symmetry phase, it is observed that, regardless of how slowly the process is driven, defects develop in the new phase with a characteristic size and density that depend on the transition rate. Such excitations arise because divergence of the relaxation time at the critical point (phenomenon known as critical slowing down) prevents an adiabatic passage across the phase boundary [163,164]. In this section, we will introduce the quantum Kibble-Zurek mechanism which, similarly to the classical version, provides a framework for

predicting scaling relations for defect generation after a quantum phase transition. Specifically, the KZM predicts power laws for the excitation density and correlation length as a function of the transition rate, while scaling laws for other physical quantities can be derived via dimensional analysis. The KZM described in this section is in its "canonical" form, this is, when the system experiences a phase transition between two gapped phases. The principles behind this particular case can be extended to other quantum phase transitions [30], such as the MI-to-SF transition in the BHM.

According to critical phenomena, as a system approaches the critical point, the relaxation time τ_0 and the correlation length of the order parameter ξ increase as

$$\tau_0 \sim |\epsilon|^{-\nu z} \quad \text{and} \quad \xi \sim |\epsilon|^{-\nu}, \tag{3.1}$$

where

$$\epsilon = (g - g_c)/g_c \tag{3.2}$$

is a dimensionless parameter that measures the distance of the tuning parameter g from the critical point g_c, and ν and z are universal critical exponents[1]. Because τ_0 diverges as ϵ approaches to zero, dynamics of the system comes to a halt nearby the critical point, and therefore, if the system starts from a disordered phase, a mosaic-like state comprised of domains of the new ordered phase will develop, since long wavelength excitations cease to be adiabatic. The orientation of the order parameter in each domain is approximately constant, but different domains are uncorrelated. As time evolves, the system is assumed to remain in this frozen state while it crosses the critical point, and dynamics does not resume until the relaxation time τ_0 decreases to a finite value. Once dynamics resumes, the system starts time-evolving from an excited state. This framework is termed the adiabatic-impulse-adiabatic approximation and is illustrated in Fig. 3.1.

Quantitatively, the KZM postulates that the crossover from the adiabatic stage to the impulse stage occurs when the relative transition rate $|\epsilon^{-1} d\epsilon/d\tau|$ and the relaxation rate $\tau_0^{-1} \sim |\epsilon|^{\nu z}$ are equal, this is, when

$$\left| \frac{1}{\epsilon} \frac{d\epsilon}{d\tau} \right| \sim |\epsilon|^{\nu z}. \tag{3.3}$$

In order to introduce time dependence into Eq. 3.3, the tuning parameter ϵ is assumed to be a continuous function of time and linearizable about $\tau = 0$, namely

$$\epsilon(\tau) \approx -\frac{\tau}{\tau_Q}, \tag{3.4}$$

[1] In critical phenomena, the correlation length scales with ϵ as $\xi \sim |\epsilon|^{-\nu}$ and the relaxation time τ_0 scales with the correlation length as $\tau_0 \sim \xi^z$. See, for example, Refs. [163, 164].

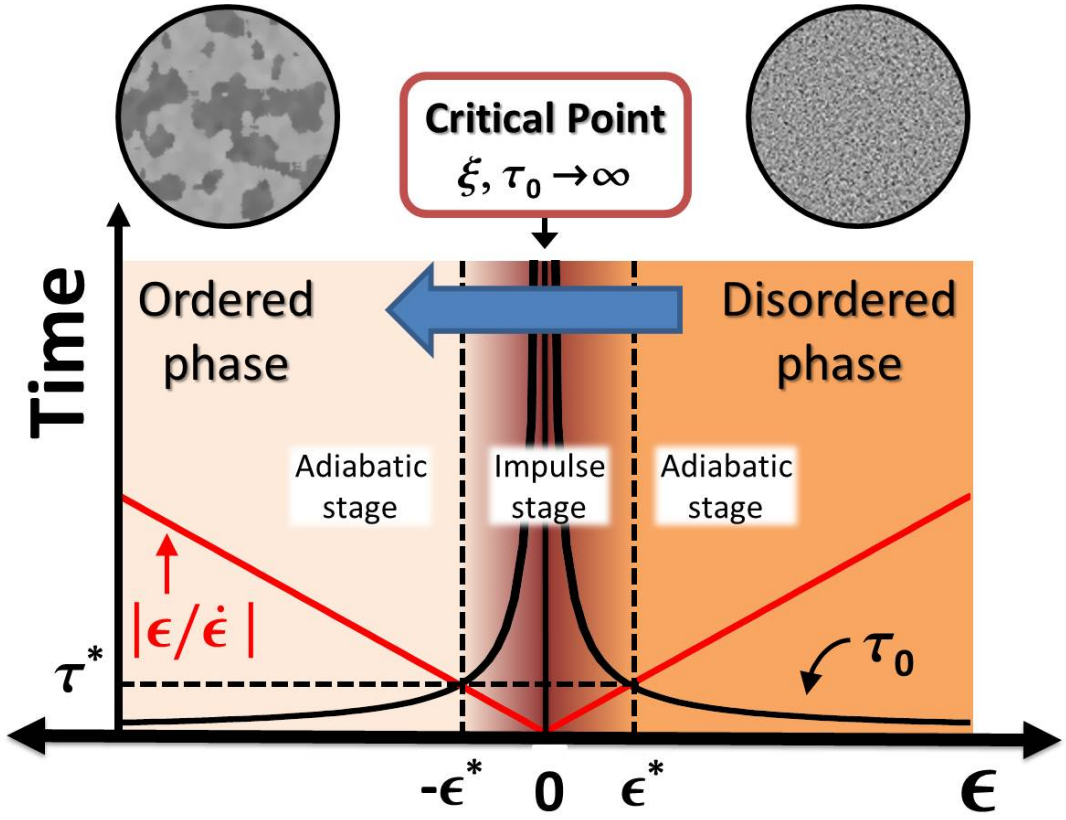

Figure 3.1: Illustration of critical slowing down and the adiabatic-impulse-adiabatic approximation during a continuous phase transition between two gapped phases. The black line is $\tau_0 \sim |\epsilon|^{-\nu z}$ (the relaxation time) and the red line is $|\epsilon/\dot{\epsilon}|$ (the inverse of the transition rate). The critical point $\epsilon = 0$ is characterized by divergent correlation length ξ and relaxation time τ_0. The complex dynamics of the phase transition is approximated by an impulse regime surrounded by two adiabatic stages. During the impulse stage, the dynamics of the system is frozen, and therefore, the system is quenched from the disordered phase to the ordered phase. Figure adapted from Ref. [30].

where $\tau_Q = |\dot{\epsilon}(0)|^{-1}$ is the quench time and $1/\tau_Q$ is the quench rate. Without loss of generality, we have assumed that the system crosses the critical point at time $\tau = 0$ from $\epsilon > 0$ to $\epsilon < 0$. After substituting $\epsilon(\tau)$ into Eq. 3.3 and solving for τ, one finds that the "freeze up" time τ^* scales as

$$\tau^* \sim \tau_Q^{\frac{\nu z}{1+\nu z}}. \tag{3.5}$$

At this exact time, ϵ scales as

$$\epsilon^* = \epsilon(\tau) \sim \left(\frac{1}{\tau_Q}\right)^{\frac{1}{1+\nu z}}. \tag{3.6}$$

The parameter ϵ^* defines the left and right boundaries of the impulse stage, as illustrated in Fig. 3.1. The correlation length ξ^*, which remains constant during the impulse stage, scales as

$$\xi^* \sim |\epsilon^*|^{-\nu} \sim \tau_Q^{\frac{\nu}{1+\nu z}}. \tag{3.7}$$

A scaling relation for the density of excitations results from the dimensional analysis $n_{\text{ex}} \sim (\xi^*)^{-D}$, where D is the spatial dimensionality of the system. The KZM therefore predicts

$$n_{\text{ex}} \sim \left(\frac{1}{\tau_Q}\right)^{\frac{D\nu}{1+\nu z}}. \tag{3.8}$$

At finite temperature, the classical version of the KZM incidentally leads to the same results in Eqs. 3.7 and 3.8. However, defects are generated through thermal fluctuations and not through quantum fluctuations, as in the quantum KZM [30].

The scaling laws found in Eqs. 3.7 and 3.8 predict that the defect size ξ^* shrinks and the excitation density n_{ex} increases as the quench rate $1/\tau_Q$ increases (i.e., for faster quenches). The decrease in ξ^* can be understood by analyzing the parameter ϵ^* (Eq. 3.6), which sets the boundaries of the impulse stage. A fast quench implies a wide impulse region, and therefore, the system freezes up at a far distance from the critical point where correlation has not built up considerably.

While the KZM has been successfully tested for classical transitions, experimental studies of quantum quenches in the context of the KZM has been scant. Experiments are needed for verifying, for example, the scaling of defect density with the transition rate in various quantum systems. Notably, there is evidence that the formation of ferromagnetic domains in a spin-1 Bose-Einstein condensate can be attributed to a quantum quench [165]. More recently, emergence of coherence in a quenched 1D Mott-insulator-to-superfluid transition has been investigated [166].

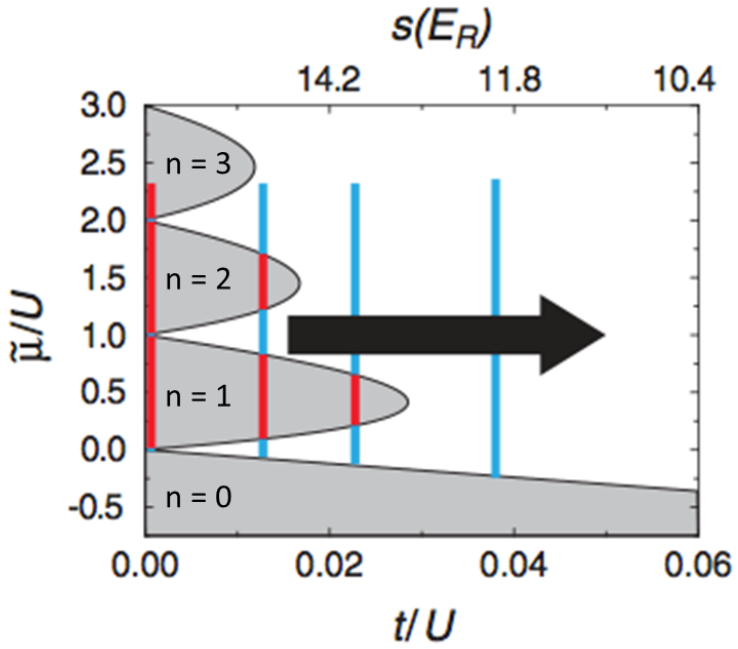

Figure 3.2: Phase diagram of the Bose-Hubbard model at zero temperature [169] showing the MI phase (grey area), the SF phase (white area), and the quench across the phase boundary (arrow). The vertical lines illustrate that the trapped gas samples a range of densities and effective chemical potentials $\tilde{\mu}$ in the LDA [170]. MI regions in the gas are colored red and SF blue. The quench is accomplished by rapidly reducing s, and thereby increasing t/U.

3.3 Hubbard Lattice Quench

In this chapter, we perform quantum quenches with atoms confined in an optical lattice. The lattice-bound atoms realize the Bose-Hubbard Hamiltonian defined in Eq. 1.12 with the tunneling and interaction energies t and U, respectively. In contrast to previous experiments on the superfluid-to-Mott-insulator transition [167, 168], we quench from the Mott insulator (MI) to the superfluid (SF) state, and we systematically investigate the formation of excitations as the quench amplitude and rate are varied.

Quenching across the MI-SF phase boundary is accomplished by adjusting the lattice potential depth s dynamically in such a way to transform the gas between equilibrium configurations with and without atoms in the MI phase present. While quenches are possible on all relevant time scales, we explore quenches that occur at rates

$$\frac{1}{\tau_Q} = \frac{d}{d\tau}\left(\frac{t}{U}\right) \tag{3.9}$$

that are too slow to excite atoms into higher vibrational states in the lattice potential (the bandgap between vibrational states sets the limiting time scale, and in our system is typically on the order of a few tens of μs). How $1/\tau_Q$ compares with U/h and t/h is complicated because the phase boundary is crossed at

a range of densities across the trap (represented by the vertical line in Fig. 3.2). Therefore, the Hubbard energies U_c and t_c at the phase transition change during the quench. Despite this, the quench rate is always slow compared with U_c, since $1/\tau_Q$ varies from $(0.001 - 0.2)\, U_c/h$. The quench rate is not consistently fast or slow compared with t_c or the confining trap frequencies. For our fastest quenches, the quench rate is $1/\tau_Q = (10 - 100)\, t_c/h$, which is always fast compared with t_c/h. For the slowest quenches, the rate is $1/\tau_Q = (0.01 - 1)\, t_c/h$, which is comparable to or slower than t_c/h. For intermediate speeds, $1/\tau_Q$ may be fast compared with t_c/h at the beginning of the quench (at $s = 25$ $\mathrm{E_R}$) and slow at the end.

We start the experiment by preparing a BEC in the hybrid dipole trap with $(161 \pm 13) \times 10^3$ atoms and condensate fraction higher than 90%. The dipole trap configuration and the evaporation method are detailed in Section 1.1.1. A cubic spin-independent optical lattice with wavelength $\lambda = 812$ nm (which is far red-detuned from the resonance frequencies in ^{87}Rb) is slowly superimposed onto the BEC in 100 ms. The lattice potential is described by Eq. 1.9 in the spin-independent configuration ($\theta = 0°$). Given the gas size and overall confining potential in our experiment, the maximum $\tilde{\mu}$ is roughly fixed at $2U$ for the measurements described here, which corresponds to a central filling (particles per lattice site) of $\mathbb{n} \approx 4$ atoms per site at low s and a central MI with $\mathbb{n} \approx 3$ atoms per site at high s according to a site-decoupled mean field calculation (Appendix F). The measured geometric mean of the trap frequencies is (43 ± 2) Hz at $s = 0$. We estimate, using Eq. 1.19, that the additional confinement from the lattice beams increases the mean frequency to (82 ± 6) Hz at $s = 25$ $\mathrm{E_R}$. The aspect ratio of the trap changes from 1:1.3:1.8 to 1:1:1.2 across the same range.

3.3.1 Defect Formation

We investigate excitation generation by varying the fraction of atoms crossing the MI-SF phase boundary. We quench the lattice depth from a variable initial value s_0 to the fixed final depth $s = 4$ $\mathrm{E_R}$ for all data. The initial depth ranges from $s_0 = 25$ $\mathrm{E_R}$ (t/U= 0.002) to $s_0 = 4$ $\mathrm{E_R}$. At $s_0 = 25$ $\mathrm{E_R}$ ($t/U \ll 1$), the gas is deep in the MI phase; at $s_0 = 4$ $\mathrm{E_R}$ ($t/U \approx 1$), the gas is deep in the SF phase. The timeline of the experiment is illustrated in Fig. 3.3. At high s_0, nearly all the atoms start in the MI phase with fillings ranging from 1 to 3 particles per site, and therefore, almost all the atoms cross the phase boundary. In contrast, at low enough s_0, all the atoms are in the SF phase and, consequently, no atoms cross the phase boundary.

The lattice depth is linearly quenched over 5 ms for all data. The quench time was chosen so that the finite excitation lifetime has little effect on the experiment. The ratio t/U and the quench rate $1/\tau_Q$ change

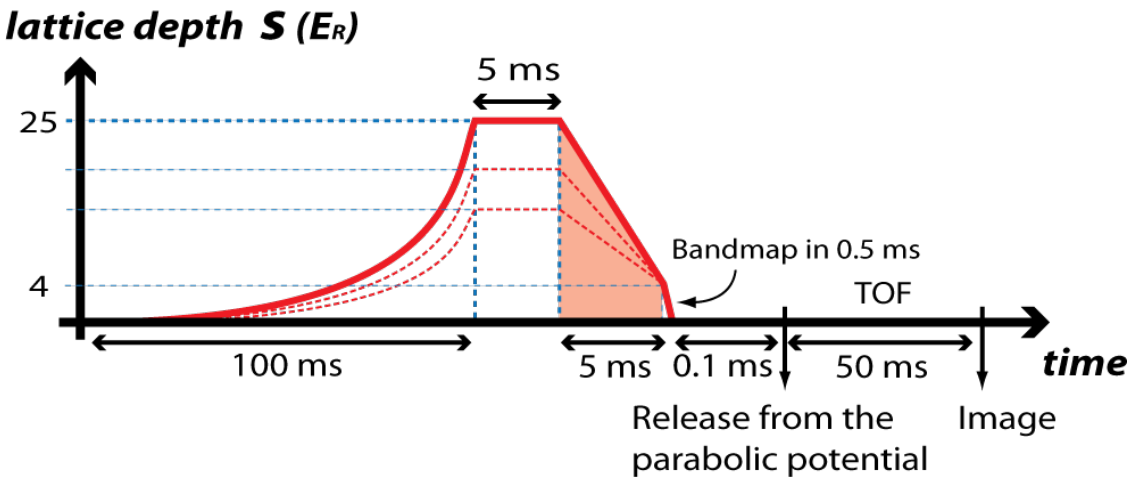

Figure 3.3: Experimental sequence for a linear quench in s (not to scale). The ultracold gas is adiabatically loaded into the optical lattice in 100 ms using an exponential ramp. The lattice potential is then linearly quenched in 5 ms (shaded area) from a variable initial depth $s_0 = (4 - 25)$ $\mathrm{E_R}$ to the fixed value $s = 4$ $\mathrm{E_R}$. Absorption images are taken after 50 ms of TOF. The solid and red-dotted lines indicate some of the possible paths that the lattice depth can follow.

nonlinearly during this quench, namely

$$\frac{t}{U} \propto e^{-2\sqrt{s/\mathrm{E_R}}}. \tag{3.10}$$

This expression results from using approximated analytic forms for the Hubbard energies in the large s limit [171], specifically

$$\begin{aligned} t &\approx \frac{4\ \mathrm{E_R}}{\sqrt{\pi}} \left(\frac{s}{\mathrm{E_R}}\right)^{3/4} e^{-2\sqrt{s/\mathrm{E_R}}} \\ U &\approx \sqrt{\frac{8}{\pi}} k a_s \left(\frac{s}{\mathrm{E_R}}\right)^{3/4} \mathrm{E_R}, \end{aligned} \tag{3.11}$$

where $k = 2\pi/\lambda$ is the wavevector of the lattice beams, a_s is the s-wave scattering length, and s is in units of $\mathrm{E_R} = \hbar^2 k^2 / 2m$.

After the quench, the lattice is bandmapped in 500 μs and the gas is released from the hybrid dipole trap for a period of free expansion, which converts phase gradients related to topological or wavelike excitations into large density fluctuations [172–174]. In order to resolve defects in the gas, absorption images are taken after a relatively long 50 ms of TOF, which expands the Thomas-Fermi radius of the condensate from ≈ 10 μm to ≈ 100 μm. A magnetic field gradient is applied to support the atoms against gravity. The bandmapping technique (discussed in Section 1.1.6) improves the low imaging signal-to-noise ratio resulting from the long expansion times employed for these measurements.

In Fig. 3.4, we display typical absorption images after TOF of quenches from different initial lattice depths. A condensate is present after the quench under all circumstances, and the condensate fraction varies

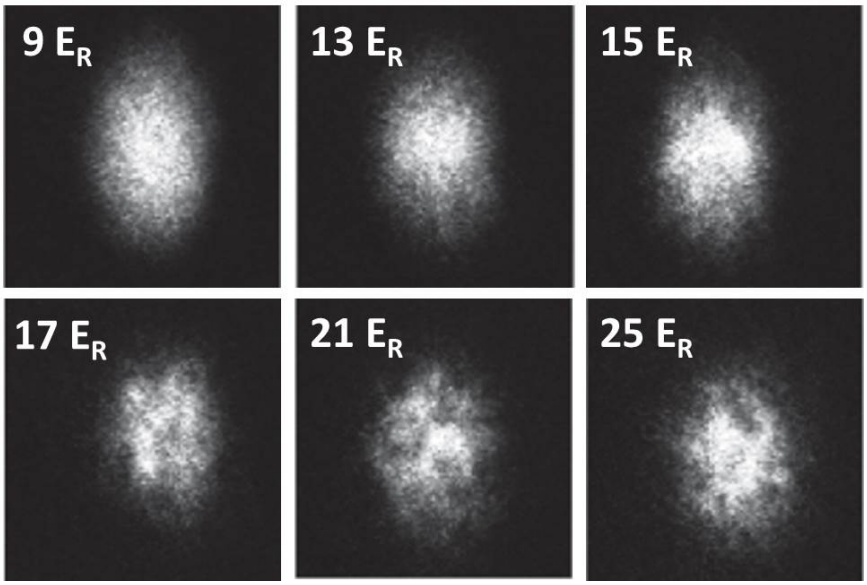

Figure 3.4: Typical absorption images after quenching the lattice potential from different initial depths (brighter areas indicate higher atomic density). The gas is allowed to expand for 50 ms to resolve defects in the gas. Perturbations to a smooth density profile emerge when the system crosses the MI-SF phase boundary.

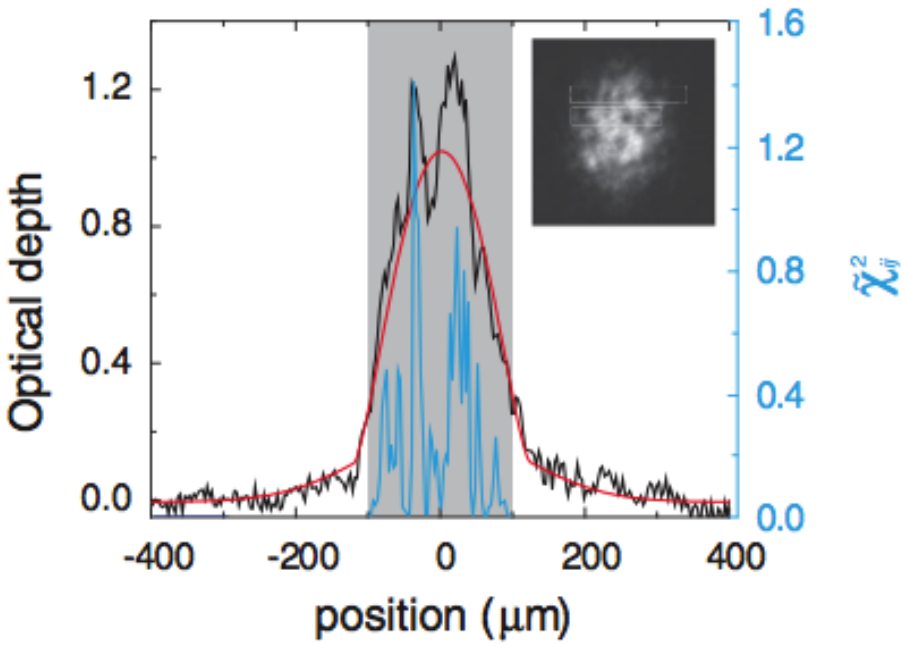

Figure 3.5: Slice (black line) through a typical absorption image (inset) taken after a lattice quench from $s_0 = 25$ E_R. The image is fit to a smooth profile (red line), which is used to determine the deviation $\tilde{\chi}^2_{ij}$ at each pixel (blue line) in a masked region (gray area) with $\mathcal{OD}_{ij} \gtrsim 0.2$.

from 0.35 to 0.6 across all the data. We observe that, when the quench start from a lattice depth below $s \approx 13\ \mathrm{E_R}$, the gas has a smooth profile. In contrast, defects develop for deep quenches. Based on mean field calculations, the tip of the unit filling lobe in the Bose-Hubbard phase diagram (Fig. 3.2) is located at $s = 13.6\ \mathrm{E_R}$ ($t/U \approx 0.03$) [71, 163, 169], which implies that below this critical lattice depth the gas is purely in the SF phase. The presence of defects for $s_0 \gtrsim 13\ \mathrm{E_R}$ suggests that quasiparticle and topological excitations emerge from atoms crossing the phase boundary.

Topological excitations (e.g. vortices) are oriented randomly with respect to the imaging direction and, sometimes, we see them clearly, as shown in the images in Fig. 3.4 and in the density profile in Fig. 3.5.

3.3.2 Excitation Measurement

We determine the amount of excitation produced during the quench by measuring the deviation of the absorption images from a smooth profile. We fit each absorption image to a smooth function that is a combination of a gaussian and a Thomas-Fermi profile (defined in Eq. 1.20). We find that all the images used in the experiment are well described by this fit, as observed in the slice through a typical image in Fig. 3.5.

We amount excitation in the gas through[2]

$$\tilde{\chi}^2 = \sum_{ij} \tilde{\chi}^2_{ij} = \alpha \, \frac{\sum_{ij} (\mathcal{OD}_{ij} - f_{ij})^2 / 2 f_{ij}}{\sum_{ij} \mathcal{OD}_{ij}}, \tag{3.12}$$

where i and j index the pixels in the image $\mathcal{OD}_{ij}$, f_{ij} is the smooth profile obtained from the fit, and α is a proportionality constant that compensates for attenuation in the measured excitation level because of column integration along the imaging axis. In Section 3.3.3, we have estimated α through numerical simulations, and we found that $\tilde{\chi}^2$ accurately reproduced the fraction of Bogoliubov excitations in a trapped condensate.

The sum in Eq. 3.12 is constrained to an area in the image with

$$\frac{\mathcal{OD}_{ij}}{\langle \delta \mathcal{OD} \rangle_{\mathrm{rms}}} > 5, \tag{3.13}$$

where $\langle \delta \mathcal{OD} \rangle_{\mathrm{rms}} = 0.044$ is the root-mean-square imaging noise measured from absorption images without the gas present. The imaging noise, readily observable in the background of the main figure in Fig. 3.5, arises primarily from shot noise on the CCD camera, as we will discuss in Section 3.3.4. The optimal signal-to-noise ratio used in Eq. 3.13 was found by maximizing $\tilde{\chi}^2$ when excitations are present and, at the same

[2]The symbol $\tilde{\chi}^2$ used for the expression defined in Eq. 3.12 does not have any statistical meaning.

time, minimizing $\tilde{\chi}^2$ when excitations are absent and the gas profile is smooth.

The quantity $\tilde{\chi}^2$ is chosen such that it measures the fraction of excited atoms in a weakly interacting trapped gas. The physical meaning of $\tilde{\chi}^2$ can be understood most straightforwardly for a one-dimensional non-interacting gas. In this case, the density profile after a sufficiently long TOF is the momentum distribution (in the momentum-space representation)

$$n(p) = |\Psi(p)|^2 = |\Psi_0(p) + \delta\Psi(p)|^2, \tag{3.14}$$

where $\delta\Psi(p)$ is a small deviation from the condensate wavefunction in the ground state

$$\Psi_0(p) = \sqrt{n_0(p)}. \tag{3.15}$$

After neglecting the second order term $|\delta\Psi|^2$ in Eq. 3.14, the momentum distribution becomes

$$n(p) = n_0(p) + \sqrt{n_0(p)}[\delta\Psi(p) + \delta\Psi^\dagger(p)], \tag{3.16}$$

and therefore,

$$\frac{[n(p) - n_0(p)]^2}{n_0(p)} = 2|\delta\Psi(p)|^2 + \Psi^2(p) + \Psi^{\dagger 2}(p). \tag{3.17}$$

In the particular case of Bogoliubov excitations, it can be shown that the last two terms in Eq. 3.17 are exactly zero after averaging over random excitation phases and integrating over momentum. Bogoliubov excitations in a uniform BEC are expressed as wavefunctions in the form (in the position-space representation) [71]

$$\delta\Psi_{\mathbf{k}}(\mathbf{r}) = \sqrt{n_0}\left[u_k e^{i(\mathbf{k}\cdot\mathbf{r}-\phi)} - v_k e^{-i(\mathbf{k}\cdot\mathbf{r}-\phi)}\right], \tag{3.18}$$

where n_0 is the gas density, ϕ is the phase of the excitation, and u_k and v_k are coefficients expressed by

$$\begin{aligned} u_k^2 &= \frac{1}{2}\left(\frac{\varepsilon_k + g\,n_0}{\varepsilon_k} + 1\right) \\ v_k^2 &= \frac{1}{2}\left(\frac{\varepsilon_k + g\,n_0}{\varepsilon_k} - 1\right), \end{aligned} \tag{3.19}$$

which depend on the excitation wavevector $k = |\mathbf{k}|$. The excitation energy is given by

$$\varepsilon_k = \sqrt{\frac{\hbar^2 k^2}{2m}\left(\frac{\hbar^2 k^2}{2m} + 2g\,n_0\right)} \tag{3.20}$$

and the interaction parameter for the Bose gas is $g = 4\pi\hbar^2 a_s/m$.

The number of excited atoms in the condensate is therefore given by

$$\int dp\,|\delta\Psi(p)|^2 = \int dp\,\frac{[n(p)-n_0(p)]^2}{2n_0(p)} \tag{3.21}$$

after averaging over random phases ϕ. We identify Eq. 3.21 with the numerator of $\tilde{\chi}^2$ defined in Eq. 3.12, apart from the absorption cross-section σ that relates $\mathcal{OD}$ with $n(p)$. The denominator of Eq. 3.12, on the other hand, is proportional to the total number of atoms $\int dp\,n_0(p)$. Therefore, $\tilde{\chi}^2$ is naturally interpreted as the fraction of excited atoms in the weakly interacting regime.

3.3.3 Determination of α via Numerical Simulation

In the previous section, we concluded that $\tilde{\chi}^2$ is the fraction of excited atoms in a one-dimensional condensate. This interpretation can be trivially extended to a three-dimensional system. In practice, however, absorption imaging hinders such straightforward interpretation given that excitations in the gas are projected onto the imaging plane. In order to relate excitations present in the gas with excitations observed in the imaging plane, we adopt a practical approach by numerically comparing the measure $\tilde{\chi}^2$ against simulated Bogoliubov excitations in a 3D weakly interacting BEC under similar experimental conditions.

We start the simulation by finding the ground-state wavefunction Ψ_0 of a condensate at equilibrium in an isotropic harmonic potential $V(\mathbf{r}) = m\omega^2\mathbf{r}^2/2$. The mean trap frequency is $\omega = (2\pi)\times 40$ Hz and the total atom number is $N = 1.5\times10^5$. We find Ψ_0 by numerically solving the 3D time-independent Gross-Pitaevskii Equation (GPE) for a BEC at zero temperature [71]

$$-\frac{\hbar^2}{2m}\nabla^2\Psi_0(\mathbf{r}) + V(\mathbf{r})\Psi_0(\mathbf{r}) + g|\Psi_0(\mathbf{r})|^2\Psi_0(\mathbf{r}) = \mu\Psi_0(\mathbf{r}), \tag{3.22}$$

where the spatial coordinates are discretized using a $128\times128\times128$ grid over a finite volume of $(100\ \mu\text{m})^3$. We employ a time-splitting spectral method that computes the solution in small steps and treats the linear part of the GPE in the time domain and the nonlinear part in the frequency domain. Details regarding this method are presented in Appendix B. The simulation results in a gas with a Thomas-Fermi density profile with an approximate radius of 10 μm.

To simulate quasiparticle excitations present in the condensate after quenching the lattice depth, we imprint excitations on the condensate by introducing a small deviation $\delta\Psi_{\mathbf{k}}(\mathbf{r})$ to the ground state $\Psi_0(\mathbf{r})$. For $\delta\Psi_{\mathbf{k}}(\mathbf{r})$, we consider Bogoliubov excitations defined by Eq. 3.18. Because Eq. 3.18 is valid only for a uniform system, we assume excitations with wavelength shorter than the size of the gas and we write the

gas wavefunction $\delta\Psi_{\mathbf{k}}(\mathbf{r})$ under a local density approximation in the form

$$\delta\Psi_{\mathbf{k}}(\mathbf{r}) = \Psi_0(\mathbf{r}) \left[u_k e^{i(\mathbf{k}\cdot\mathbf{r}-\phi)} - v_k e^{-i(\mathbf{k}\cdot\mathbf{r}-\phi)} \right]. \tag{3.23}$$

The wavefunction of the excited gas is therefore formulated as

$$\Psi(\mathbf{r}) = \sqrt{1 - \frac{N_{\mathrm{ex}}}{N}}\, \Psi_0(\mathbf{r}) + \sqrt{\frac{N_{\mathrm{ex}}}{N}}\, \delta\Psi_{\mathbf{k}}(\mathbf{r}), \tag{3.24}$$

where the ratio N_{ex}/N represents the fraction of excited atoms in the condensate and the wavefunctions $\Psi_0(\mathbf{r})$ and $\delta\Psi_{\mathbf{k}}(\mathbf{r})$ are normalized to the total atom number N. In the simulation, we have assumed small N_{ex}/N to ensure validity of the Bogoliubov equations and the LDA.

In analogy to TOF imaging, the confining potential is instantly switched off (i.e., $V(\mathbf{r}) = 0$) and $\Psi(\mathbf{r})$ is time-evolved using the time-dependent GPE

$$\left[-\frac{\hbar^2}{2m}\nabla^2 + V(\mathbf{r}) - \mu + g|\Psi(\mathbf{r},\tau)|^2 \right] \Psi(\mathbf{r},\tau) = i\hbar\frac{\partial}{\partial\tau}\Psi(\mathbf{r},\tau), \tag{3.25}$$

which we numerically solve using the same time-splitting spectral method aforementioned.

The measure $\tilde{\chi}^2$ is calculated from the gas density $|\Psi(\mathbf{r},\tau)|^2$ after integration along the imaging line of sight. In Fig. 3.6 we show the result from the numerical simulation, where the range of excitation fractions and excitation wavelengths probed are $N_{\mathrm{ex}}/N = 0.02 - 0.1$ and $k = (0.8 - 3)\ \mu\mathrm{m}^{-1}$, respectively, and each point is averaged over 10 relative phases ϕ uniformly distributed over 0 and 2π. Fig. 3.6 shows that $\tilde{\chi}^2$ depends linearly on the excitation fraction N_{ex}/N. We conclude that $\tilde{\chi}^2$ is proportional to the fraction of excited particles present in the gas and it is independent of the excitation wavevector (within the range of validity of the LDA). Therefore, under the fit parameter $\alpha = 10.7 \pm 0.2$, $\tilde{\chi}^2$ is equal to the fraction of excited atoms in the gas. This numerical method, however, is only valid at zero temperature and does not properly account for trap-length-scale excitations or topological excitations such as vortices [175], which are evident in Fig. 3.4.

3.3.4 Testing the Kibble-Zurek Mechanism

In Fig. 3.7, we plot $\tilde{\chi}^2$ versus the lattice depth s_0 from which the quench is initiated. As we concluded in the previous section, $\tilde{\chi}^2$ is interpreted as the fraction of excited atoms in the gas. We observe that, below the emergence of the unit filling MI phase at $s_0 \approx 13\ \mathrm{E_R}$, the measure $\tilde{\chi}^2$ is constant at $\tilde{\chi}^2_0 \approx 0.06$ (determined by averaging $\tilde{\chi}^2$ over data points with $s_0 \leq 12\ \mathrm{E_R}$); whereas above $s_0 \approx 13\ \mathrm{E_R}$, the degree of excitation

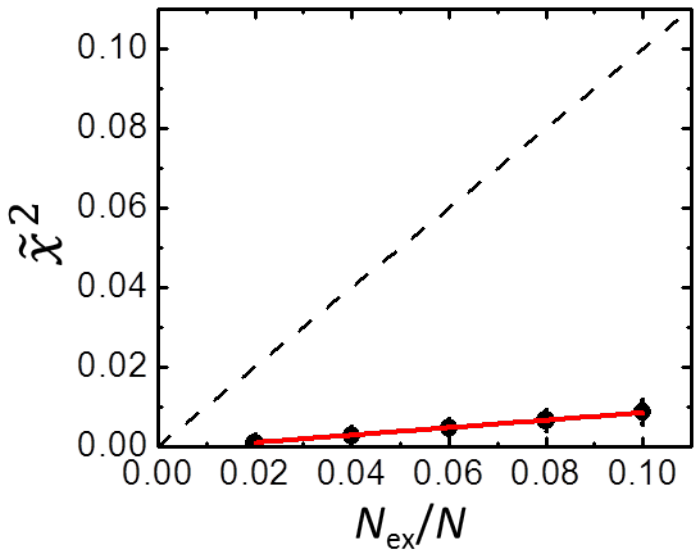

Figure 3.6: Numerical simulation of the measured excitation level $\tilde{\chi}^2$ versus the fraction of excited atoms $N_{\rm ex}/N$ introduced to the condensate. The measure $\tilde{\chi}^2$ is computed according to Eq. 3.12 with $\alpha = 1$. Each data point is averaged over excitation phases that range from $\phi = 0 - 2\pi$ and wavevectors that range from $k = (0.8 - 3)\ \mu\text{m}^{-1}$. The error bars show the standard deviation. The TOF employed is 10 ms, which was limited by the grid size. The slope of the linear fit (red line) is 0.093 ± 0.002. The dashed line has a slope of 1 and is shown to guide the eye.

grows until $\tilde{\chi}^2$ saturates to approximately 0.17 at high lattice depths, for which more than 90% of the atoms are in the MI phase before the quench.

The offset $\tilde{\chi}_0^2$ in Fig. 3.7 is consistent with imaging noise present in the absorption images[3]. The numerical value of $\tilde{\chi}_0^2$ can be roughly estimated from the definition of $\tilde{\chi}^2$ in Eq. 3.12. If we consider that the mean imaging noise is $\langle \delta\mathcal{OD} \rangle_{\rm rms} \approx 0.044$ and the mean optical depth of an image is $\langle f_{ij} \rangle \approx 0.6$ (see, for example, Fig. 3.5), we estimate an offset $\tilde{\chi}_0^2 \approx \alpha\,(0.044/0.6)^2 \approx 0.054$, which is comparable with the value observed in the plot.

The red line in Fig. 3.7 shows the fraction of atoms in the MI phase before the quench, which we have determined according to a zero-temperature mean-field calculation in the LDA [170] (see Appendix F). We observe that the fraction of excited atoms measured by $\tilde{\chi}^2$ is proportional to the fraction of atoms in the MI phase, which is identical to the overall fraction of atoms crossing the SF-MI phase boundary. Given that in the KZM only the regions of the lattice crossing the phase boundary give rise to excitations, the direct relation between the fraction initially in the MI phase and the degree of excitation is strong evidence that a Kibble-Zurek-like mechanism is responsible for generating excitations during the quench.

[3]The dominant source of imaging noise is shot noise.

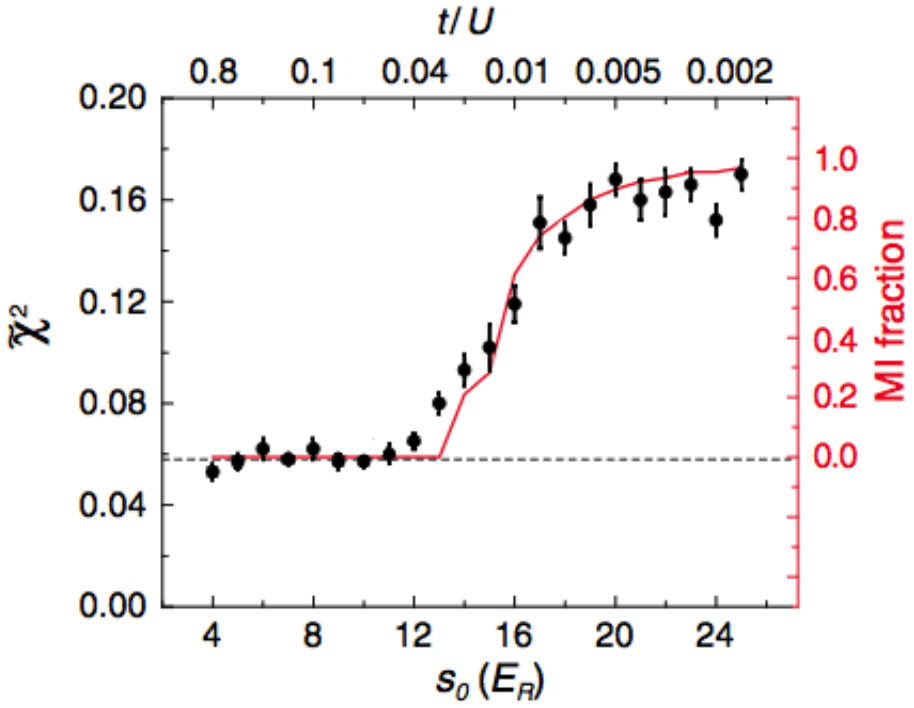

Figure 3.7: Excitation generated by quenching the lattice potential from different initial depths s_0. The data sample a range of s_0 such that at high s_0 nearly all the atoms start in the MI phase, whereas at low enough s_0 all the atoms are in the SF phase, as seen in the phase diagram in Fig. 3.2. The error bars are the standard error for the average taken over 5 images. The dashed line indicates the offset in $\tilde{\chi}^2$ that arises from the imaging noise. The red line is the fraction of atoms in the MI phase before the quench. The red vertical axis has been adjusted to overlap the two curves. The overall uncertainty in the MI fraction (which arises from uncertainty in t/U and N) ranges from 30% at $s_0 = 16$ $\mathrm{E_R}$ to 10% at $s_0 = 20$ $\mathrm{E_R}$. Below $s_0 = 12$ $\mathrm{E_R}$ and above $s_0 = 22$ $\mathrm{E_R}$, the uncertainty in the MI fraction is zero.

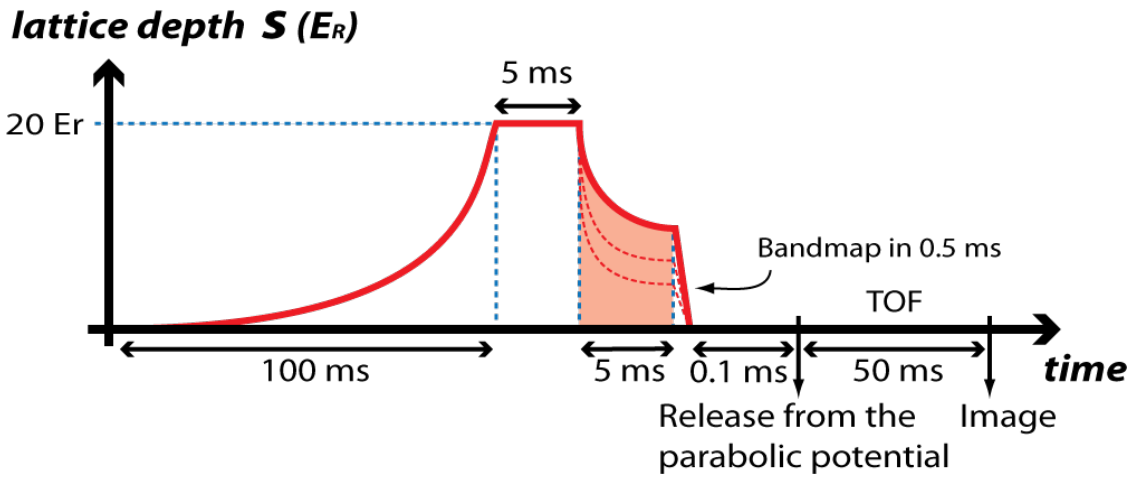

Figure 3.8: Experimental sequence for a linear quench in t/U (not to scale). The sequence is identical to that of Fig. 3.3 except for the quench procedure (shaded area) . The quench is performed using the ramp defined in Eq. 3.26 to ensure crossing the SF-MI phase boundary at a constant rate $d(t/U)/d\tau = 1/\tau_Q$. Most of the gas is in the MI phase before the quench, and the entire gas is in the SF phase after the quench.

3.4 Scaling Relations

In the Kibble-Zurek scenario, the quench rate controls the amount of excitations generated according to a power law that depends on the critical exponents for the phase transition. As a second experiment, we investigate this power law across 2 orders of magnitude in quench rate. The lattice potential depth is quenched maintaining the rate $d(t/U)/d\tau = 1/\tau_Q$ approximately constant, and we probe the quench rates $1/\tau_Q = (0.003-0.3)$ ms^{-1}. The quench is performed over 5 ms for all data and initiated from a gas composed nearly entirely of the MI phase at $s_0 = 20$ E$_\mathrm{R}$ ($t/U = 0.005$). The evolution of the lattice depth s as a function of time is given by the nonlinear form

$$s(\tau) = \frac{1}{4}\ln^2\left[\left(\frac{\pi a_s}{\sqrt{2}d}\right)\frac{\tau}{\tau_Q} + e^{-2\sqrt{s_0/\mathrm{E_R}}}\right]\ \mathrm{E_R} \tag{3.26}$$

derived from the analytical expressions for t and U in Eq. 3.11, where $d = \lambda/2$ is the lattice spacing. The lattice potential is quenched to a variable final lattice depth which depends on the quench rate. The final lattice depth ranges from $s \approx 2.2$ E$_\mathrm{R}$ for $1/\tau_Q = 0.3$ to $s \approx 13.6$ E$_\mathrm{R}$ for $1/\tau_Q = 0.003$ (the gas is always entirely in the SF phase after the quench). The full experimental sequence for $s(\tau)$ is shown in Fig. 3.8.

Besides measuring $\tilde{\chi}^2$ for this nonlinear quench—which may misinterpret topological excitations such as vortices—we also obtain the increase in energy induced by the quench by measuring the kinetic energy per

particle of the gas after TOF using the formula

$$K = \frac{m}{2\tau_{\mathrm{TOF}}^2}\langle r^2 \rangle, \tag{3.27}$$

where τ_{TOF} is the time of flight, $\langle r^2 \rangle$ is the second moment of the density distribution given by

$$\langle r^2 \rangle = \frac{3}{2} \cdot \frac{\sum_{ij} \mathcal{OD}_{ij} r_{ij}^2}{\sum_{ij} \mathcal{OD}_{ij}}, \tag{3.28}$$

and the factor of 3/2 arises from assuming an isotropic energy distribution among three spatial directions. K measures the total increase in energy induced by the quench, because the gas expansion converts the in-trap potential and interaction energy into kinetic energy.

A fit to the data shown in Fig. 3.9 reveals power laws for $\tilde{\chi}^2$ and K mutually consistent within the fit uncertainty, namely

$$\tilde{\chi}^2 \propto \left(\frac{1}{\tau_Q}\right)^{0.31\pm0.03} \tag{3.29}$$

and

$$K \propto \left(\frac{1}{\tau_Q}\right)^{0.32\pm0.02}. \tag{3.30}$$

However, our experimental results are inconsistent with the universal exponents predicted by the simplest version of the adiabatic-impulse-adiabatic approximation in the Kibble-Zurek mechanism. In an inhomogeneous gas, nearly all the atoms cross the "generic" phase transition and not the "multicritical" points at the tip of the MI lobes (see the phase diagram in Fig. 3.2). The generic points obey the dilute Bose gas universality class with critical exponents $\nu = 1/2$ and $z = 2$, whereas the multicritical points are governed by the universality class of the $O(2)$ quantum rotor with critical exponents $z = 1$ and $\nu = 1$ [163, 169, 176, 177]. Given that most of the atoms cross the generic points at the phase boundary, the number of excitations predicted by the KZM (Eq. 3.8) is $n_{\mathrm{ex}} \sim (1/\tau_Q)^{3/4}$, which is inconsistent with our data.

When we published our results in Ref. [1], we suggested that the disagreement between our experimental exponents and the theoretical predictions might be explained by numerous details that deserved more theoretical attention. For example, the spatially inhomogeneous nature of the gas gives rise to a phase transition "front" that moves through the gas. This has been examined in the context of certain classical and quantum phase transitions [30, 178, 179]. In a recent numerical study, it has been shown that the quenched gas does not have enough time to develop long range correlation, and therefore, the correlation length does not have a well defined power law [157]. Discrepancies may also arise from temperature effects, since the data in this work were taken at a low but nonzero temperature (the initial condensate fraction is higher than 90%

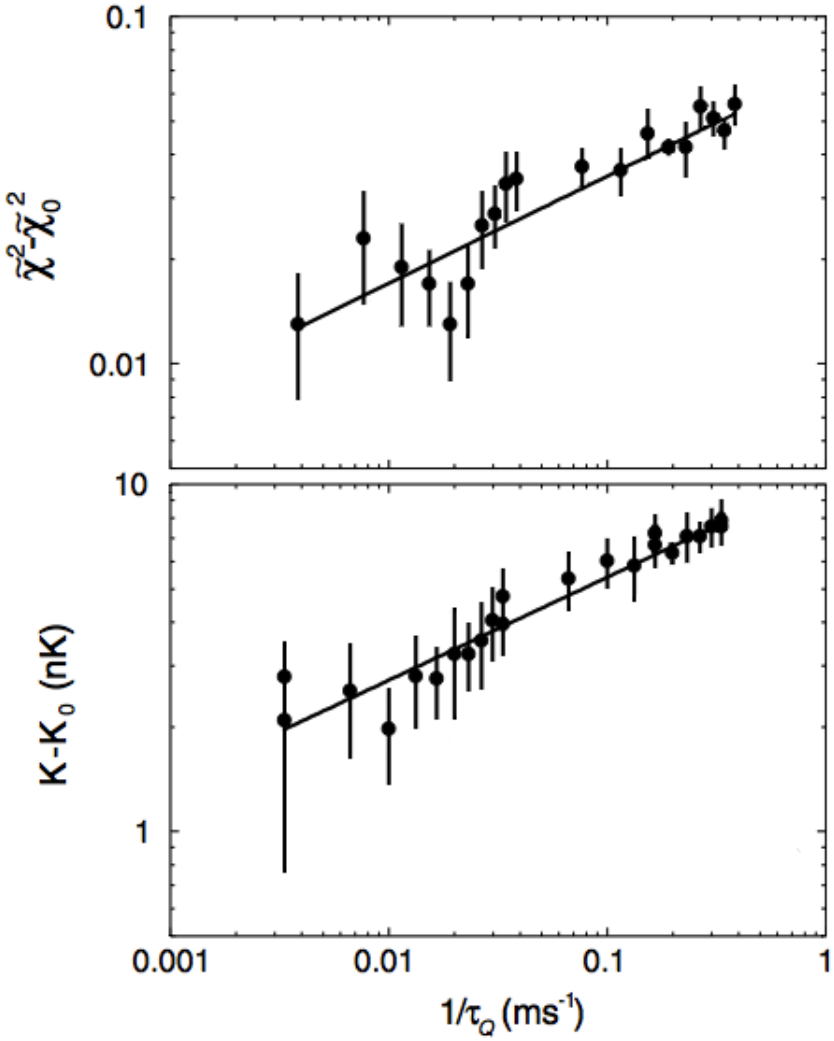

Figure 3.9: Scaling for the excitation level and the kinetic energy versus the quench rate $1/\tau_Q$. The measured offset $\tilde{\chi}_0^2$ is subtracted from $\tilde{\chi}^2$. Analogously, the kinetic energy without the quench K_0 (determined by averaging across images with $s_0 < 13$ $\mathrm{E_R}$) is subtracted from K. For comparison, the critical temperature for condensation in the trap before turning on the lattice and after bandmapping is approximately 100 nK. The error bars are the standard deviation for the average taken over 5 images.

before turning on the lattice) [150, 180]; from the finite size of the gas, as discussed in Ref. [151] for the Bose-Hubbard model in 1D; and from difference in the quench dynamics depending on the nature of the excitations (for example, $n_{\rm ex}$ scales differently if the excitations are only vortices). Finally, our measure $\tilde{\chi}^2$ (defined in Eq. 3.12) is only an estimate of the excitations, and thus, a more sophisticated formulation must be developed.

3.4.1 Quench in the Non-Universal Regime

After we published our results, Zurek et. al. numerically simulated our experiment by calculating the MI-to-SF quench dynamics for a zero-temperature, 3D gas using the Truncated Wigner Approximation [157] (the TWA approximates the full quantum dynamics of the original Hamiltonian by the evolution of ensemble averages [181–185]). It was found that the energy of the gas scales with the quench rate as a power law with exponent $\approx 1/3$, which is consistent with our experimental measurements. In this subsection, we present a brief outline of the numerical and analytical calculations presented in Ref. [157] (also see Ref. [185]).

The Bose-Hubbard Hamiltonian (Eq. 1.12) in 1D under the TWA[4] reduces to the classical Hamiltonian (besides an energy offset) [157, 186]

$$H = -t\sum_j(\psi^*_{j+1}\psi_j + \psi_{j+1}\psi^*_j) + \frac{\mathbb{n}U}{2}\sum_j|\psi_j|^4 + \sum_j\left(\frac{1}{2}m\omega^2d^2j^2 - \mu\right)|\psi_j|^2, \tag{3.31}$$

where ψ_j is a complex lattice field defined as $\sqrt{\mathbb{n}}\,\psi_j = \langle\hat{a}_j\rangle$, $\langle\hat{a}_j\rangle$ is the ensemble-averaged annihilation operator, $\mathbb{n}$ is the lattice filling, j indexes the lattice sites, d is the lattice spacing and ω is the frequency of the parabolic confinement. The discrete Gross-Pitaevskii Equation follows from $i\partial\psi_j/\partial\tau = \delta H/\delta\psi^*_j$ and reads

$$i\hbar\frac{\partial\psi_j}{\partial\tau} = -t(\psi_{j+1} + \psi_{j-1} - 2\psi_j) + \mathbb{n}U|\psi_j|^2\psi_j + \left(\frac{1}{2}m\omega^2d^2j^2 - \mu\right)\psi_j. \tag{3.32}$$

Ref. [157] simulates Eq. 3.32 numerically in 3D considering a linear quench in the tunneling energy t, which is ramped up from zero according to

$$\epsilon(\tau) = \frac{t(\tau)}{\mathbb{n}U} = \frac{\tau}{\tau_Q}. \tag{3.33}$$

In this MI-to-SF quench, the phase boundary is crossed at the rate $1/\tau_Q$ and the critical point is at approximately $\epsilon = 0$ for a large filling ($\mathbb{n} \gg 1$), since $\mathbb{z}\,(t/U)_c \approx 1/\mathbb{n}$ [71, 163, 169] ($\mathbb{z}$ is the lattice coordination number) and therefore $\epsilon_c = (t/\mathbb{n}U)_c \sim 1/\mathbb{n}^2 \approx 0$. The simulation shows that the gas energy scales with the

[4] This approximation is valid when $\mathbb{n} \gg 1$. For a discussion on the validity of the TWA in boson lattice models, see Ref. [186].

quench rate as

$$E = \langle H \rangle \sim \left(\frac{1}{\tau_Q}\right)^{0.31\pm0.01} \tag{3.34}$$

across four orders of magnitude in quench time (from $\tau_Q \simeq 10$ ms to $\tau_Q \simeq 10^5$ ms). The expectation values are estimated by averaging over stochastic realizations of $\psi_j(0) = e^{i\theta_j(0)}$ with random initial phases $\theta_j(0)$. The exponent in Eq. 3.34 coincides with the experimental value 0.32 ± 0.02 (Eq. 3.30) within the uncertainties, even though the experiment only marginally satisfies the condition $\mathbb{n} \gg 1$ for validity of the TWA.

An analytical calculation based on the KZM in a non-universal regime also agrees with the experimental exponent 1/3. In a MI-to-SF quench, the KZM arises from an impulse-adiabatic approximation, where the initial state is a frozen MI phase with negligible tunneling between neighbor sites and the system evolves into an adiabatic regime as the tunneling energy increases. The KZM postulates that the dynamics in the system becomes adiabatic when

$$\frac{1}{\epsilon(\tau)}\frac{d\epsilon(\tau)}{d\tau} \sim \frac{1}{\tau_0(\tau)}, \tag{3.35}$$

where the left side is determined directly from the ramp equation defined in Eq. 3.33. The relaxation time $\tau_0(\tau)$, on the other hand, scales with t as

$$\tau_0 \sim t^{-1/2} \tag{3.36}$$

in the so-called Josephson regime, where the impulse-adiabatic crossover occurs in the deep MI phase ($t/U \ll 1$), and therefore, Eq. 3.32 can be approximated by the Josephson equation[5]

$$\frac{\partial^2\theta_j}{\partial\tau^2} = \frac{2\mathbb{n}tU}{\hbar^2}\Big[\sin(\theta_{j+1}-\theta_j) + \sin(\theta_{j-1}-\theta_j)\Big]. \tag{3.37}$$

The scaling relation expressed in Eq. 3.36 follows from a dimensional analysis on Eq. 3.37 and it has been numerically verified in Ref. [157]. Disagreement with the universal scaling $\tau_0 \sim t^{-\nu z} = t^{-1}$ suggests that the regime probed is non-universal. A similar non-universal behavior has been observed in 1D via density-matrix renormalization group [187]. The impulse-adiabatic crossover condition (Eq. 3.35) then reduces to

$$\frac{1}{\tau^*} \sim \sqrt{\frac{\tau^*}{\tau_Q}}, \tag{3.38}$$

and, consequently, $\tau^* \sim \tau_Q^{1/3}$ and $t^* \sim \tau_Q^{-2/3}$. Ref. [157] shows that the time-dependent temperature in the

[5] In the Josephson regime, dynamics consists of small density fluctuations $\delta\mathbb{n}_j = \mathbb{n}\delta f_j$ on top of a uniform background $\mathbb{n}$. Therefore, ψ_j is approximated as $\psi_j = \sqrt{1+\delta f_j}\, e^{i\theta_j}$, with δf_j and θ_j real variables and $|\delta f_j| \ll 1$. Substitution of ψ_j into the Hamiltonian in Eq. 3.31 leads to the equations of motion for $\delta\mathbb{n}_j$ and θ_j which becomes the Josephson equation after elimination of $\delta\mathbb{n}_j$.

adiabatic stage scales as $T \sim t^{1/2}(t^*)^{1/2}$ and, combined with $E \sim T$ from the equipartition theorem, we find that the energy of the system scales as

$$E \sim t^{1/2}\tau_Q^{1/3}. \tag{3.39}$$

Consistency between the experiment and the non-universal Kibble-Zurek prediction strongly suggests that the quench rates in our experiments—which are in the range $\tau_Q \approx (1 - 300)$ ms—are too fast to probe the universal regime [30]. Implementing slow quenches to test quantum criticality is experimentally challenging because quantum coherence and atom number stability are required for long quench times. Furthermore, the universal regime may not even be experimentally accessible. For example, simulations in 1D show that the universal scaling regime is reached at the "astronomical" quench time of $\tau_Q \simeq 10^{10}\,\tau_0$ [158].

The presence of phase domains and vortex excitations after the quench is confirmed via computational simulations [157]. In the KZM picture, the initial MI state with random phases remains unchanged during the impulse stage and, once the evolution becomes adiabatic, phase correlation starts growing across the system. Given that long range order can not be reached in a finite quench time, the lattice-potential quench leads to a state comprised of phase domains and topological vortex excitations. In the simulation, the correlation length does not have a simple power law with the quench time, and therefore, we were unable to compare the numerical excitation density $n_{\rm ex}$ with the experimental data.

3.5 Conclusions

The methodology we have demonstrated in this chapter provides a window into excited states and dynamics which are beyond our current theoretical understanding in a wide variety of strongly interacting many-body quantum systems.

We have found that the amount of excitations after a MI-to-SF quench is proportional to the fraction of atoms crossing the phase boundary. This result strongly supports the Kibble-Zurek picture, where the diverging relaxation time near the phase boundary "freezes in" phase fluctuations present in the MI, and dynamics only effectively restart some time after crossing the phase boundary. Once the dynamics becomes adiabatic, the phase fluctuations develop into superfluid excitations which potentially include sound waves and topological excitations such as vortices. While it was suggested in Ref. [188] that the condensate fraction may oscillate after the quench, we find no evidence for such behavior.

The measured power-law relation for the gas energy versus the quench rate is consistent with numerical simulations of the Bose-Hubbard Model using the TWA in the Josephson regime. Furthermore, the KZM correctly predicts the observed scaling based on non-universal power laws. In contrast, the scaling

relation for the excitation density $n_{\rm ex}$ in the experiment does not coincide neither with the simple adiabatic-impulse-adiabatic universal Kibble-Zurek prediction nor with the numerical simulation. Potential sources of disagreement are the presence of topological defects, thermal and finite size effects, and the spatially inhomogeneity of the gas.

In order to investigate different aspects of a quantum phase transition, new tools and techniques have to be developed. For example, there are several proposals for measuring critical exponents in ultracold gas experiments [28, 176, 177, 189]. Moreover, a quantum gas microscope with single lattice-site resolution [168, 190–197] could potentially measure the local gas configuration during a phase-transition quench.

A particularly important application of quantum criticality and quench dynamics is adiabatic quantum computing [31], where a system is prepared in a simple quantum state of an initial Hamiltonian and adiabatically driven to a final Hamiltonian (usually across a phase transition) whose ground state is the solution to a non-trivial computational problem. Quantum dynamics may also have significant consequences for thermometry in optical lattice experiments [198]. One commonly employed technique to estimate temperature in a lattice is to slowly turn off the lattice potential, measure temperature, and then infer entropy in the lattice assuming that the turn-off is adiabatic. We have found that adiabaticity is violated across a wide range of linear lattice quench rates. For example, for a quench from $s_0 = 20$ $\mathrm{E_R}$, the amount of excitation decreases from $\tilde{\chi}^2 = 0.17$ to only $\tilde{\chi}^2 = 0.12$ when the ramp time is increased fivefold from 5 ms to 25 ms.

Chapter 4

Bath-Induced Band Decay

4.1 Introduction

Dissipation plays an essential role in determining the behavior of many quantum systems [199, 200]. In the form of decoherence, dissipation is deleterious and an obstacle to activities that involve controlling quantum states, such as quantum information processing [201]. Conversely, the effects of dissipation can be advantageous. For example, new paradigms have emerged for engineering dissipation to give rise to desired quantum states [202–211] and even as a resource for universal quantum computing [212]. Furthermore, dissipation could potentially be used to cool many-particle systems into manifestly quantum regimes via coupling to a reservoir, as exemplified in Fig. 4.1. Intense research into manipulating dissipation is ongoing, inspired both by these applications and by the many open questions regarding the dynamics of dissipation, especially in strongly interacting systems [213, 214].

Ultracold gases are remarkably dissipation-free, closed quantum systems and, thus, an ideal platform for harnessing and studying engineered dissipation. In this chapter, we investigate dissipation on a strongly correlated atomic gas confined in an optical lattice due to interaction with a thermal bath. Using a three-dimensional spin-dependent lattice, we engineer a low-entropy, dissipative bath that interacts with a band-excited strongly correlated thermal lattice gas prepared in the Mott-insulator regime of the Bose-Hubbard model (Eq. 1.12). Previous experiments probing dissipation and entropy exchange in species-dependent potentials have utilized one-dimensional lattices and explored the weakly interacting regime [215, 216].

The bath in our measurements affects the lattice gas similarly to the way in which the electromagnetic vacuum causes decay of excited electronic states in an atom via spontaneous emission [206, 217–219]. Fluctuations of the electric field of the electromagnetic vacuum couple electronic states through the electric dipole interaction, while in our system, collisions with the bath couple lattice atoms to different bands. Because the electromagnetic vacuum is a zero-entropy state, the dipole interaction only causes decay to lower energy states. Likewise, since the bath in our experiment is a weakly interacting superfluid and thus a low-entropy reservoir, lattice atoms exclusively decay to lower energy bands. Irreversible decay of electronic states only

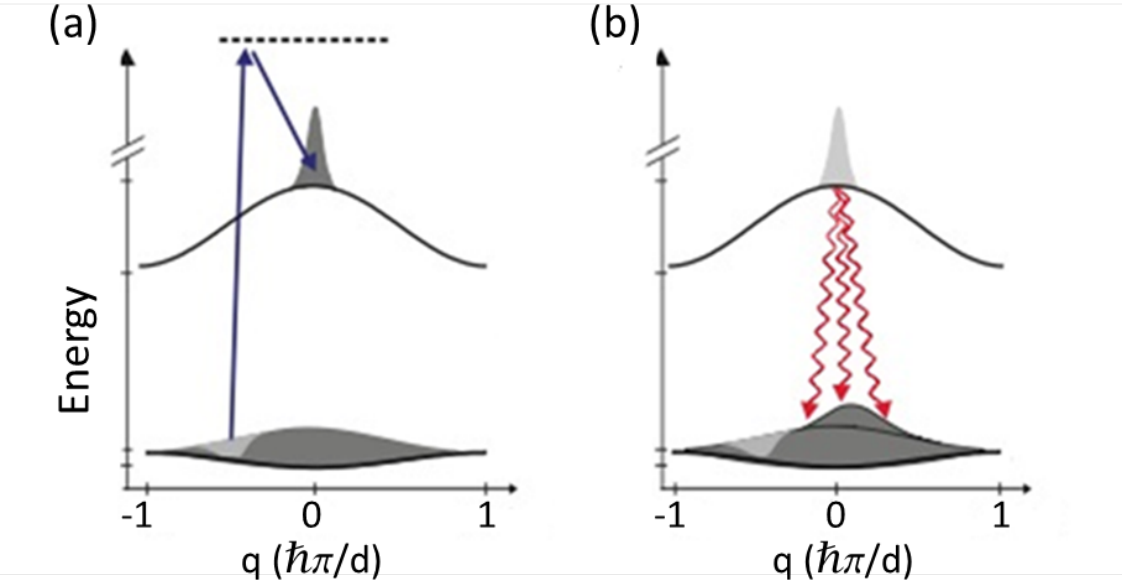

Figure 4.1: Scheme proposed in Refs. [58,59] for cooling an atomic gas confined in an optical lattice through dissipation. (a) Stimulated Bragg excitation is engineered to selectively transfer atoms from states in the ground Bloch band with large quasimomentum q to states with small quasimomentum in the first-excited band. (b) The excited atoms decay to the ground band through collisions with a background gas which acts as a thermal reservoir. By performing the cooling cycle iteratively, the quasimomentum distribution of the lattice-bound gas becomes narrower about the origin.

happens when the spontaneously emitted photon escapes and does not interact with the atom; otherwise, coherent vacuum Rabi oscillations occur [220]. We achieve irreversible decay in our system by tuning the trap depth so that the bath atoms involved in inter-band transitions can escape from the gas.

4.2 Experimental Procedure

To carry out the experiment, we start with a partially condensed ^{87}Rb gas in the $|F = 1, m_F = -1\rangle$ hyperfine state confined in a crossed dipole trap (described in Section 1.1.1). Subsequently, an unequal mixture of $|1, -1\rangle$ (lattice) and $|1, 0\rangle$ (bath) states is prepared using an adiabatic rapid passage driven by a radio-frequency magnetic field[1]. This mixture is miscible in the dipole trap and stabilized against spin-exchange collisions by a 10 G uniform magnetic field. The atom number in each state is $N^{(l)} = (13 \pm 2) \times 10^3$ for the lattice atoms and $N^{(b)} = (36 \pm 5) \times 10^3$ for the bath atoms, and the temperature of the spin mixture is (91 ± 6) nK. At this temperature, the lattice atoms are above the critical temperature for Bose condensation, while the bath atoms are below the critical temperature with $(30 - 40)\%$ condensate fraction. The geometric mean of the dipole trap frequencies is $2\pi \times (75 \pm 6)$ Hz, and the trap depth is $(420 \pm 60)\, k_B \times$ nK.

[1]The RF field is adiabatically swept across resonance to drive a Landau-Zener transition.

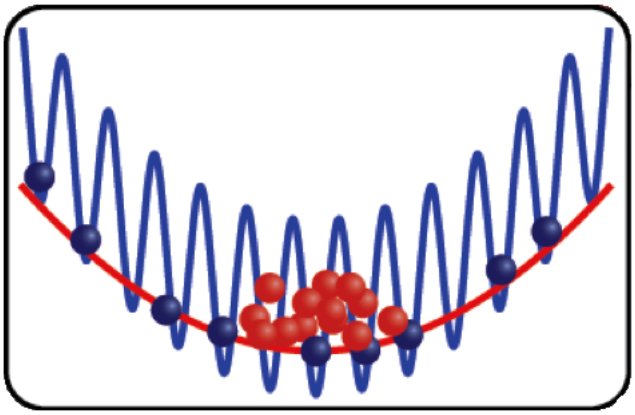

Figure 4.2: Lattice atoms (blue spheres) and bath atoms (red spheres) in a spin-dependent lattice generated from 790 nm laser beams. Both species are harmonically confined in a crossed dipole trap formed from 1064 nm laser beams, but only the lattice atoms experience the periodic potential.

4.2.1 Lattice-Bath Atom Mixture

A spin-dependent, cubic optical lattice formed from three pairs of counter-propagating laser beams with $\lambda = 790$ nm[2] is slowly superimposed on the gas over 50 ms. Both species in the mixture experience identical confinement from the dipole trap, but only the lattice atoms interact with the optical lattice, since the potential is proportional to $|m_F|$, as expressed by Eq. 1.9 in the $\theta = 90°$ configuration. An illustration of the spin mixture in the optical lattice is shown in Fig. 4.2. The lattice atoms realize the strongly interacting Bose-Hubbard model with tunneling energy t and interaction energy U controlled by the lattice potential depth s [221], and the $|1,0\rangle$ atoms form a spatially overlapping, weakly interacting superfluid bath [222]. Similar 1D spin-dependent lattices have also been used to investigate atomic impurity [223,224], matter-wave probes [225], and mixed-dimensional scattering [226]. Spin mixtures in 3D spin-dependent lattices have been used to explore applications to thermometry [77,222] and to study superfluid coherence [227].

We set the lattice depth along the lattice directions $\hat{x}$ and $\hat{y}$ to 22.5 E_R, and along the third direction $\hat{z}$ to $s = (13.5 - 18)$ E_R[3]. The spatial configuration of the lattice vectors $\hat{x}$, $\hat{y}$, and $\hat{z}$ are shown in Fig. 1.2. At zero temperature, the lattice atoms would be in the Mott-insulator phase for the lattice potential depths explored in this experiment. The bandgap between the ground and first-excited bands E_{bg} for the lattice atoms along the z direction is in the range $(1100 - 1300)\, k_B \times$ nK, which is greater than the dipole trap depth for the bath atoms. The corresponding bandgap along the x and y directions is $1500\, k_B \times$nK. The bandgap difference in $\hat{z}$ and $\hat{x}, \hat{y}$ is greater than the excited bandwidths and prevents interparticle collisions between lattice atoms in excited bands from transferring energy between lattice directions.

[2]We chose $\lambda = 790$ nm for the spin-dependent lattice because it nearly minimizes the heating rate from spontaneous scattering. See Ref. [77].

[3]The lattice depths were chosen to sample the MI phase of the lattice gas with the available laser power at $\lambda = 790$ nm.

For all the lattice depths sampled in this work, we estimate that the temperature of the lattice atoms ranges from 50 to 130 times the Hubbard tunneling energy t of the ground band, and therefore, atoms fill the ground band almost uniformly. Moreover, the temperature is 0.07 times the bandgap in the z direction, and consequently, all the atoms are approximately in the ground band according to the estimation for the excited-band population $1/(1+e^{-E_{\mathrm{bg}}/k_BT}) \approx 1$. The temperature of the lattice atoms is estimated using semiclassical thermodynamics (which neglects interactions) [85]. We assume that the lattice turn-on is isentropic, and we solve self-consistently for the chemical potential μ and temperature T that reproduce the number of lattice atoms N and entropy S before turning on the lattice. The entropy of the lattice gas is given by

$$S = \frac{E - \mu N - \Omega}{T}, \tag{4.1}$$

where the gas energy E, atom number N and grand canonical potential Ω are calculated using the semiclassical quasimomentum distribution

$$n(q_x, q_y, q_z) = \frac{1}{h^3} \int d^3r \frac{1}{e^{-\mu/k_BT} e^{2t\sum_{i=x,y,z}[1-\cos(q_i d/\hbar)]/k_BT} e^{m\omega^2 r^2/2k_BT} - 1} \tag{4.2}$$

(ω is the mean dipole trap frequency and $d = \lambda/2$ is the lattice spacing). Details regarding this semiclassical approach can be found in Appendix D.

4.2.2 Bragg Excitation

After turning the lattice on, we use a pair of Bragg laser beams 500 GHz detuned from the $5P_{3/2}$ excited electronic state to transfer a fraction of the lattice atoms from the ground band to the first-excited band along the lattice z-direction. The spatial configuration of the Bragg beams is illustrated in Fig. 1.2. The wavevector difference between the Bragg beams is $\Delta k = 1.43\,\pi/d$ and it is aligned along the z direction. The relative frequency is tuned to match the bandgap frequency E_{bg}/h, which ranges from 22 kHz at $s = 13.5$ $\mathrm{E_R}$ to 27 kHz at $s = 18$ $\mathrm{E_R}$. The Bragg light is pulsed on for 200 μs and the relative frequency is swept across resonance over 2 kHz. According to the Rabi formula 2.14 for stimulated Bragg transitions, we estimate that the excitation probability along $\hat{z}$ varies from 0.45 to 0.65 across the band, and excitation in the transverse directions is negligible because of the lattice depth mismatch. We estimate, using Eq. 1.3, that spontaneous scattering caused by the Bragg beams occurs at a rate lower than 1 $\mathrm{s^{-1}}$. The experimental sequence is depicted in Fig. 4.3.

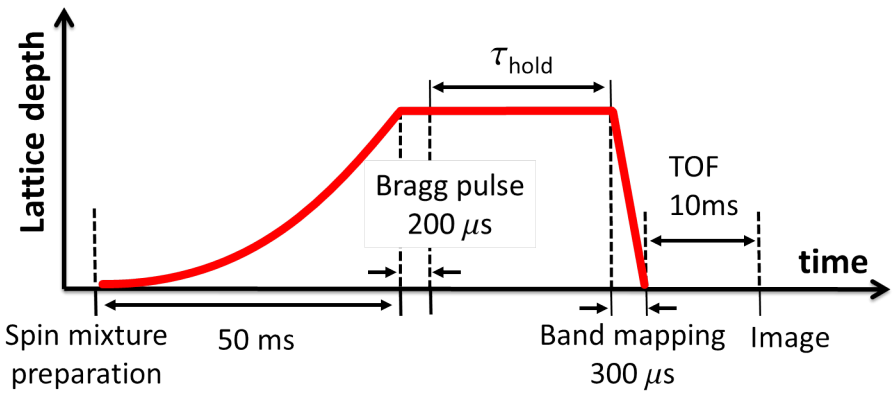

Figure 4.3: Timeline of the experimental sequence for measuring band decay (not to scale). The lattice potential is slowly turned on in 50 ms using an exponential ramp. A fraction of the lattice atoms are transferred to the first-excited band by a 200 μs Bragg pulse. The hold time τ_{hold} in our experiments ranges from 0 to 100 ms. Bandmapping is performed with a linear ramp in 300 μs and absorption images are taken after 10 ms of TOF.

4.3 Band Decay Mechanisms

Once the lattice atoms are band-excited, the gas is held in the lattice for τ_{hold} while it decays back to the ground band. The band decay is dominated by two decay channels: collisions between lattice atoms (intrinsic decay) and collisions between lattice and bath atoms (bath-induced decay). Both cases are illustrated in (a) and (b) of Fig. 4.4, respectively.

4.3.1 Intrinsic Decay

In this mechanism, two lattice atoms in the first-excited band ($n = 1$) mutually collide. One atom decays to the ground band ($n = 0$), while the other atom is promoted to the second-excited band ($n = 2$). Intrinsic decay has previously been investigated in species-independent optical lattices in 1D [228] and in very deep 3D potentials [92].

In a non-interacting system, the intrinsic decay channel is suppressed at the relatively high lattice depth we employ because of energy and momentum conservation in a binary intra-band collision, namely

$$\begin{aligned} \epsilon^{(1)}(q_{1z}) + \epsilon^{(1)}(q_{2z}) &= \epsilon^{(0)}(q'_{1z}) + \epsilon^{(2)}(q'_{2z}) \\ q_{1z} + q_{2z} &= q'_{1z} + q'_{2z}, \end{aligned} \tag{4.3}$$

where (q_{1z}, q_{2z}) are the initial quasimomenta with $n = 1$ and (q'_{1z}, q'_{2z}) are the final quasimomenta with $n = 0$ and $n = 2$. Suppression of intrinsic collisions as the lattice depth increases can be understood more easily in the limit of a very deep lattice. In this regime, the energy bands become approximately flat, and

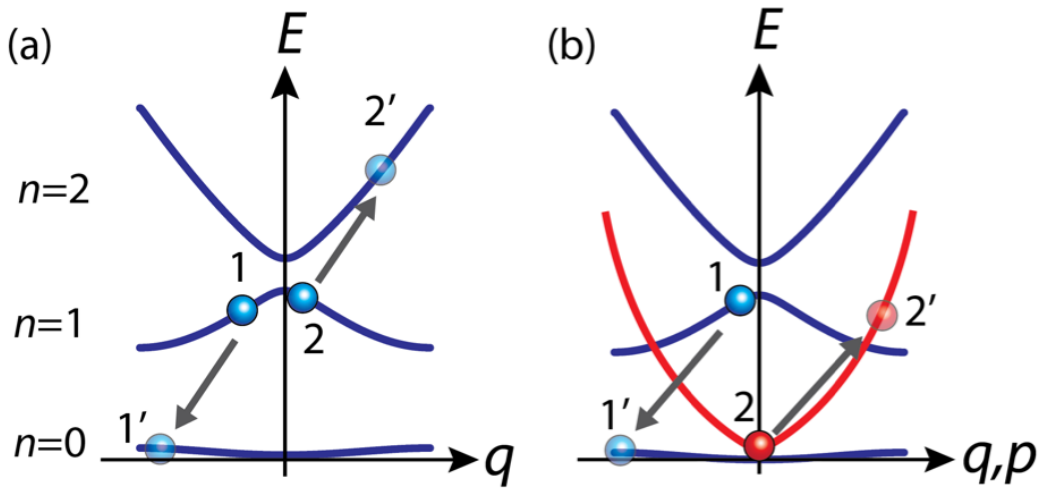

Figure 4.4: Illustration of possible band decay processes in the z direction of the lattice. (a) Intrinsic decay arises from collisions between lattice atoms (blue spheres). The band energies as a function of quasimomentum q are shown using blue lines. Atoms begin in the initial states 1 and 2 and scatter to the states $1'$ and $2'$ through a collision. (b) The bath-induced decay process arises as a result of inter-species collisions. The Bogoliubov dispersion (red line) as a function of momentum p for the bath atoms (red spheres) is superimposed on the band structure. The bath atoms scatter into particle-like Bogoliubov excitations that can escape from the trap.

therefore, two lattice atoms within the same band can not mutually collide because of mismatching bandgaps (the lattice potential is inherently anharmonic, as shown in (b) of Fig. 1.4).

4.3.2 Bath-Induced Decay

In this decay channel, the bath-induced decay can be understood as a lattice atom in the first-excited band colliding with a Bogoliubov quasiparticle initially at low energy and momentum in the superfluid bath. After the collision, the quasiparticle is scattered to higher energy and momentum, and the lattice atom decays to the ground band. Based on energy conservation, the energy of the excited quasiparticle will approximately be equal to E_{bg} (within the bandwidth), which is larger than the dipole trap depth for the bath atoms. Furthermore, for our range of experimental parameters, a quasiparticle with energy equal to E_{bg} has a momentum more than 6 times greater than $\sqrt{2m\mu}$, where $\mu \approx 20\,k_B\times$nK is the chemical potential of the bath. Therefore, the excited quasiparticle is particle-like, and the bath-induced decay process can result in a bath atom leaving the trap.

We have experimentally shown in a previous work, reported in Ref. [222], that thermalization between ground-band atoms and the bath is suppressed for deep enough lattices, because energy and momentum

conservation can not be satisfied in such inter-species collision. This result has important consequences in the cooling scheme proposed in Fig. 4.1, since the cooled atoms in the ground-band must remain thermally insulated from the bath.

The lattice depth threshold at which inter-species thermalization becomes suppressed can be estimated from energy and momentum conservation, specifically

$$\epsilon(\mathbf{q}+\mathbf{p}/2) = \varepsilon(\mathbf{p}) + \epsilon(\mathbf{q}-\mathbf{p}/2), \tag{4.4}$$

where $\epsilon(\mathbf{q})$ is the excitation energy of a lattice atom with quasimomentum $\mathbf{q} = (q_x, q_y, q_z)$, $\varepsilon(\mathbf{p})$ is the excitation energy of a quasiparticle in the bath with momentum $\mathbf{p} = (p_x, p_y, p_z)$, and we have approximated the initial momentum of the bath to zero. For $\epsilon(\mathbf{q})$, we consider the tight-binding energy of a non-interacting gas

$$\epsilon(\mathbf{q}) = \sum_{i=x,y,z} 2t_i \left[1 - \cos\left(\frac{q_i d}{\hbar}\right)\right], \tag{4.5}$$

and for $\varepsilon(\mathbf{p})$ we use the Bogoliubov excitation spectrum of a weakly interacting uniform Bose gas [71]

$$\varepsilon(\mathbf{p}) = \sqrt{\varepsilon^0(p)[\varepsilon^0(p) + 2gn]} \approx p\sqrt{\frac{g\,n}{m}}, \tag{4.6}$$

where $\varepsilon^0(p) = p^2/2m$ is the free-particle energy, $g = 4\pi\hbar^2 a_s/m$ is the interaction parameter, and n is the gas density. The bath energy has been approximated to a linear function of p, since collisions with lattice atoms in the ground band can only excite low energy modes in the bath. Substitution of Eqs. 4.5 and 4.6 into Eq. 4.4 leads to

$$p\sqrt{\frac{g\,n}{m}} = \sum_{i=x,y,z} 4t_i \sin\left(\frac{q_i d}{\hbar}\right) \sin\left(\frac{p_i d}{2\hbar}\right). \tag{4.7}$$

For each pair of vectors $\mathbf{q}$ and $\mathbf{p}$, there is a tunneling energy threshold t_c below which Eq. 4.7 can not be satisfied and, consequently, collisions between the ground-band atoms and the bath are suppressed. Eq. 4.7, however, does not apply to lattice atoms in higher-energy bands, and therefore, bath-induced band decay can occur.

We can estimate t_c by finding an upper bound[4] of the right side of Eq. 4.7, namely

$$p\sqrt{\frac{g\,n}{m}} \leq 2\sqrt{3}\,t\,\frac{pd}{\hbar}, \tag{4.8}$$

[4]We use the inequalities $\sin(q_i d/\hbar) \leq 1$, $\sin(p_i d/2\hbar) \leq |p_i|d/2\hbar$ and $\sum_{i=x,y,z}|p_i| \leq \sqrt{3}p$.

and therefore,

$$t_c \simeq \sqrt{\frac{4}{3\pi^3}\left(\frac{a_s}{d}\right)\text{n}\, d^3}\ \mathrm{E_R}, \tag{4.9}$$

where $\text{n}\, d^3$ is the lattice filling (number of particles per lattice site). A more accurate estimation of t_c would require to solve Eq. 4.7 numerically for each pair of vectors $\mathbf{p}$ and $\mathbf{q}$ under a local-density approximation.

In most ultracold gas experiments, the lattice filling n is not uniform because of the overall parabolic confinement. Consequently, as the lattice depth increases, suppression of collisions start at the gas center, where n is highest, and progresses towards the edge, where n vanishes. Even though the outermost atoms in the lattice are always in thermal contact with the bath because $\text{n} \approx 0$, the bulk of the gas remains thermally insulated from the bath at high enough lattice depths.

In the experiments in this chapter, the central filling calculated using a site-decoupled mean-field approximation (Appendix F) is $\text{n}d^3 = 0.13$. The corresponding critical tunneling and lattice depth are $t_c \approx 0.016\ \mathrm{E_R}$ and $s_c \approx 11\ \mathrm{E_R}$, respectively.

4.4 Band Decay Measurement

The fraction of lattice atoms in each band is measured from quasimomentum distributions after holding the gas in the lattice for τ_{hold}. The quasimomentum distribution of the gas is acquired using bandmapping in 300 μs and an expansion time of 10 ms. The bath atoms are spatially separated from the lattice atoms during TOF using a magnetic field gradient. After bandmapping, atoms populating the ground band appear inside the first BZ and atoms in the first-excited band are mapped onto the second BZ. Fig. 1.5 shows the first and second BZ in 3D and their projection onto the imaging plane.

Fig. 4.5 shows typical images of the lattice atoms taken after Bragg excitation and after holding the lattice potential on for τ_{hold}. Two different situations are presented: Part (b) illustrates the band decay for the lattice atoms when the bath is absent and (c) shows the band decay when the bath is present. To characterize the decay process, we determine the fraction of lattice atoms in the ground band $N_g^{(l)}/N^{(l)}$ taken at different τ_{hold}, where $N_g^{(l)}$ is the number of lattice atoms in the ground band, and $N^{(l)}$ is the total number of lattice atom. We obtain $N_g^{(l)}$ and $N^{(l)}$ by integrating the optical depth of the absorption images over the first BZ and over the entire image, respectively. At $\tau_{\mathrm{hold}} = 0$, we measure that approximately 40% of the lattice atoms are in the first-excited band along $\hat{z}$, and off-resonant excitation through the first-excited band leads to 10% of the atoms driven to the second-excited band.

Two systematic issues potentially affect our determination of $N_g^{(l)}/N^{(l)}$. First, atoms excited along the x and y directions can appear to be within the first BZ, as observed in (b) of Fig. 1.5. Nevertheless, excitations

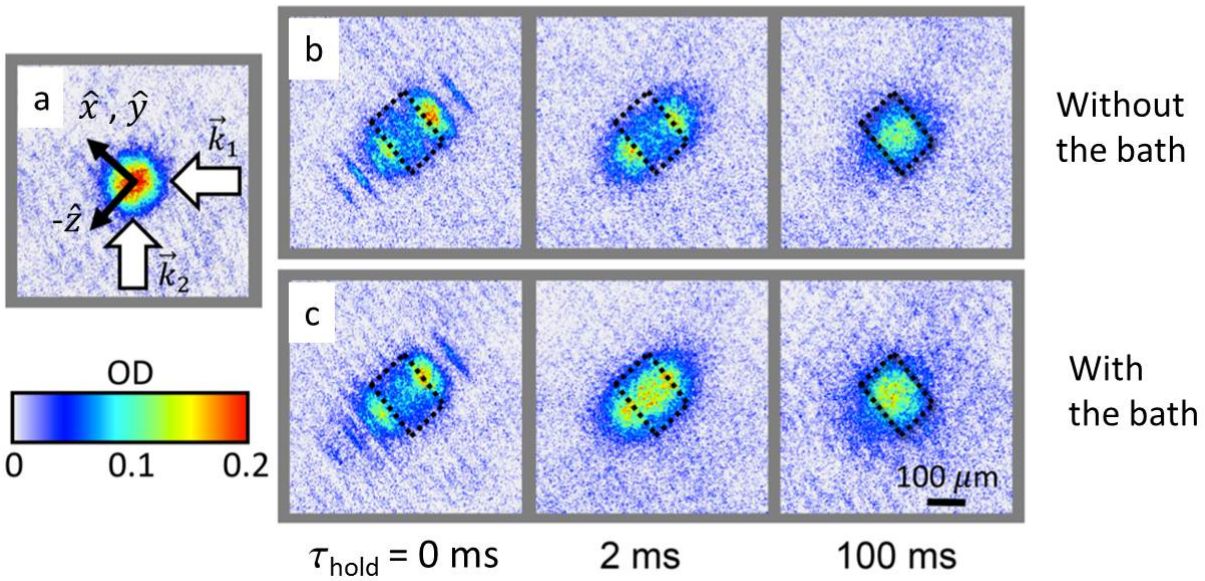

Figure 4.5: TOF images of the lattice atoms only (spatially separated from the bath) taken at $s = 16.2\ \mathrm{E_R}$. The images are projections of the 3D gas onto the imaging plane. (a) Lattice atoms before Bragg excitation. The geometry of the Bragg beams (white arrows) and lattice beams (black arrows) has been superimposed on the image. The Bragg beams propagate along $\mathbf{k}_1$ and $\mathbf{k}_2$, so that their wavevector difference lies along the z direction. As discussed in the text, the lattice atoms uniformly fill the ground band. (b) Lattice atoms after holding the lattice on for τ_{hold} without the bath present. (c) Lattice atoms after holding the lattice on for τ_{hold} when the bath is present. The first BZ projected onto the imaging plane is displayed using dashed lines.

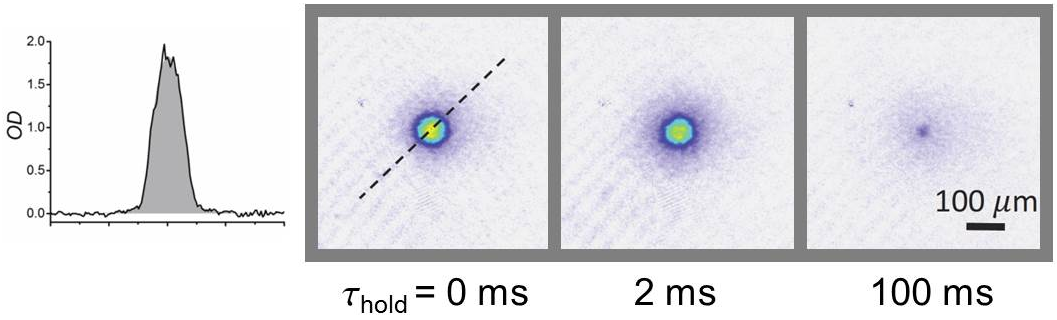

Figure 4.6: TOF images of the bath associated with the images in part (c) of Fig. 4.5. The lattice and bath atoms interact for τ_{hold} after Bragg excitation, and they are spatially separated for imaging. A slice along the dashed line displays the result of a two-component fit (shaded grey).

along these directions are highly suppressed because the Bragg wavevector lies along $\hat{z}$. Furthermore, we have employed larger lattice depths along $\hat{x}$ and $\hat{y}$ to prevent exchange of excitation energy between lattice directions. Second, a systematic error is introduced to measuring $N_g^{(l)}/N^{(l)}$ using our imaging method because bandmapping fails at the band edge, and thus, a fraction of atoms within the ground band appear outside the first BZ. For example, before Bragg excitation we measure $N_g^{(l)}/N^{(l)} = 0.77 \pm 0.06$ even though the gas temperature is sufficiently low compared with E_{bg} such that almost all the atoms are in the ground band. This error does not significantly affect the measured decay rate, since the ground band is homogeneously filled and the excitation is nearly uniform across the BZ.

In both situations, with and without the bath present, the decay channels involve binary collisions, and therefore, the excited lattice atoms decay exponentially to the ground band, as shown in (a) of Fig. 4.7 for the fraction of atoms in the ground band $N_g^{(l)}/N^{(l)}$ versus τ_{hold}. We extract a decay time constant τ (and a decay rate $\Gamma = 1/\tau$) by fitting a single exponential decay to $N_g^{(l)}/N^{(l)}$, as shown by the solid and dashed lines in Fig. 4.7.

If we consider Γ_{ll} as the rate of binary collisions between excited lattice atoms (lattice-lattice), then $1/\Gamma_{\mathrm{ll}}$ gives the decay time constant in absence of the bath. On the other hand, if we consider Γ_{lb} as the rate of binary collisions between the bath and excited lattice atoms (lattice-bath), then the total rate of change in $N_g^{(l)}$ is given by

$$\frac{dN_g^{(l)}}{d\tau} = \Gamma_{\mathrm{ll}} + \Gamma_{\mathrm{lb}}, \tag{4.10}$$

and therefore $1/(\Gamma_{\mathrm{ll}} + \Gamma_{\mathrm{lb}})$ is the decay time constant of the excited atoms when the bath is present. The enhancement in the decay rate observed in (a) of Fig. 4.7 when the bath is present confirms the existence of additional decay mechanisms in the system.

Even though the bath marginally increases the ground-band fraction $N_g^{(l)}/N^{(l)}$ once the decay is complete, $N_g^{(l)}/N^{(l)}$ is greatly reduced compared with the state before Bragg excitation. For example, for the lattice depth $s = 16.2\ \mathrm{E_R}$ shown in (a) of Fig. 4.7, the ground-band fraction increases from 0.496 ± 0.006 to 0.516 ± 0.007 according to the exponential fits, but the final ground-band fraction is considerably lower than the initial fraction 0.77 ± 0.06. Heating in the lattice gas occurs because a small fraction of intrinsic decay events can deposit a large amount of energy into the gas, since E_{bg} is much larger than the bandwidth of the ground band. For instance, at $s = 16\ \mathrm{E_R}$, $E_{\mathrm{bg}} \approx 1\ \mu\mathrm{K} \times k_B$, whereas the ground-band bandwidth is just a few $\mathrm{nK} \times k_B$

We also analyze images of the bath atoms (for example, see Fig. 4.6) using a bimodal fit to measure the condensed and non-condensed components of the gas. From the fit, we obtain the condensate fraction $N_0^{(b)}/N^{(b)}$ of the bath and the atom number $N^{(b)}$, as shown in (b) and (c) of Fig. 4.7. For all s, the condensate

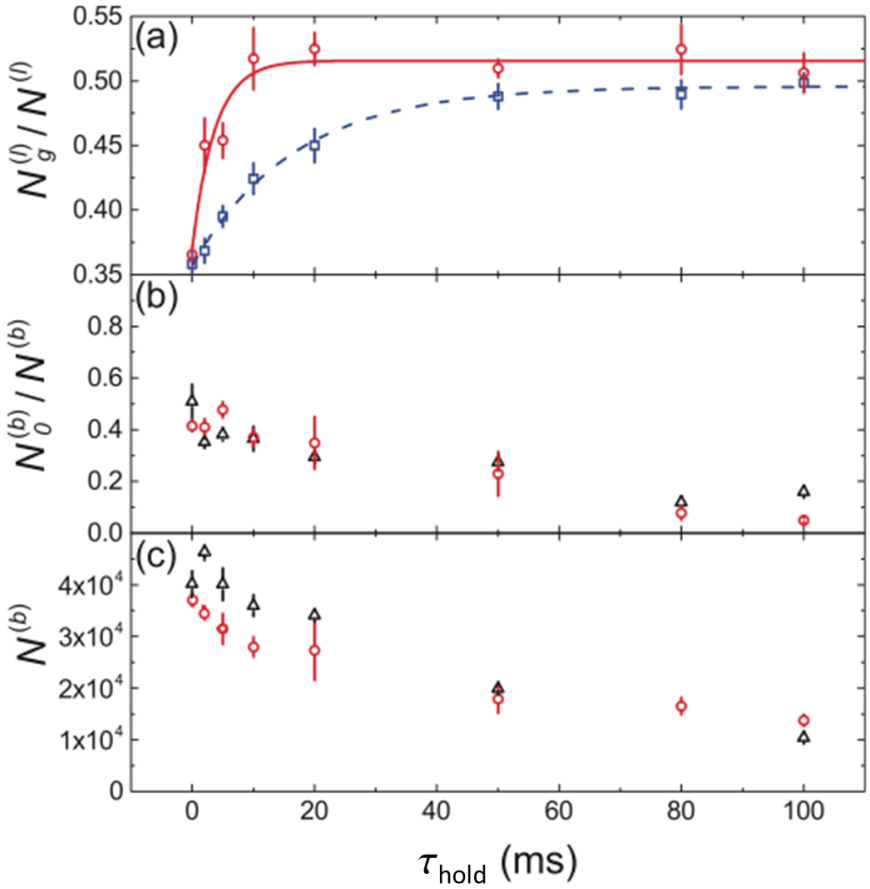

Figure 4.7: Observables for the lattice and bath atoms during the band decay process in a 16.2 E_R lattice. The error bars show the standard error of the mean of 4 to 6 experimental runs for each point. (a) Fraction of lattice atoms in the ground band versus τ_{hold} extracted from images such as those shown in Fig. 4.5. Two situations are considered: with the bath present (red circles) and absent (blue squares). The solid and dashed lines are exponential fits to the experimental data. (b–c) Condensate fraction and atom number of the bath versus τ_{hold} are shown as red circles. Control data taken with the lattice atoms absent are shown as black triangles.

fraction is approximately constant during the decay process ($\tau_{\text{hold}} \lesssim 20$ ms). At longer hold times, a decrease in condensate fraction is caused by heating induced from spontaneous scattering associated with the lattice light[5]. Regarding the atom number of the bath $N^{(b)}$, we observe an exponential-like decrease over time for all s, which is independent of the presence of the lattice atoms, as shown in (c) of Fig. 4.7. Losses in $N^{(b)}$ are not consistent with calculated rates for three-body recombination [229] and evaporation [230]. Instead, losses are consistent with bath atoms being spontaneously excited to other spin states by the lattice beams [231, 232].

Given the relative small number of lattice atoms, losses in bath atoms $N^{(b)}$ induced by inter-species collisions are too small to be resolved within the noise in $N^{(b)}$[6]. Even though the data suggest a lower $N^{(b)}$ when the lattice atoms are present (triangles versus circles in (c) of Fig. 4.7), the effect is only marginal and further investigation would be required to come to a conclusion.

The fitted decay time constant τ with and without the bath present is shown as data points in Fig. 4.8 for three different lattice depths: $s = 13.5\ \mathrm{E_R}, 16.2\ \mathrm{E_R}$, and $18\ \mathrm{E_R}$. The red circles represent the spin mixture, while the blue squares correspond to the lattice atoms without the bath. For this range of lattice potential depths, the measured decay time constants do not vary strongly with s, and the bath-induced decay rate is at least a factor of two larger than the intrinsic decay rate. In order to gain insight into the band-decay mechanisms experienced by the lattice atoms, we numerical calculate the decay time constants shown in Fig. 4.8 using Fermi's golden rule.

4.5 Fermi's Golden Rule Prediction

We compare the fitted decay time constants with predictions based on a Fermi's golden rule (FGR) calculation without free parameters. We calculate the collisions rate Γ that leads to decay into the ground band using the contact potential for low-energy binary collisions

$$V_{\text{int}} = \frac{4\pi\hbar^2 a_s}{m}\,\delta^3(\mathbf{r}_i - \mathbf{r}_j), \tag{4.11}$$

where $\mathbf{r}_i$ is the location of particle i and a_s is the scattering length. FGR is evaluated using the Fourier expansion

$$V_{\text{int}} = \frac{4\pi\hbar^2 a_s}{mL^3}\sum_{\mathbf{p}'} e^{-\frac{i}{\hbar}\mathbf{p}'\cdot(\mathbf{r}_i-\mathbf{r}_j)}, \tag{4.12}$$

[5]The rate at which a single atom is heated by the lattice beams is discussed in Ref. [77].

[6]The experimental noise in $N^{(b)}$ is comparable to the effect we would like to investigate. Indeed, the expected loss in $N^{(b)} = (36 \pm 5) \times 10^3$ from inter-species collisions is smaller than 10% of $N^{(b)}$, since approximately 5000 lattice atoms are Bragg-excited and only a fraction of them decay to the ground band and induce loss in the bath atoms.

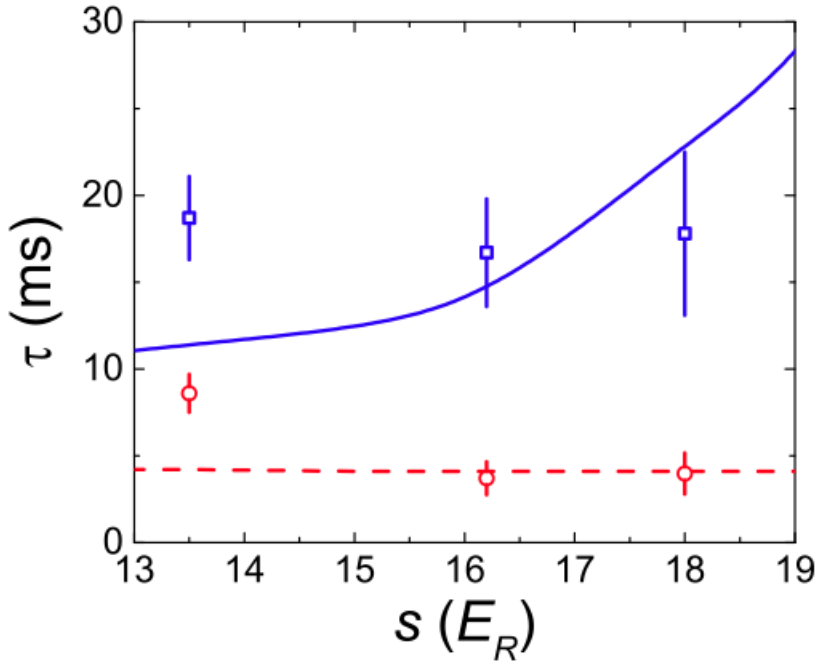

Figure 4.8: Decay time constant at different lattice depths when the bath is present (red circles) and absent (blue squares). The error bars are the uncertainty in the fit to data such as those shown in (a) of Fig. 4.7. The solid and dashed lines are the FGR prediction for $1/\Gamma_{\rm ll}$ and $1/(\Gamma_{\rm ll}+\Gamma_{\rm lb})$, respectively.

where L^3 is the volume of the system, $\mathbf{p}'$ is momentum, and we approximate sums over momentum (or quasi-momentum) by $\sum_{\mathbf{p}'} \to (L/2\pi\hbar)^3 \int d^3p'$. Single-particle quantum states are used for the lattice component, and we only consider atoms in the $n=0$ and $n=1$ bands.

For the intrinsic decay, depicted in (a) of Fig. 4.4, we apply FGR to collisions between two lattice atoms assuming that dynamics are frozen along the x and y directions. The rate for collisions that scatter a pair of atoms with quasimomentum q_{1z} and q_{2z} from the first-excited band ($n=1$) into the ground ($n=0$) and second excited ($n=2$) band is

$$\Gamma_{\rm ll} = \frac{2\pi}{\hbar} \sum_{q'_{1z},q'_{2z}} |\langle \psi^{(0)}_{q'_{1z}} \psi^{(2)}_{q'_{2z}} | V_{\rm int}\left(\mathbf{r}_1-\mathbf{r}_2\right) | \psi^{(1)}_{q_{1z}} \psi^{(1)}_{q_{2z}} \rangle|^2 \delta\left(\epsilon^{(0)}(q'_{1z}) + \epsilon^{(2)}(q'_{2z}) - \epsilon^{(1)}(q_{1z}) - \epsilon^{(1)}(q_{2z})\right), \quad (4.13)$$

where q'_{1z} (q'_{2z}) represents quasimomentum in the band $n=0$ ($n=2$). For determining $\Gamma_{\rm ll}$, we treat the lattice atoms as uniform and contained in a cube of volume L^3. We evaluate $\Gamma_{\rm ll}$ using wavefunctions

$$\psi^{(n)}_{q_{iz}}(\mathbf{r}) = w^{(0)}(x) w^{(0)}(y) \phi^{(n)}_{q_{iz}}(z), \quad (4.14)$$

where $\phi^{(n)}_{q_z}(z)$ is the Bloch wavefunction in band n with quasimomentum q_z along the lattice direction $\hat{z}$,

and $w^{(0)}(x)$ and $w^{(0)}(y)$ are the Wannier wavefunctions for band n along the lattice directions $\hat{x}$ and $\hat{y}$. The coefficients $c_j^{(n)}(q_z)$ for the plane-wave expansion

$$\phi_{q_z}^{(n)}(z) = \frac{e^{\frac{i}{\hbar}q_z z}}{\sqrt{L}} \sum_{j=-\infty}^{\infty} c_j^{(n)}(q_z) e^{i2kjz} \tag{4.15}$$

and the non-interacting lattice dispersion $\epsilon^{(n)}(q_z)$ for band n (Section 1.1.3) are determined numerically (with $k = 2\pi/\lambda$). We truncate the sum over plane-wave components to $|j| \leq 3$ and approximate the Wannier wavefunctions by the harmonic-oscillator ground states of the lattice wells. We average Γ_{ll} over q_{1z} and q_{2z} assuming a uniform distribution of initial quasimomentum, reflecting the high entropy per particle we employ for the lattice component.

Given the non-interacting lattice dispersion $\epsilon^{(n)}(q_z)$ and the range of s we sample, the intrinsic decay process should be prevented by the energy-conserving delta function in Γ_{ll}, and thus, $\Gamma_{\mathrm{ll}} = 0$ (as concluded in Section 4.3.1, at high enough lattice depths, energy conservation can not be fulfilled in binary collisions that scatter non-interacting lattice atoms). The decay we observe is thus evidence that strong interactions may play a central role in dynamics. In order to compare numerical predictions with the measured decay rate, we relax energy conservation and represent the delta function in Γ_{ll} by a Gaussian with root-mean-squared radius

$$U_{\mathrm{ll}} = \frac{4\pi\hbar^2 a_s}{m} \int d^3r \, |w^{(0)}(x)|^4 |w^{(0)}(y)|^4 |w^{(1)}(z)|^4, \tag{4.16}$$

which is the Hubbard interaction energy between atoms in the first-excited band along the z direction and in the ground band in the x and y directions. This approach is inspired by Fermi-liquid theory, in which interactions lead to a finite quasiparticle lifetime and broadening of the spectral function.

To compute the bath-induced decay rate Γ_{lb}, we treat the lattice atoms as confined to single sites of the lattice, which are approximated by three-dimensional harmonic oscillator potentials. The bath atoms are described as a weakly interacting zero-temperature superfluid. We consider energy-conserving collisions between a single lattice atom and the bath that cause the lattice atom to decay from the first to the ground vibrational level along $\hat{z}$ and produce a quasiparticle in the bath with momentum $\mathbf{p}$, as illustrated in (b) of Fig. 4.4. We compute

$$\Gamma_{\mathrm{lb}} = \frac{2\pi}{\hbar} \sum_{\mathbf{p}} |\langle \Phi_{\mathbf{p}}, \psi_{000} | \sum_j V_{\mathrm{int}}(\mathbf{r} - \mathbf{r}_j) | \Phi_0, \psi_{001} \rangle|^2 \delta\left(\varepsilon(\mathbf{p}) - \hbar\omega_z\right), \tag{4.17}$$

where $\mathbf{r}_j$ are the coordinates of the bath atoms, $\mathbf{r}$ is the coordinate of the lattice atom, $|\Phi_0\rangle$ is the ground state of the SF bath, $|\Phi_{\mathbf{p}}\rangle$ is the bath with a Bogoliubov quasiparticle of momentum $\mathbf{p}$ and excitation

spectrum $\varepsilon(\mathbf{p})$, $|\psi_{n_x n_y n_z}\rangle$ is the harmonic oscillator state with quantum numbers n_x, n_y, and n_z, and ω_z is the vibrational frequency of the lattice well along $\hat{z}$ (approximately $E_{\mathrm{bg}}/\hbar$ in the deep lattice limit). The bath is treated as uniform and contained in a cube of volume L^3.

Inserting the interaction potential into Eq. 4.17 leads to

$$\Gamma_{\mathrm{lb}} = \frac{2\pi}{\hbar}\left(\frac{4\pi\hbar^2 a_s}{mL^3}\right)^2 \sum_{\mathbf{p}} |\langle\Phi_{\mathbf{p}}|\sum_j e^{\frac{i}{\hbar}\mathbf{p}\cdot\mathbf{r}_j}|\Phi_0\rangle|^2 \, |\langle\psi_{000}|e^{-\frac{i}{\hbar}\mathbf{p}\cdot\mathbf{r}}|\psi_{001}\rangle|^2 \, \delta\left(\varepsilon(\mathbf{p}) - \hbar\omega_z\right). \tag{4.18}$$

Given that $\hbar\omega_z$ is much greater than the chemical potential of the bath, we approximate the SF dispersion (expressed in Eq. 4.6) as $\varepsilon(p) \approx p^2/2m$, and we use the result

$$|\langle\Phi_{\mathbf{p}}|\sum_j e^{\frac{i}{\hbar}\mathbf{p}\cdot\mathbf{r}_j}|\Phi_0\rangle|^2 = n_0 L^3 \frac{p^2}{2m\varepsilon(p)} \approx n_0 L^3 \tag{4.19}$$

from Refs. [233,234]. The density in the center of the trapped SF is estimated according to the Thomas-Fermi approximation for n_0. The matrix element

$$\langle\psi_{000}|e^{-\frac{i}{\hbar}\mathbf{p}\cdot\mathbf{r}}|\psi_{001}\rangle = \langle\psi_0|e^{-\frac{i}{\hbar}p_x\cdot x}|\psi_0\rangle\langle\psi_0|e^{-\frac{i}{\hbar}p_y\cdot y}|\psi_0\rangle\langle\psi_0|e^{-\frac{i}{\hbar}p_z\cdot z}|\psi_1\rangle \tag{4.20}$$

is evaluated using the formula for coherent coupling between 1D harmonic states presented in Eq. 2.32. The bath-induced decay rate in Eq. 4.18 then becomes

$$\Gamma_{\mathrm{lb}} \approx \frac{2\pi n_0 L^3}{\hbar}\left(\frac{4\pi\hbar^2 a_s}{mL^3}\right)^2 \sum_{p_x,p_y,p_z} \left(\frac{p_z z_0}{\hbar}\right)^2 e^{-\left(\frac{p_x x_0}{\hbar}\right)^2 - \left(\frac{p_y y_0}{\hbar}\right)^2 - \left(\frac{p_z z_0}{\hbar}\right)^2} \, \delta\left(\frac{p^2}{2m} - \hbar\omega_z\right), \tag{4.21}$$

where $x_0 = \sqrt{\hbar/(2m\omega_x)}$, $y_0 = \sqrt{\hbar/(2m\omega_y)}$, and $z_0 = \sqrt{\hbar/(2m\omega_z)}$.

We show predictions for τ with and without the bath present in Fig. 4.8. When the bath is present, we account for both decay channels. The computed intrinsic time constant increases for higher s because the phase space for collisions that conserve momentum and energy within U_{ll} shrinks. In contrast, the bath-induced decay rate is largely independent of s because the bandgap, which determines the density of states of quasiparticle excitations in the bath, depends weakly on the lattice potential depth[7].

The predicted and measured decay time constants τ agree within the experimental uncertainty at $s = 16.2\ \mathrm{E_R}$ and $s = 18\ \mathrm{E_R}$, but disagree significantly at $s = 13.5\ \mathrm{E_R}$. The FGR calculation we implement is limited and should not be expected to entirely model the decay. We ignore the non-zero temperature of the bath and the additional decay channels introduced by off-resonant Bragg excitations to the $n = 2$

[7] If each lattice site is approximated by a parabolic potential, then the bandgap scales as $E_{\mathrm{bg}} \propto \sqrt{s}$.

band, which is noticeable in (b) of Fig. 4.5. Including these effects is computationally intensive because a large number of states must be included. Nevertheless, collisions involving atoms in the $n = 2$ band will tend to increase the decay rate into the ground band, and therefore, our model is expected to overestimate the decay time constant. On the other hand, fully including tunneling or implementing approaches such as dynamical density-matrix renormalization group methods [235] to more accurately treat strong interactions would require significant computational resources and is beyond the scope of this work.

4.6 Conclusions

We have investigated the dissipation mechanisms introduced to a band-excited, strongly interacting MI gas in contact with a weakly interacting superfluid. We have identified two band-decay mechanisms for lattice atoms in the first-excited band. In the intrinsic decay, two excited lattice atoms collide and one particle decays to the ground band, while the second particle is promoted to the second-excited band. In the bath-induced decay, the condensate exchanges energy and momentum with the excited lattice atoms, resulting in an excited lattice atom decaying to the ground band and a Bogoliubov particle is created in the superfluid.

The bath-induced decay is a key element in the cooling scheme proposed in Ref. [58], in which bath atoms act as a thermal reservoir and carry entropy away from the lattice-bound species. We have found that the presence of the bath enhances the intrinsic decay rate and marginally increases the fraction of atoms in the ground band. However, the presence of intrinsic decay, evident in Fig. 4.7, was not considered in Ref. [58] and its occurrence may negatively impact the success of such cooling scheme (a small fraction of intrinsic decay events can deposit a large amount of energy into the lattice gas). This problem could be mitigated by employing a larger ratio $N^{(b)}/N^{(l)}$ to increase the bath-induced decay rate (since the rate is proportional to the bath density) or by utilizing Feshbach resonance [236] to transiently suppress the interactions between lattice atoms.

The measured time constants for the bath-induced decay are in general consistent with the FGR calculations with no free parameters. The discrepancy at $s = 13.5\ \mathrm{E_R}$ may arise from dynamics introduced by atoms promoted to higher energy bands, or from the non-zero temperature of bath. Studying such effects would require more sophisticated techniques and substantial computational power which are beyond the objective of this work.

We have observed that the intrinsic decay rate does not depend strongly on the lattice depth within the range sampled (blue dots in Fig. 4.8). This is inconsistent with suppression of interparticle collisions for deep lattices predicted by our FGR calculation (blue line in Fig. 4.8). The disagreement may indicate that

strong interactions between lattice atoms could play a fundamental role in the intrinsic decay dynamics. The study of quantum dynamics in strongly correlated systems is an active field of research.

In the future, the intrinsic decay process may be important to proposals for Bose condensation via dissipation [202] and techniques for preparing ultracold gases in excited bands of optical lattices [237–240]. Furthermore, the lattice-bath interaction we have demonstrated may be a rich platform for exploring the influence of dissipation on strongly correlated dynamics [213] and on exotic many-particle quantum states, such as excited-orbital superfluids [63, 65, 241–243].

Chapter 5

Quasimomentum Relaxation and Cooling

5.1 Introduction

Over the last decade, optical lattice experiments have proven to be a versatile platform for the study of Hubbard models [80], which are our simplest paradigms of strongly correlated electronic solids [244]. However, our inability to reach temperatures much lower than the magnetic super-exchange energy has prevented us from accessing new quantum regimes, such as the analog of d-wave superconductivity in the cuprates [198]. Several cooling schemes in optical lattices have been proposed, such as immersion cooling [245] and filter cooling [49–55], but experimental demonstrations have been limited [56, 57]. Notably, the kinetic energy, or quasimomentum degree of freedom, has not been cooled directly and remains hotter than the Néel temperature in experiments with fermionic atoms [27].

In this chapter, we have developed and demonstrated a promising novel technique for cooling the quasimomentum distribution of a strongly correlated atomic gas trapped in an optical lattice, which in principle can operate with any atomic species. The entropy of the gas is reduced by ejecting the most energetic atoms from the lattice, in direct analogy to evaporative cooling, where the entropy per particle of the system decreases as atoms with energy greater than the ensemble average escape from the trap [230]. We have also investigated thermalization in this lattice gas. Despite the importance of rapid thermalization to cooling (since any cooling method requires that the cooling power exceed the heating mechanisms present in the system [198]), it has remained essentially unexplored in experiments on strongly correlated quantum system [246]. Remarkably, we have observed gas relaxation faster than the Hubbard parameters $\hbar/t$ and $\hbar/U$, which can not be completely explained by a weakly interacting theory even for a low-density thermal gas.

In the next section, we describe the experimental parameters in our measurements. In Section 5.3, we present a review of stimulated Raman excitation applied to quasimomentum selectivity (which was generically described in Section 2.3.2). In Sections 5.4 and 5.5, we report the rethermalization and cooling measurements, respectively.

5.2 Experimental Procedure

We start the experiments with a partially condensed gas of ^{87}Rb atoms in the $|F = 1, m_F = 0\rangle$ state prepared according to Section 1.1.1. The gas is confined in a 1064 nm crossed dipole trap with a geometric mean of the trap frequencies of $\omega = 2\pi \times (55 \pm 5)$ Hz. The atom number in the trap is $N = (84 \pm 4) \times 10^3$, the temperature is (91 ± 4) nK, and the condensate fraction is $N_0/N = 0.23 \pm 0.02$. A cubic optical lattice formed from three pairs of counter-propagating laser beams with wavelength $\lambda = 812$ nm is exponentially ramped up in 100 ms to a lattice depth s ranging from 4 E_R to 8 E_R ($U/t = 1.3 - 7.4$), where $E_R = \hbar^2\pi^2/2md^2$ is the recoil energy, m is the atomic mass, $h = 2\pi\hbar$ is Planck's constant, and $d = \lambda/2 = 406$ nm is the lattice spacing. A 10.15 G uniform magnetic field is applied to the atom gas to suppress spin-exchange collisions. The lattice-confined atoms are described by the Bose-Hubbard (BH) model (Eq. 1.12) with tunneling energy t and interaction energy U, and the ratio U/t is adjusted by varying s [221]. The range of s and U/t accessed in these measurements corresponds to the superfluid regime of the BH model (the phase diagram of the BH model is illustrated in Fig. 3.2). The initial gas temperature in the lattice potential is (100 ± 15) nK, which is comparable with the bandwidth $12t$ of the ground band (at 4 E_R, $12t \approx 170$ nK $\times k_B$ and at 8 E_R, $12t \approx 60$ nK $\times k_B$). The initial temperature is inferred from the temperature in the parabolic trap using a non-interacting semiclassical calculation that conserves the entropy per particle during the lattice turn-on (Appendix D).

5.3 Quasimomentum-Selective Raman Excitation

We use quasimomentum-selective stimulated Raman excitation to rapidly modify the quasimomentum distribution of the gas. The Raman light couples the ground band ($n = 0$) of the hyperfine state $|\downarrow\rangle = |F = 1, m_F = 0\rangle$ to the first-excited band ($n = 1$) of the hyperfine state $|\uparrow\rangle = |2, 0\rangle$, as depicted in Fig. 5.1. We have chosen to drive Raman excitations between spin states with $m_F = 0$ because this transition is insensitive against first order Zeeman shift, and consequently, robust against magnetic noise. The general theoretical framework of Raman transitions is described in Chapter 2.

In our experimental configuration, the Raman laser beams provide a momentum impulse $\hbar\Delta k = 1.45\, q_B$ to the lattice-confined atoms along the lattice direction $-\hat{z}$ (see part (ii) of Fig. 5.2), where $q_B = \hbar\pi/d$. Such momentum impulse is equivalent to a change in quasimomentum of $\Delta q = 2q_B - 1.45\, q_B = 0.55\, q_B$[1].

As described in Section 2.3.2, selectivity in quasimomentum is enabled by the difference in curvature

[1] The signs of Δk and Δq are with respect to the coordinates shown in Fig. 5.2

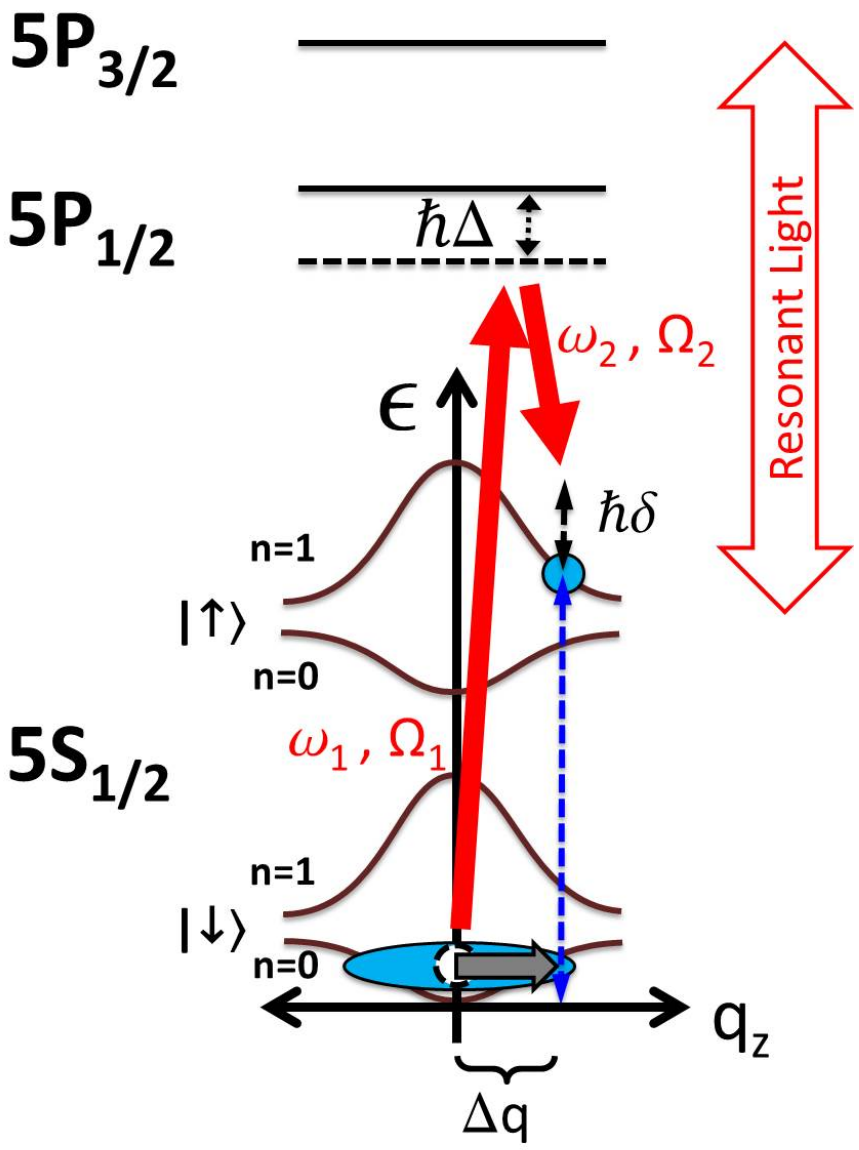

Figure 5.1: Energy diagram of ^{87}Rb confined in a lattice potential that illustrates quasimomentum-selective stimulated Raman excitation (not to scale). Only the ground ($n = 0$) and first-excited ($n = 1$) bands in $|\downarrow\rangle$ and $|\uparrow\rangle$ are shown. A pair of Raman beams (solid red arrows) are used to selectively transfer atoms from $|\downarrow, n = 0\rangle$ to $|\uparrow, n = 1\rangle$. The Raman beams with Rabi rates Ω_1 and Ω_2 are detuned by Δ from the transition to the $5P_{1/2}$ excited electronic state, and provide a quasimomentum impulse $\Delta q = 0.55\, q_B$ to the lattice-confined atoms. The dashed blue arrow indicates the resonance frequency $\omega_0 + [\epsilon^{(1)}(q_z + \Delta q) - \epsilon^{(0)}(q_z)]/\hbar$ between the coupled states. The $|\uparrow\rangle$ atoms are subsequently ejected from the trap using light resonant with the $5S_{1/2}, F = 2 \leftrightarrow 5P_{3/2}$ transition, which is indicated by the hollow arrow.

between the ground and first-excited bands. The quasimomentum-dependent Raman detuning is given by

$$\delta(q_z) = \omega_1 - \omega_2 - \left[\omega_0 + \frac{\epsilon^{(1)}(q_z + \Delta q) - \epsilon^{(0)}(q_z)}{\hbar}\right] \tag{5.1}$$

and it is shown in Fig. 5.1. The quantity $\omega_1 - \omega_2$ is the relative frequency between the Raman beams, $\epsilon^{(0)}(q_z)$ and $\epsilon^{(1)}(q_z)$ are the ground and first-excited energy bands associated with the lattice potential, and the frequency offset ω_0 accounts for the hyperfine splitting and second order Zeeman shift between $|\downarrow\rangle$ and $|\uparrow\rangle$[2]. We measured a frequency offset of $\omega_0 = 2\pi \times (6834.742 \pm 0.001)$ MHz at the quantization field 10.15 G used in the experiments. The terms between brackets in Eq. 5.1 represent the resonance frequency between the states $|\downarrow, n = 0\rangle$ and $|\uparrow, n = 1\rangle$, which is shown as a dashed blue arrow in Fig. 5.1.

When the Raman beams are pulsed on for $\Delta\tau$, the probability of exciting atoms from $|\downarrow, n = 0\rangle$ to $|\uparrow, n = 1\rangle$ in the z direction is given by the Rabi formula

$$P(q_z) = \frac{\Omega^2}{\Omega^2 + \delta(q_z)^2} \sin^2\left(\sqrt{\Omega^2 + \delta(q_z)^2}\frac{\Delta\tau}{2}\right), \tag{5.2}$$

where $\delta(q_z)$ is the effective detuning defined in Eq. 5.1, Ω is the effective Rabi rate given by

$$\Omega = \frac{\Omega_1\Omega_2^*}{2\Delta}\langle\uparrow, n = 1|e^{i\Delta q_z \cdot z/\hbar}|\downarrow, n = 0\rangle, \tag{5.3}$$

Ω_1 and Ω_2 are the Rabi rates associated with each individual Raman beam, and Δ is the detuning from the $5S_{1/2} \leftrightarrow 5P_{1/2}$ transition. The Rabi rates are usually tuned by adjusting the laser light intensities. The quasimomentum selectivity is controlled by choosing an appropriate combination of $\omega_1 - \omega_2$, Ω, and $\Delta\tau$ [245].

5.4 Rethemalization

In our first experiment, we measure the quasimomentum relaxation of a lattice-trapped thermal gas in the superfluid regime of the BH model after its quasimomentum distribution is brought out of equilibrium. We employ quasimomentum-selective stimulated Raman excitation to rapidly remove atoms with low quasimomentum (which include most of the condensed gas) along the z direction of the lattice, i.e., atoms with $q_z \approx 0$.

The experimental sequence starts by pulsing the Raman beams on for 200 μs to excite atoms from $|\downarrow, n =$

[2]The hyperfine splitting between $|\downarrow\rangle$ and $|\uparrow\rangle$ is approximately 6834.6826 MHz [73]. The second order Zeeman shift is a few tens of kHz for a 10 G field.

$0\rangle$ to $|\uparrow, n=1\rangle$. The relative frequency $\omega_1 - \omega_2$ has been tuned to target atoms with low quasimomentum. We sweep $\omega_1 - \omega_2$ across resonance over 1.6 kHz with a central frequency in the range $\omega_1 - \omega_2 = \omega_0 + 2\pi \times (10 - 14.8)$ kHz, which corresponds to the lattice depths $s = (4-8)$ E_R explored in this chapter. The Raman beams are detuned by $\Delta = 2\pi \times 200$ GHz from the $5S_{1/2} \leftrightarrow 5P_{1/2}$ transition and the effective Rabi rates employed vary within the range $\Omega = 2\pi \times (3.2 - 4.2)$ kHz. The experimental sequence is illustrated in Fig. 5.2.

Immediately after the Raman light pulse, atoms in $|\uparrow, n=1\rangle$ are ejected from the trap by pulsing on light resonant with the $5S_{1/2}, F=2 \leftrightarrow 5P_{3/2}$ transition for 50 μs. Thereafter, the remaining out-of-equilibrium quasimomentum distribution is allowed to time evolve in the lattice potential for $\tau_{\text{hold}} = (0-10)$ ms. The atom number of the remaining gas is $N = (40 \pm 6) \times 10^3$. The lattice is then bandmapped in 300 μs and the gas is released from the dipole trap for 20 ms of free expansion. As described in the introduction chapter (Section 1.1.6), bandmapping projects the quasimomentum distribution onto the free particle momentum distribution and, consequently, atoms in excited bands appear outside the first BZ in TOF images.

Fig. 5.2 shows TOF images of intermediate stages of the atom removal procedure. Figure (i) shows the quasimomentum distribution of the gas before the Raman pulse (i.e., all the atoms are in $|\downarrow, n=0\rangle$). Figure (ii) is taken immediately after the Raman pulse excites atoms with low quasimomentum from $|\downarrow, n=0\rangle$ to $|\uparrow, n=1\rangle$. Figure (iii) occurs immediately after the resonant light removes the $|\uparrow, n=1\rangle$ atoms from the trap.

We show characteristic TOF images at different lattice hold times τ_{hold} in the inset of Fig. 5.3. We observe that the quasimomentum distribution relaxes to the equilibrium distribution as τ_{hold} increases. The gas becomes thermal once the condensed atoms are removed from the gas.

5.4.1 Image Processing

To quantify the quasimomentum relaxation of the gas, we fit a non-interacting semiclassical model to each TOF image. The model describes the equilibrium quasimomentum distribution of a non-interacting bosonic gas trapped in a combined lattice-parabolic potential (Appendix E). The model, projected onto the imaging plane, is given by

$$n(q_2, q_3) = A \sum_{j=1}^{\infty} \frac{e^{-2j\beta t(3-\cos b)} z^j}{j^{3/2}} \left[(\pi - a) I_0(\alpha_j) + 2 \sum_{l=1}^{\infty} I_l(\alpha_j) \frac{\sin l(\pi - a)}{l} \right], \tag{5.4}$$

where q_2 and q_3 are the horizontal and vertical directions in the absorption images, respectively (see Eq. E.2 and Fig. E.1), z is fugacity, I_l is the modified Bessel function of the first kind, $\alpha_j = 4j\beta t \cos a$, $a =$

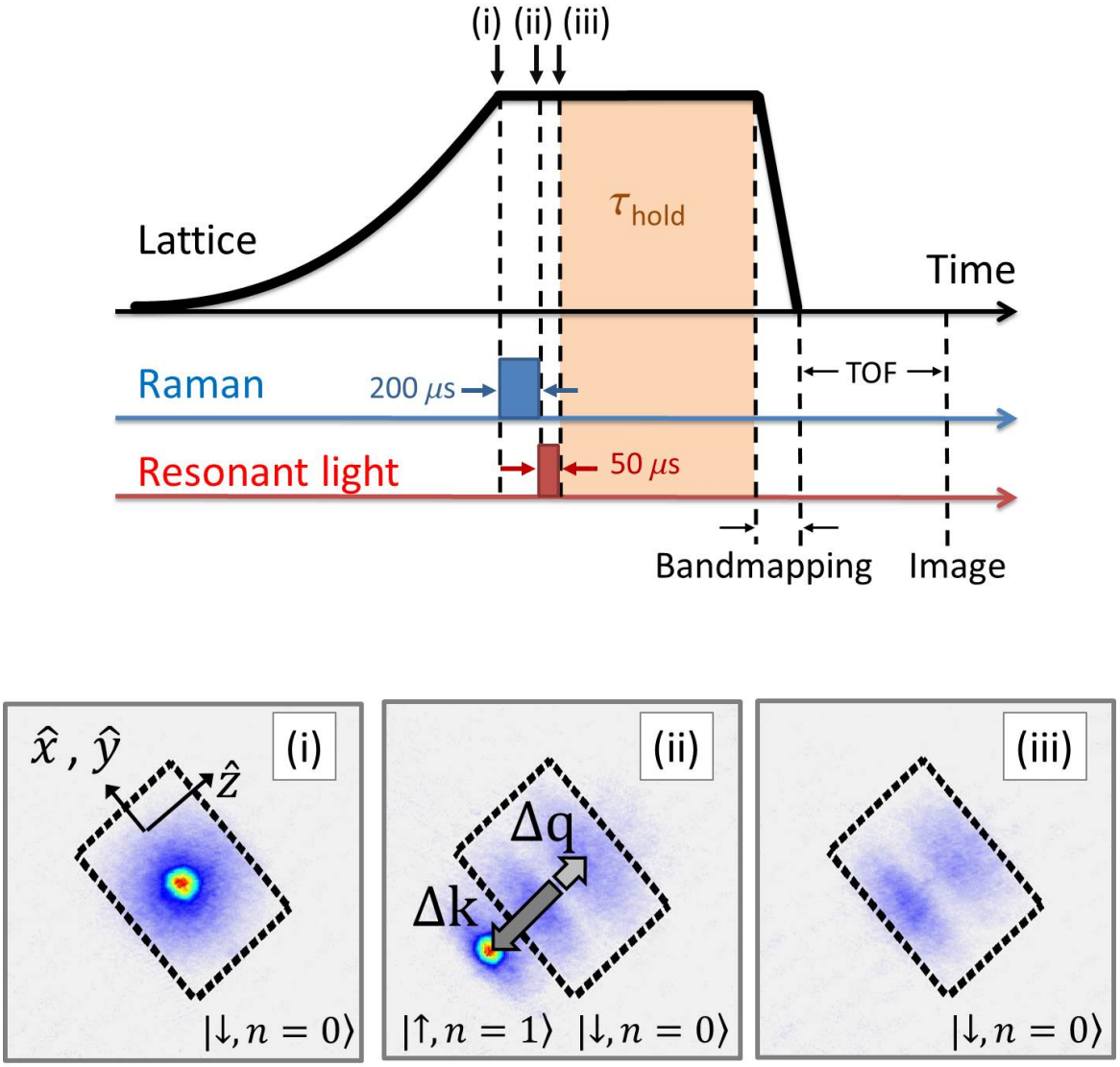

Figure 5.2: Experimental sequence for measuring thermalization in a lattice-trapped gas (not to scale). The lattice potential is ramped up exponentially in 100 ms. The Raman light is pulsed on for 200 μs and the relative detuning is tuned to target low quasimomentum. A resonant light is then pulsed on for 50 μs and the gas is subsequently allowed to relax in the lattice potential for τ_{hold}. Absorption images are taken after bandmapping in 300 μs and 20 ms of TOF. Figures (i)-(iii) are TOF images showing intermediate steps of the sequence. The images have been obtained before (i) and immediately after (ii) the Raman pulse; and subsequent to the resonant pulse (iii). The lattice directions are indicated by $\hat{x}, \hat{y}$, and $\hat{z}$. The Raman beams excite atoms in $|\downarrow, n = 0\rangle$ with $q_z \approx 0$ to $|\uparrow, n = 1\rangle$ with $q_z \approx 0.55 q_B$ (light grey arrow). After bandmapping, atoms in $|\uparrow, n = 1\rangle$ appear outside the first BZ with momentum $p_z \approx -1.45 q_B$ (dark grey arrow). The projection of the first BZ onto the imaging plane is displayed with dashed lines.

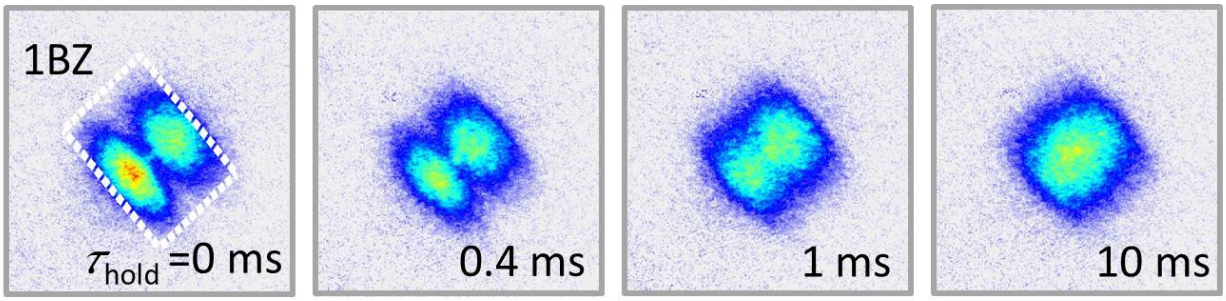

Figure 5.3: Typical TOF images of the gas after being brought out of equilibrium and held in the lattice potential for τ_{hold}. The white line marks the first BZ.

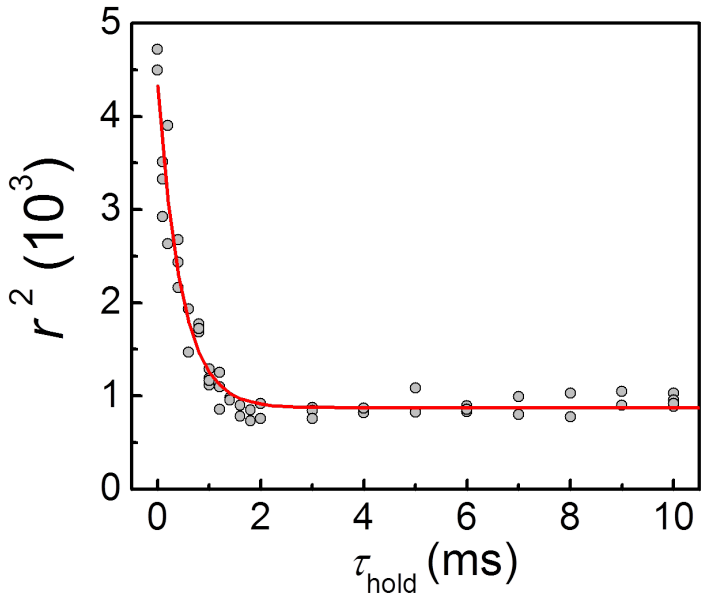

Figure 5.4: Mean squared residual r^2 versus τ_{hold} for $s = 6$ $\mathrm{E_R}$. The measure r^2 is defined in Eq. 5.5 and quantifies the relaxation of the gas in quasimomentum. Each data point corresponds to a single measurement on an image such as those shown in Fig. 5.3. The red line is a single exponential-decay fit used to determine the relaxation time constant τ. The offset from zero is consistent with imaging noise and failure of bandmapping at the edge of the first BZ.

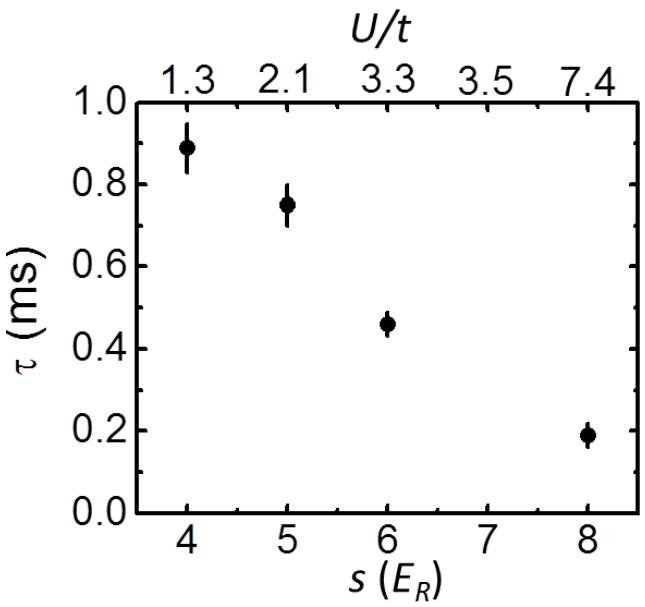

Figure 5.5: Relaxation time constant for r^2 at different lattice depths. These values are obtained from a single exponential-decay fit to r^2 versus τ_{hold} such as that shown in Fig. 5.4 for $s = 6$ E_R. Because r^2 relaxes exponentially in time, atoms with quasimomentum $q_z \approx 0$ relax to equilibrium with an exponential time constant of 2τ. The error bars display the fit uncertainty.

$\pi|q_2 - q_3|/(2q_B)$, $b = \pi(q_2 + q_3)/(\sqrt{2}q_B)$, $\beta = 1/k_B T$, $q_B = \hbar\pi/d$, and A is a fitting constant. The derivation of Eq. 5.4 is presented in Appendix E.

To measure the deviation of the quasimomentum distribution of the gas from equilibrium, we define the mean squared residual of the fit as

$$r^2 = \frac{\sum_{ij}(\mathcal{OD}_{ij} - n_{ij})^2}{\sum_{ij} 1}, \tag{5.5}$$

where $\mathcal{OD}_{ij}$ is the optical depth of the absorption image, n_{ij} is the fit function given by Eq. 5.4 after expansion time, and the summations in i and j extend over a mask that covers the first Brillouin zone (BZ) projected onto the imaging plane. The mask size is reduced by 20% at the edge of the first BZ along $\hat{z}$ to account for failure of bandmapping [86]. We also mask out the residual condensate (less than 6% of the initial condensate which occasionally remains in $|\downarrow, n = 0\rangle$) using a circular mask with twice the Thomas-Fermi radius. We measure r^2 versus τ_{hold} for four different lattice depths: $s = 4, 5, 6$, and 8 E_R. Fig. 5.4 shows r^2 versus τ_{hold} for the particular case of $s = 6$ E_R. For all lattice depths, we find that r^2 versus τ_{hold} is well described by a single exponential-decay fit, from which we extract a decay time constant τ. Because r^2 relaxes exponentially in time, we conclude that atoms with quasimomentum $q_z \approx 0$ relax to equilibrium with an exponential time constant of 2τ.

In Fig. 5.5, we show τ for different lattice depths s. The relaxation time speeds up for a stronger lattice

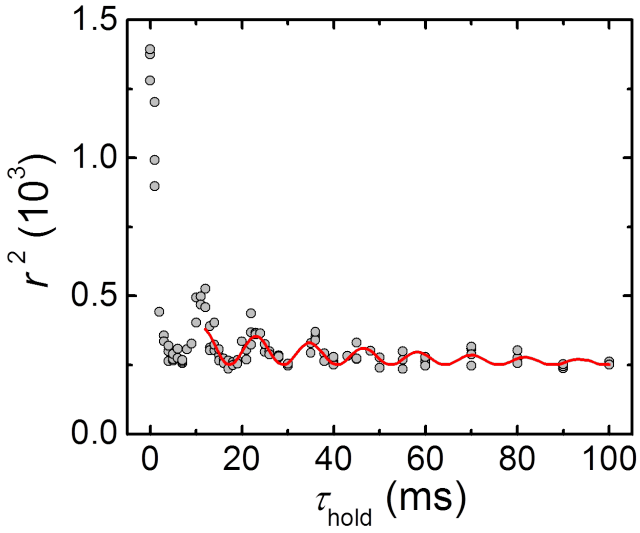

Figure 5.6: Relaxation of a thermal gas in a harmonic trap. The plot shows r^2 versus τ_{hold}, where r^2 is the mean squared residual of a gaussian fit (defined in Eq. 5.5), and τ_{hold} is the evolution time in the harmonic trap. Individual points are single measurements, and the red line is a damped sine-squared fit to the linear response regime ($\tau_{\text{hold}} > 12$ ms). The measured oscillation period is (11.7 ± 0.2) ms, and the damping time constant is (44 ± 10) ms. The offset is consistent with imaging noise.

potential, ultimately reaching just $2\tau \approx 400$ μs at $s = 8$ E_R. The quasimomentum relaxation is always faster than the timescale associated with both Hubbard energies, which lie within the range $\hbar/t = (0.5 - 1.5)$ ms and $\hbar/U = (0.2 - 0.4)$ ms for the lattice depths $s = (4 - 8)$ E_R sampled. Additionally, the relaxation time is approximately two orders of magnitude faster than the time constant observed in the harmonic trap, as we will discuss in the next subsection.

5.4.2 Momentum Relaxation in a Harmonic Trap

In order to test and validate our r^2 analysis, we apply the same relaxation measurement to a gas confined in a parabolic trap (i.e., without the lattice potential). Given that the thermodynamic properties of a weakly interacting, semi-classical gas are well understood, we compare the experimental results against theoretical calculations and numerical simulations.

We begin the measurement with a partially condensed gas with initial parameters similar to those used in the lattice experiment. The gas is brought out of equilibrium by rapidly removing atoms with low momentum along $\hat{z}$. The remaining atoms are allowed to relax for $\tau_{\text{hold}} = (0 - 100)$ ms and we fit a gaussian distribution to each TOF image to determine the mean squared residual r^2.

We plot r^2 versus τ_{hold} in Fig. 5.6. We observe damped oscillations in r^2 with a frequency matching that of the harmonic trap. The data for $\tau_{\text{hold}} > 12$ ms fit well to a damped sine-squared function with a damping

time constant of (44 ± 10) ms. We exclude data taken at short τ_{hold} when the gas is far from equilibrium, since the relaxation does not appear to be exponential in that region.

In a classical gas, the rate of (total) collisions is given by [247]

$$\Gamma = \sigma n_{\text{dwd}} v_{\text{rel}}, \tag{5.6}$$

where $\sigma = 8\pi a_s^2$ is the elastic collision cross section, a_s is the s-wave scattering length, n_{dwd} is the density-weighted density defined as

$$n_{\text{dwd}} = \int d^3r \; n(\mathbf{r}) \; n(\mathbf{r}), \tag{5.7}$$

$n(\mathbf{r})$ is the gas density, v_{rel} is the mean relative speed defined as

$$v_{\text{rel}} = \frac{1}{N^2} \iint d^3p_1 \, d^3p_2 \; \frac{|\mathbf{p}_1 - \mathbf{p}_2|}{m} \; \Pi(\mathbf{p}_1)\Pi(\mathbf{p}_2), \tag{5.8}$$

$\Pi(\mathbf{p})$ is the momentum distribution of the gas, and N is the atom number. For the particular case of a harmonic trap we find

$$n_{\text{dwd}} = N^2 \left(\frac{m\omega^2}{4\pi k_B T} \right)^{3/2} \tag{5.9}$$

and

$$v_{\text{rel}} = \left(\frac{16 k_B T}{\pi m} \right)^{1/2}. \tag{5.10}$$

Under experimental parameters, we find that Eq. 5.6 predicts a collision time of $N/\Gamma = 150 \pm 40$ ms. In order to relate the predicted collision time to the damping time measured in Fig. 5.6, we use a 3D molecular dynamics simulation of hard spheres confined in a harmonic trap to determine the average number of collisions required for rethermalization after the gas is brought out of equilibrium. We consider 5000 particles with an initial Maxwell-Boltzmann distribution of velocities and positions. At the beginning of the simulation, particles with speeds 20% smaller than the average are removed along one direction, which approximately emulates the experimental procedure. Particle trajectories are then propagated using the velocity-Verlet method. When an overlap between two particles is detected, the direction of the relative velocity is randomized to simulate s-wave collisions (while preserving the center-of-mass velocity of the pair). The velocity distribution is analyzed at each time step to compute the residual from the equilibrium distribution. We observe behavior similar to that displayed in Fig. 5.6. A fit of an exponentially damped oscillatory function to r^2 versus the evolution time indicates that the damping time constant corresponds to 0.5 collision per particle for a wide range of particle diameters. Therefore, the measured time constant for

relaxation in the dipole trap is consistent with N/Γ within a factor of two. The discrepancy between the measured time constant and the inferred collision rate may arise from systematic uncertainty in the number of particles, trap anharmonicity, and quantum degeneracy effects [248].

5.4.3 Fermi's Golden Rule Prediction

The measured time constants shown in Fig. 5.5 are compared to a short-range, two-body scattering calculation based on Fermi's golden rule (FGR), treating the Hubbard interaction term as a perturbation to the single-particle tight-binding Hamiltonian[3]. This mechanism, which is analogous to electron-electron scattering, is distinct from the kinetic processes, such as electron-phonon and electron-impurity interactions that dominate in most solid-state systems.

We consider a 3D classical gas initially at equilibrium in a cubic lattice potential plus an overall harmonic confinement. We remove all the atoms at $\mathbf{q} = 0$ and we calculate the relaxation rate of the occupation number $\mathbb{n}_{\mathbf{q}=0}$ to the equilibrium value. The relaxation time τ predicted by FGR is given by[4]

$$\frac{1}{\tau} = \frac{4}{\hbar}\langle \mathbb{n} \rangle F\left(\frac{t}{k_B T}\right)\frac{U^2}{t}, \tag{5.11}$$

where the function F is plotted in Fig. 5.7 and is given by the integral

$$F(x) = \frac{\int \frac{d^3\theta_1}{(2\pi)^3}\frac{d^3\theta_2}{(2\pi)^3} e^{-2x[C(\boldsymbol{\theta}_1)+C(\boldsymbol{\theta}_2)]} 2\pi\delta(2C(\boldsymbol{\theta}_1)+2C(\boldsymbol{\theta}_2)-2C(\boldsymbol{\theta}_1+\boldsymbol{\theta}_2))}{\int \frac{d^3\boldsymbol{\theta}}{(2\pi)^3} e^{-2xC(\boldsymbol{\theta})}}, \tag{5.12}$$

with $C(\boldsymbol{\theta}) = \sum_{i=x,y,z}(1-\cos\theta_i)$. The density-weighted average lattice filling $\langle \mathbb{n} \rangle$ of the harmonically-trapped gas is given by

$$\langle \mathbb{n} \rangle = N\left(\frac{m\omega^2 d^2}{4\pi k_B T}\right)^{3/2}, \tag{5.13}$$

where N is the atom number and T is the temperature of the gas before it is brought out of equilibrium. The derivation of Eq. 5.11 is presented in Appendix G.

We compare the relaxation times predicted by Eq. 5.11 with the experimental values shown in Fig. 5.5. The initial gas temperature in the lattice (before bringing the gas out of equilibrium) is in the range $T_i = (96 - 102)$ nK and the corresponding lattice filling is $\langle \mathbb{n}_i \rangle = 0.11 - 0.16$. The temperature is inferred by matching the entropy per particle in the lattice to that of the harmonic trap (i.e., before loading the gas into the lattice potential) using non-interacting semiclassical thermodynamics (Appendix D). For the

[3] At $s = 8\ \mathrm{E_R}$, $U \approx 0.23\ \mathrm{E_R}$ is only marginally smaller than the ground-band bandwidth $12t \approx 0.38\ \mathrm{E_R}$. Beyond this regime, interaction effects become dominant, and therefore, perturbation theories break down.

[4] This formula was derived by Professor Erich Mueller (Cornell University).

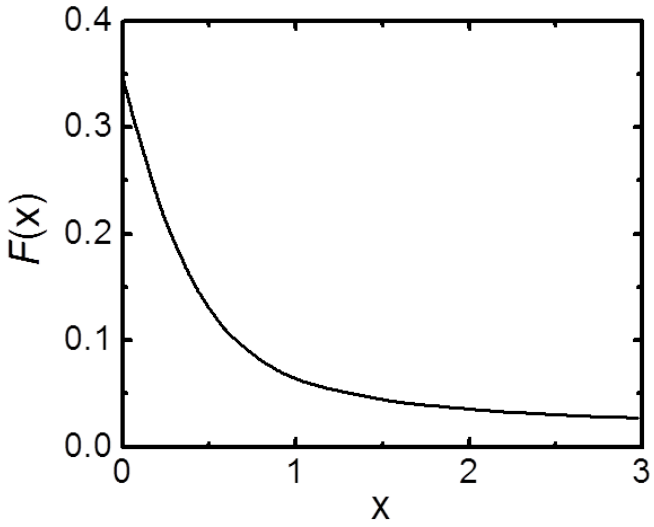

Figure 5.7: Function $F(x)$ from the FGR calculation. $F(x)$ is defined in Eq. 5.12.

range $s = (4-8)$ E_R probed, the tunneling energy is in the range $t/k_BT \approx 0.07-0.14$, and therefore, $F(t/k_BT) \approx 0.3$. We have also inferred the gas temperature after equilibration in the lattice by measuring the temperature in the parabolic trap after slowly ramping down the lattice in 100 ms. The equilibrium temperature in the lattice is in the range $T_f = (184-223)$ nK. The corresponding lattice filling is in the range $\langle n_f \rangle = 0.04-0.05$ and $F(t/k_BT) \approx 0.3$. As mentioned before, the atom number in the lattice potential is $N = (40 \pm 6) \times 10^3$.

In Fig. 5.8, we plot the measured relaxation rate $1/\tau$ (normalized by the Hubbard tunneling rate $t/\hbar$) versus U^2/t^2. The dotted line represents Eq. 5.11. No free parameters were used for the theoretically predicted τ, which is only constrained by the known experimental values. We have used the initial lattice filling $\langle n_i \rangle = 0.13$ averaged across all lattice depths. By contrast, the final lattice filling (i.e., after relaxation of the gas) does not reproduce the experimental results.

We find excellent quantitative agreement between the predicted and the measured relaxation rates at $s = 6$ E_R and $s = 8$ E_R. This agreement is surprising considering that the relaxation time is short compared with the time for an atom to tunnel between neighboring lattice sites, a condition that corresponds to a mean-free path shorter than the lattice spacing and a violation of the Mott-Ioffe-Regel (MIR) bound [249]. The MIR limit is the requirement that the uncertainty in the quasimomentum of a particle must be less than the extend of the BZ for a semiclassical transport theory to be valid. The breakdown of the MIR bound has been associated with unusual transport phenomena in metallic compounds that are not completely understood. Remarkably, our simple kinetic theory works in this regime, even though it fails to capture rethermalization

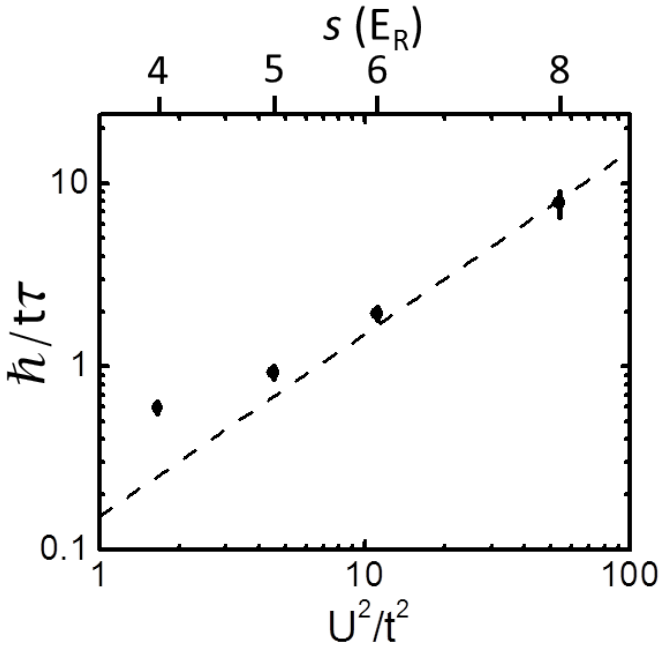

Figure 5.8: Normalized relaxation rate $\hbar/t\tau$ versus U^2/t^2. The dashed line represents the scaling law predicted by Eq. 5.11 using $\langle \mathbb{n}_i \rangle = 0.13$ and $F(t/k_BT) = 0.3$. No free parameters were used in the theoretically prediction. The points show the measured relaxation rate in Fig. 5.5. The error bars include the fit uncertainty used to determine τ and the standard deviation of the mean temperature and atom number.

time at lower lattice depths. The measured normalized relaxation time does not scale linearly with U^2/t^2 and decreases less rapidly with U^2/t^2 than predicted by Eq. 5.11. The time constant τ is therefore smaller (and the rethermalization rate faster) at lower lattice depths than the FGR prediction, which is surprising because one would expect a perturbative calculation in U/t to be more accurate at lower lattice depths (where interactions are weaker) and to break down as the lattice depth and interaction strength increase. The failure of a scattering model at low lattice depths may be related to the long-debated breakdown of quasiparticles and Fermi liquid theory in the low density limit of the Hubbard model (see Ref. [250], for example).

5.5 Quasimomentum-Selective Raman Cooling

In a second experiment, we have demonstrated a novel technique for reducing the entropy of a superfluid gas in an optical lattice which, in principle, works with any atomic species. The extraordinarily fast relaxation in quasimomentum (compared with $\hbar/t$ and $\hbar/U$) we observe enables efficient cooling by iteratively removing the most energetic atoms of the gas from the ground band, in direct analogy to evaporative cooling [230].

In a proof-of-principle experiment, we demonstrate cooling in a partially condensed gas trapped in a 4 E_R

optical lattice. The ^{87}Rb gas is prepared in the same hyperfine state and with the same initial conditions as in the thermalization experiment. After the lattice potential is ramped up to 4 E_R ($U/t \approx 1.3$) in 100 ms, the Raman beams and resonant light are consecutively pulsed on for $\Delta\tau = 400$ μs and 50 μs. For this experiment, each Raman pulse is designed to remove only atoms with high quasimomentum, whereas the condensate is left largely unaffected. The spatial configuration of the Raman beams allows to remove atoms from one side of the first BZ along the z direction, as shown in (ii) of Fig. 5.9. After the resonant pulse, a 1 ms delay before the start of the next cooling cycle is included to allow the quasimomentum distribution to equilibrate. After all the cycles are completed, the gas is held in the lattice potential for 4 ms before bandmapping in 300 μs and TOF imaging. Fig. 5.9 illustrates the full experimental sequence.

The Raman beams couple the same spin states used in the thermalization experiment (i.e., $|\downarrow, n = 0\rangle$ and $|\uparrow, n = 1\rangle$), and the momentum impulse is also the same (i.e., $\Delta q = 0.55\, q_B$). The beams are detuned by $\Delta = 2\pi \times 430$ GHz from the $5S_{1/2} \leftrightarrow 5P_{1/2}$ transition, and the effective Rabi rate is $\Omega = 2\pi \times 1.0$ kHz[5]. For the first cooling cycle, we use $\omega_1 - \omega_2 = \omega_0 + 2\pi \times 15.8$ kHz[6]. For the second cycle, we use $\omega_1 - \omega_2 = \omega_0 + 2\pi \times 16$ kHz instead to target quasimomenta slightly closer to $q_z = 0$. The optimal Raman parameters were found through maximization of the resulting condensate fraction.

In parts (i) and (ii) of Fig. 5.9, we show the quasimomentum distribution (projected onto the imaging plane) immediately before and after atoms have been removed from the thermal component. In Fig. 5.10, we plot the excitation probability $P(q_z)$ in Eq. 5.2 using the experimental parameters. The plot is qualitatively consistent with the experimental image observed in (ii) of Fig. 5.9.

5.5.1 Cooling Power and Efficiency

We present the results from the cooling experiment in (a)–(d) of Fig. 5.11. In (a), we show the quasimomentum profile of the gas along $\hat{z}$ before (black) and after (shaded gray) two cooling cycles. We observe that the width of the thermal component shrinks and the condensate number grows as the cooling sequence is performed. For a quantitative analysis, we fit the TOF images using Eq. 5.4 plus an independent Thomas-Fermi profile for the condensate. From the fit, we determine the number of thermal and condensed atoms, the condensate fraction N_0/N and the parameter $\beta t = t/k_B T$ which estimates the temperature of the gas.

The results of the semiclassical fits are shown in (b)–(d) of Fig. 5.11. In (b), we show the atom number in the thermal component (N) and in the condensate (N_0) as the cooling cycles are performed. We observe that N decreases, since atoms are expelled from the trap, whereas N_0 increases because of redistribution of atoms from the thermal component to the condensate. We interpret this redistribution as a sign of

[5] At this Rabi rate, the pulse length applied is nearly a π-pulse.
[6] The relative Raman frequency $\omega_1 - \omega_2$ remains fixed during each Raman pulse.

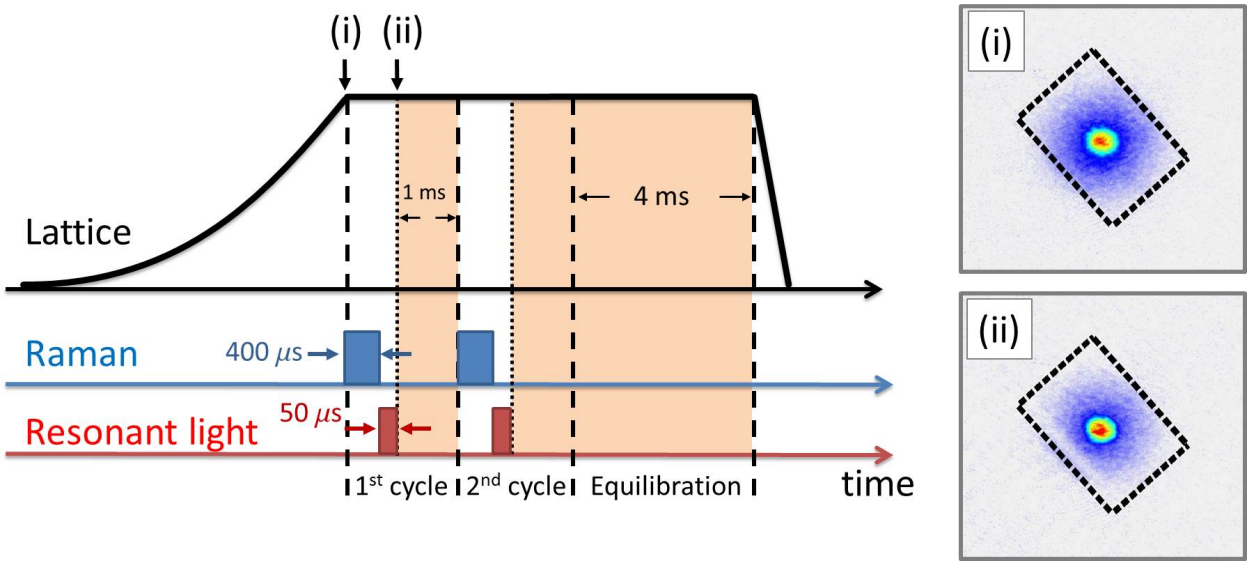

Figure 5.9: Experimental sequence for cooling a lattice-confined gas using quasimomentum-selective stimulated Raman excitation (not to scale). During each cooling cycle, the Raman and resonant lights are pulsed on for 400 μs and 50 μs, respectively. In a proof-of-principle experiment, we have carried out two cooling cycles followed by 4 ms of equilibration time. Absorption images show the quasimomentum distribution before a Raman pulse (i) and after a resonant-light pulse (ii).

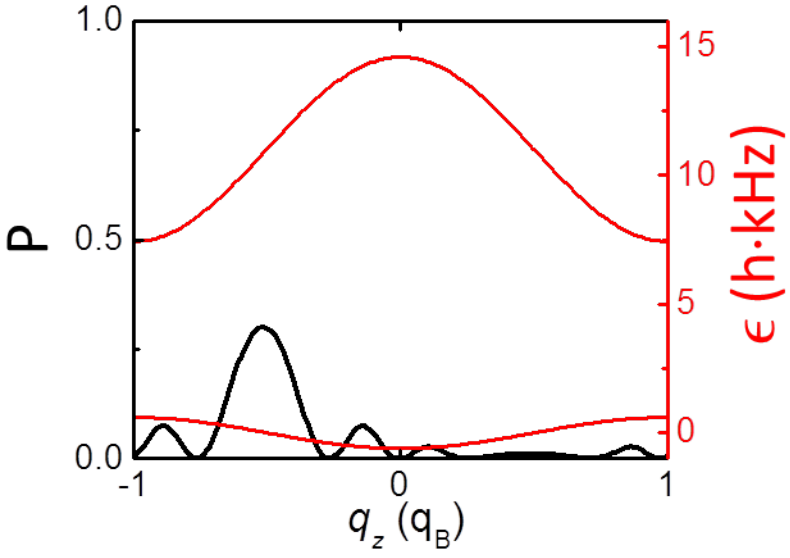

Figure 5.10: Probability of exciting a particle from $|\downarrow, n = 0\rangle$ to $|\uparrow, n = 1\rangle$ using a Raman pulse along q_z (black line). The plot is calculated using Eq. 5.2 with $\Delta q = 0.55\, q_B$, $\omega_1 - \omega_2 = \omega_0 + (2\pi) \times 15.8$ kHz, $\Omega = (2\pi) \times 1$ kHz, and $\Delta\tau = 0.4$ ms. The probability profile qualitatively agrees with the experimental image in (ii) of Fig. 5.9. The red lines show the energy bands $\epsilon^{(0)}$ and $\epsilon^{(1)}$ in the tight-binding approximation (the frequency offset ω_0 is not shown).

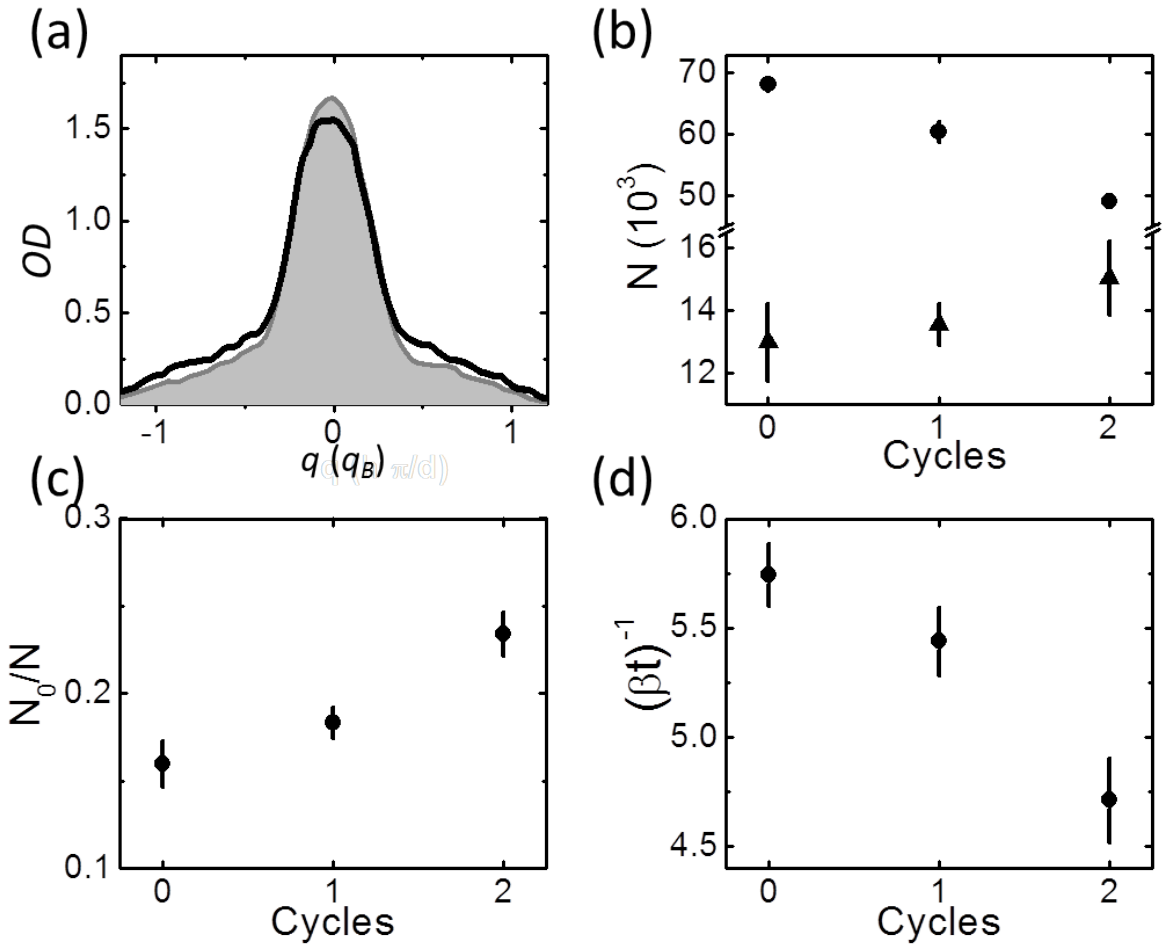

Figure 5.11: Observables in the cooling experiment. (a) Quasimomentum profile along $\hat{z}$ averaged over $3-4$ images before (black) and after (gray-shaded) two cooling cycles. (b) Atom number in the condensate (triangles) and in the thermal component (circles) as the cooling cycles are performed. (c) and (d) show the condensate fraction and the fit parameter βt, respectively, versus the cooling cycles (T is monotonically related to $1/(\beta t)$). Plots (b)–(d) are obtained by fitting the TOF images to a non-interacting semiclassical model plus a Thomas-Fermi profile. The error bars represent the standard error of the mean.

rethermalization of the gas during the cooling sequence. Moreover, the steady increase in the condensate fraction N_0/N shown in (c) is a direct evidence for reduction of entropy per particle during cooling. This technique, therefore, may be used to reach new quantum phases that exist at ultra low entropies.

In part (d) of Fig. 5.11, we plot the parameter βt obtained from the semiclassical fit. Even though temperature can not be accurately determined from $\beta t = t/k_B T$ because bandmapping fails at the edge of the first BZ (refer to Section 1.1.6), $1/(\beta t)$ is monotonically related to T [85], and therefore, a decrease in $1/(\beta t)$ is an unambiguous signal of reduction in temperature, as we observe in the plot. Such decrease in temperature further suggests that the gas has achieved thermal equilibrium during cooling.

A measure of efficiency for any evaporative cooling scheme is

$$\alpha = \frac{d \log N}{d \log T}. \tag{5.14}$$

A small value of α indicates efficient cooling—fewer atoms are removed for the same change in T. To calculate α for our method, we use the values of N shown in (b) of Fig. 5.11, and we estimate T by matching the condensate fraction measured in (c) to that obtained from a semiclassical model (Appendix D). The resulting efficiency parameter is $\alpha = 1.75 \pm 0.04$. This performance compares favorably with recent results for non-lattice gases, including $\alpha \approx 1.5$ and 1.9 for "tilt" evaporation in a hybrid magnetic-optical trap [67, 251] and $\alpha \approx 2.7$ for dipole-trap evaporation of ^{87}Rb [252].

The ultimate limit to the lowest temperature achievable by any cooling method is determined by competition between cooling and heating rates—cooling ceases when the two are equal. The heating rate in optical lattices is primarily determined by momentum diffusion resulting from the interaction between the laser light and atoms [253]. This effect can be minimized by detuning the laser far from any electronic transition. In our experiment, the heating rate induced by the three lattice beams is 0.15 E_R/s = 25 pK/ms at $s = 4$ E_R (estimated using Eq. 1.10), while the cooling power, based on the data shown in (c) of Fig. 5.11, is approximately 9 nK $\times$ k_B/ms (corresponding to $0.6\, t/ms$). This extraordinary cooling power is possible because of the high thermalization rate. In the regime we explore, heating from the lattice is not a limitation to the cooling method. An analysis of the cooling power at lower temperatures and for fermions would require developing a method for quantitatively predicting the thermalization rate.

In principle, more cooling cycles could have been carried out in our experiment, since there are no technical limitations to this method other than phase noise in the Raman pulses. However, temperature drift in the gas preparation (via forced evaporative cooling in the dipole trap) has constrained our time window for data acquisition. In the next subsection, we will see that the ultimate cooling limit of this

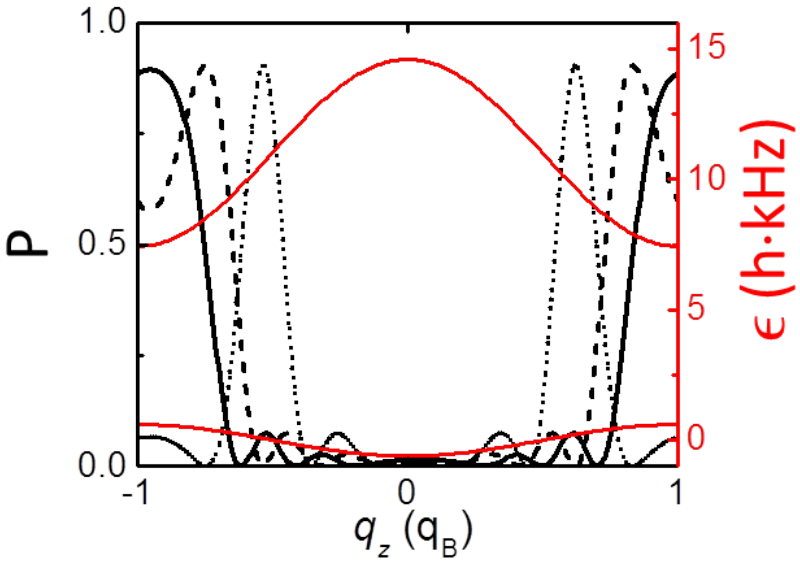

Figure 5.12: Excitation probability of a Raman pulse when $\Delta q = 0.05\, q_B$ (black lines). As shown in this plot, both sides of the first BZ can be addressed simultaneously when Δq is small enough compared with q_B. The parameters used in this calculation are $s = 4$ $\mathrm{E_R}$, $\Delta q = 0.05\, q_B$, $\Omega = (2\pi) \times 1$ kHz, $\Delta\tau = 0.4$ ms, and three different detunings: $\omega_1 - \omega_2 = \omega_0 + (2\pi) \times 6.7$ kHz (solid), $\omega_1 - \omega_2 = \omega_0 + (2\pi) \times 7.7$ kHz (dashed), and $\omega_1 - \omega_2 = \omega_0 + (2\pi) \times 10$ kHz (dotted). The red lines show the energy bands $\epsilon^{(0)}$ and $\epsilon^{(1)}$ in the tight-binding approximation. The frequency offset ω_0 is not shown.

technique, as applied to bosonic atoms, is determined by selectivity in quasimomentum together with the finite momentum spread of the condensate.

5.5.2 Scalability

In our proof-of-principle cooling experiment, the quasimomentum impulse $\Delta q = 0.55\, q_B$ employed only allows removing atoms from one side of the first BZ at a time (along $\hat{z}$). A more efficiency scheme would be to address both sides of the BZ simultaneously, which could be achieved by using a smaller Δq compared with $q_B = \hbar\pi/d$. As an example, in Fig. 5.12 we use Eq. 5.2 to predict the excitation profile for $\Delta q = 0.05\, q_B$ (black lines). We observe that both sides of the first BZ can be targeted simultaneously (solid) and, furthermore, different quasimomenta can be progressively targeted by adjusting the relative Raman frequency $\omega_1 - \omega_2$ (dashed and dotted). In practice, a small Δk could be implemented by using a small relative angle between the Raman beams. The drawback of this configuration is the need for more laser power given that the effective Rabi rate decreases with Δk, as shown in (a) of Fig. 2.3.

The cooling efficiency can be further improved by simultaneously driving quasimomentum-selective Raman excitation along more lattice directions. In practice, this can be achieved by implementing additional

Raman beams in the system. We numerically investigate the cooling performance under realistic heating mechanisms when the cooling sequence is simultaneously applied along one, two, and three lattice directions. We start the simulation with a non-interacting semiclassical model which describes the 3D equilibrium quasimomentum distribution of a bosonic gas in a lattice potential (Appendix D). We emulate the atom-removal step by truncating the quasimomentum distribution beyond a certain threshold $\varepsilon \cdot q_B$ (exemplified in (f) of Fig. 5.13), where ε ranges from 0 to 1. Subsequently, we emulate the rethermalization process by calculating the new equilibrium temperature of the system via energy conservation. For example, in the case of cooling along three lattice directions, the truncated kinetic energy is given by

$$K_\varepsilon(T_0) = \int_{-\varepsilon\cdot q_B}^{\varepsilon\cdot q_B}\int_{-\varepsilon\cdot q_B}^{\varepsilon\cdot q_B}\int_{-\varepsilon\cdot q_B}^{\varepsilon\cdot q_B} d^3q \quad 2t \sum_{i=x,y,z} \left[1-\cos\left(\pi q_i/q_B\right)\right] n(q_x,q_y,q_z), \tag{5.15}$$

where $n(q_x, q_y, q_z)$ is the equilibrium quasimomentum distribution at temperature T_0 (Eq. D.10). The new equilibrium temperature T_1 after thermalization is determined from

$$K(T_1) + V(T_1) = K_\varepsilon(T_0) + V(T_0) + \dot{E}\Delta\tau, \tag{5.16}$$

where $\dot{E}$ is the heating rate associated with the three lattice beams ($\dot{E} = 25$ pK/ms at $s = 4$ E_R), $\Delta\tau$ is the duration of a cooling cycle, and K and V are the equilibrium kinetic and potential energies of the gas (Appendix D).

In Fig. 5.13, we show the cooling simulation performed on a 3D gas with initial atom number $N = 1\times10^5$, temperature $T = 50$ nK, and condensate fraction $N_0/N \approx 0.6$. We iteratively reduce the cutoff parameter ε using the exponential function shown in (a), which has not been optimized. In (b)–(e), we show the atom number N, gas temperature T, condensate fraction N_0/N and entropy per particle S/N versus the number of cooling cycles. The 1/2D line (black squares) corresponds to the case where atoms are removed from one side of the first BZ along one of the lattice vectors, as we have demonstrated experimentally. The 1D line (red circles) represents the case where atoms on both sides of the first BZ are addressed simultaneously. The 2D (blue triangles) and 3D (magenta diamonds) cases refer to the extension of the technique into the orthogonal directions using additional pairs of beams. We observe that the cooling efficiency improves as the technique is extended beyond 1D, and S/N approaches to zero in a reasonable number of steps in the 2D and 3D cases. We conclude that realistic heating rates from the optical lattice are not a limitation to cooling. Ultimately, the spread in momentum of the condensate, which was not considered in the simulation, sets practical limitations to quasimomentum selectivity on the thermal component of the gas. On the other hand, Pauli blocking [254] and hole heating [255] may limit the lowest temperatures achievable by this method for

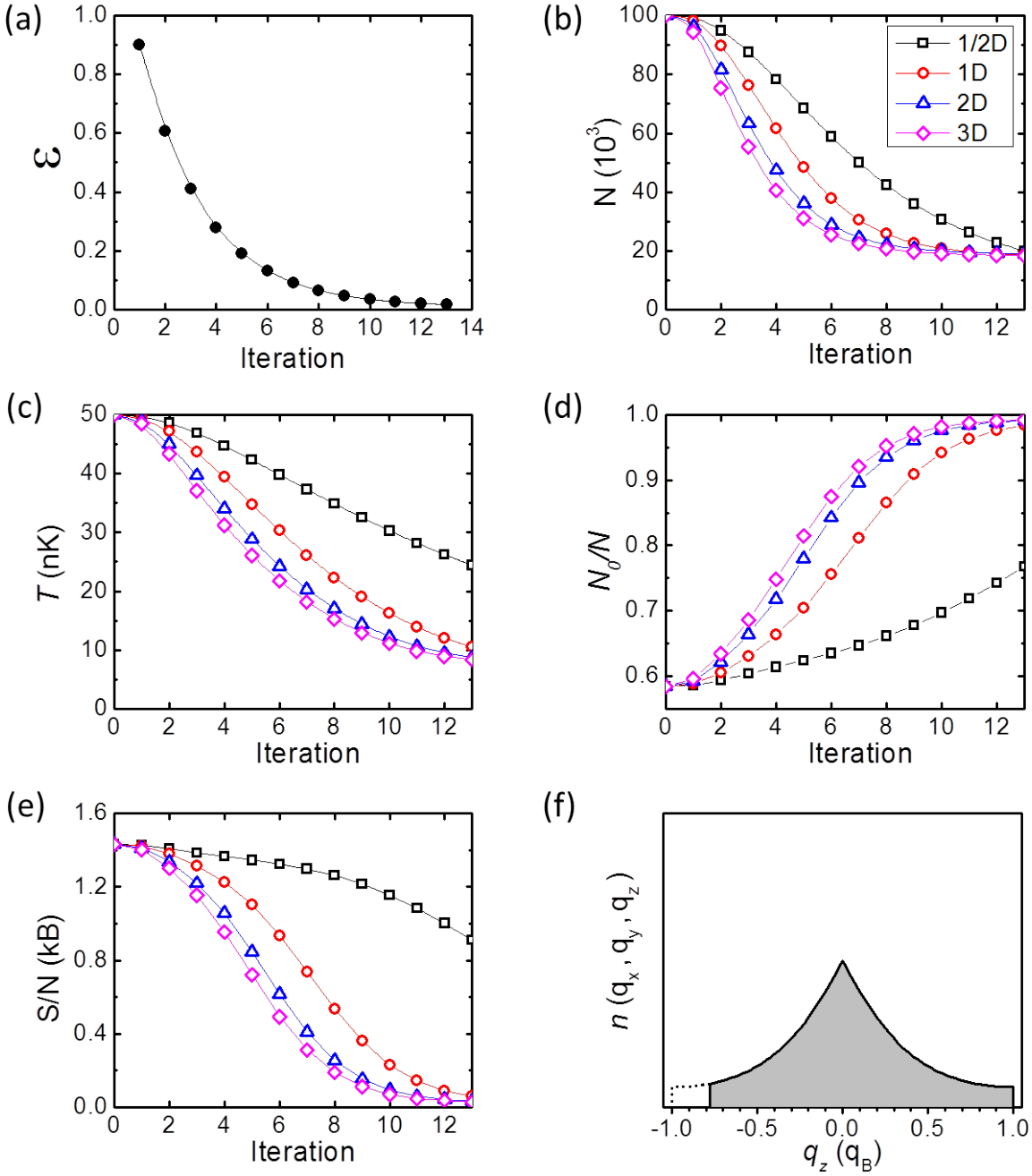

Figure 5.13: Semiclassical simulation of cooling a 3D gas in a cubic lattice ($s = 4$ E_R) using quasimomentum-selective Raman excitation. The quasimomentum distribution is truncated along one (1/2D and 1D), two (2D), and three (3D) lattice directions. (a) Quasimomentum cutoff parameter ε versus cooling iteration. (b) Atom number N. (c) Temperature T. (d) Condensate fraction N/N_0. (e) Entropy per particle S/N. The 1/2D schemes refers to removing atoms from one side of the quasimomentum distribution at a time, as exemplified in (f). For the 1D, 2D, and 3D cases, both sides of the quasimomentum distribution are targeted simultaneously. The cooling parameters have not been optimized.

fermionic atoms. An analysis of strong interaction effects that may also introduce difficulties is beyond the scope of this work.

5.6 Conclusions and Outlook

We have developed a novel cooling technique that selectively removes atoms with large quasimomentum from a lattice-trapped gas. In a proof-of-principle experiment, we have demonstrated for the first time direct cooling of the kinetic energy of a bosonic gas in the Hubbard superfluid regime. The observed reduction in condensate fraction is an evidence for a gas with lower entropy.

Even though thermalization is a key factor for any cooling scheme, it has remained largely unexplored by experiments with strongly correlated systems [256]. In this chapter, we have measured for the first time (to our knowledge) rethermalization rates in a three-dimensional, strongly interacting gas confined in an optical lattice. The rethermalization process observed is extremely fast compared with $\hbar/t$ and $\hbar/U$, and sufficiently rapid to support cooling rates that exceed the heating mechanisms present in the system.

We have compared the experimental equilibration time to a prediction based on FGR with no free parameters. The observed deviation from the FGR calculation at low lattice depths ($s \approx 4$ $\mathrm{E_R}$) highlights the need for a better understanding of dynamics in strongly correlated systems. While density matrix renormalization group approaches can predict dynamics in 1D for short times, there is no method, to our knowledge, for simulating dynamics with controlled uncertainty in this 3D strongly interacting system. Furthermore, exact equilibrium theories, such as quantum Monte Carlo simulations, do not yet have access to the full range of excited states in trapped systems for large N needed to describe our system (quantum Monte Carlo has recently been applied to time evolution in 1D and 2D [257]). Understanding out-of-equilibrium phenomena and dynamics in 3D strongly correlated systems remains an outstanding problem [6].

Numerical simulations based on a non-interacting semiclassical model show that the cooling power and efficiency in our cooling method can be dramatically enhanced by addressing both sides of the first BZ simultaneously along the three lattice directions. The ultimate limit of this cooling technique, as applied to bosons or fermions, must be further investigated.

In the future, this cooling method, which is applicable to any atomic species, could be used on fermionic atoms trapped in optical lattices in order to reach exotic quantum states that may exist at low entropy per particle [60, 62]. Further studies of relaxation in this system may contribute to our understanding of thermalization in closed quantum systems [246] and transport in materials that also display a violation of the MIR bound [249].

Appendix A

Bogoliubov-de-Gennes Equations

In this section, we derive the spectrum of a weakly interacting Bose-Einstein condensate [71]. The time-dependent Gross-Pitaevskii equation is given by [71]

$$\left[-\frac{\hbar^2}{2m}\nabla^2 + V(\mathbf{r}) - \mu + g|\Psi(\mathbf{r},\tau)|^2\right]\Psi(\mathbf{r},\tau) = i\hbar\frac{\partial}{\partial\tau}\Psi(\mathbf{r},\tau) \tag{A.1}$$

where τ is time, μ is the chemical potential, $V(\mathbf{r})$ is a time-independent external potential acting on the system, and $g = 4\pi\hbar^2 a_s/m$ is the interaction parameter. In order to solve Eq. A.1 for $\Psi(\mathbf{r},\tau)$, we consider small deviations from the ground state $\Psi_0(\mathbf{r})$ in the form

$$\Psi(\mathbf{r},\tau) = e^{-i\mu\tau/\hbar}\left[\Psi_0 + u(\mathbf{r})e^{-i\omega\tau} + v^*(\mathbf{r})e^{i\omega\tau}\right]. \tag{A.2}$$

Substitution of Eq. A.2 into Eq. A.1, where we have only kept the linear terms in u and v. Matching the terms with $e^{-i\mu\tau/\hbar}$ in A.1 leads to the equation for the ground state

$$H_0\Psi_0 + g|\Psi_0|^2\Psi_0 = \mu\Psi_0, \tag{A.3}$$

where we have defined the single-particle Hamiltonian $H_0 = -\hbar^2\nabla^2/2m + V(\mathbf{r})$. Analogously, matching the terms with $e^{-i(\mu+\hbar\omega)\tau/\hbar}$ and $e^{-i(\mu-\hbar\omega)\tau/\hbar}$ leads to the Bogoliubov-de-Gennes (BdG) equations

$$\begin{pmatrix} H_0 + 2g|\Psi_0|^2 - \mu & g\Psi_0^2 \\ g\Psi_0^{*2} & H_0 + 2g|\Psi_0|^2 - \mu \end{pmatrix}\begin{pmatrix} u \\ v \end{pmatrix} = \hbar\omega\begin{pmatrix} u \\ -v \end{pmatrix}. \tag{A.4}$$

In the particular case of a uniform Bose gas (i.e., $V(\mathbf{r}) = 0$), the single-particle Hamiltonian H_0 is that of a free particle, $H_0 = \hbar^2k^2/2m$, $\mu = g|\Psi_0|^2$, and the excitations are plane waves

$$u = \frac{u_k}{\sqrt{V}}e^{i\mathbf{k}\cdot\mathbf{r}} \qquad v = \frac{v_k}{\sqrt{V}}e^{i\mathbf{k}\cdot\mathbf{r}} \tag{A.5}$$

where k is wavevector and V is the volume of the system. The BdG equations then reads

$$\begin{pmatrix} \frac{\hbar^2 k^2}{2m} + g|\Psi_0|^2 & g\Psi_0^2 \\ g\Psi_0^{*2} & \frac{\hbar^2 k^2}{2m} + g|\Psi_0|^2 \end{pmatrix} \begin{pmatrix} u \\ v \end{pmatrix} = \hbar\omega \begin{pmatrix} u \\ -v \end{pmatrix}. \tag{A.6}$$

Therefore,

$$\hbar\omega = \sqrt{\varepsilon^0(k)[\varepsilon^0(k) + 2g|\Psi_0|^2]} \tag{A.7}$$

where $\varepsilon^0(k) = \hbar^2 k^2/2m$ is the free-particle energy.

Appendix B

Time-Splitting Spectral Method

In Chapter 3, we have employed the time-splitting spectral method to solve numerically the time-dependent Gross-Pitaevskii equation (GPE)

$$\left[-\frac{\hbar^2}{2m}\nabla^2 + V(\mathbf{r}) - \mu + g|\psi(\mathbf{r},\tau)|^2\right]\psi(\mathbf{r},\tau) = i\hbar\frac{\partial}{\partial\tau}\psi(\mathbf{r},\tau). \tag{B.1}$$

This method is numerically stable and accurate with limited grid points [258].

The time-splitting spectral method propagates the GPE in time through steps $\Delta\tau$, with the linear and nonlinear parts are treated separately, namely

$$i\hbar\frac{\partial}{\partial\tau}\psi(\mathbf{r},\tau) = \left(V(\mathbf{r}) - \mu + g|\psi(\mathbf{r},\tau)|^2\right)\psi(\mathbf{r},\tau) \tag{B.2a}$$

$$i\hbar\frac{\partial}{\partial\tau}\psi(\mathbf{r},\tau) = -\frac{\hbar^2}{2m}\nabla^2\psi(\mathbf{r},\tau), \tag{B.2b}$$

where τ is in the time interval $[\tau_n, \tau_n + \Delta\tau]$. Each equation is solved separately and the final solution is combined using the Strang-splitting formula [259]. If we consider the solutions to Eq. B.2a and Eq. B.2b as $\Phi_{1,\tau}$ and $\Phi_{2,\tau}$, respectively, then

$$\psi(\tau_n + \Delta\tau) = (\Phi_{1,\Delta\tau/2} \circ \Phi_{2,\Delta\tau} \circ \Phi_{1,\Delta\tau/2})(\psi(\tau_n)). \tag{B.3}$$

To solve Eq. B.2a, we first notice that $\partial\psi/\partial\tau \cdot \psi^*$ is a pure imaginary number, and therefore, $\partial|\psi|^2/\partial\tau = 2\,\mathrm{Re}\,(\partial\psi/\partial\tau \cdot \psi^*) = 0$, which implies that $|\psi(\mathbf{r},\tau)|^2$ is time-invariant during each time step. Consequently, U defined as $U = V(\mathbf{r}) - \mu + g|\psi(\mathbf{r},\tau_n)|^2$ is time independent, and therefore, the solution to Eq. B.2a is simply

$$\psi(\mathbf{r},\tau_n + \Delta\tau) = e^{-\frac{i\Delta\tau}{\hbar}U}\psi(\mathbf{r},\tau_n). \tag{B.4}$$

On the other hand, Eq. B.2b can be efficiently solved using the spatial fast Fourier transform $\mathcal{FFT}\{\cdot\}$. We

therefore find

$$\tilde{\psi}(\mathbf{k}, \tau_n + \Delta\tau) = e^{-\frac{i\hbar k^2}{2m}\Delta\tau}\tilde{\psi}(\mathbf{k}, \tau_n), \tag{B.5}$$

where $\tilde{\psi}(\mathbf{k}, \tau) = \mathcal{FFT}\{\psi(\mathbf{r}, \tau)\}$.

Combining Eqs. B.4 and B.5 via Eq. B.3 yields

$$\psi(\mathbf{r}, \tau_n + \Delta\tau) = e^{-\frac{i\Delta\tau}{2\hbar}U}\mathcal{FFT}^{-1}\left\{e^{-\frac{i\hbar k^2\Delta\tau}{2m}}\mathcal{FFT}\left\{e^{-\frac{i\Delta\tau}{2\hbar}U}\psi(\mathbf{r}, \tau_n)\right\}\right\}. \tag{B.6}$$

The time and spatial discretization errors are $\mathcal{O}(\Delta\tau^3)$ and $\mathcal{O}(\Delta L^2)$, respectively, where $\Delta\tau$ is the time step and ΔL is the mesh size [258].

The algorithm defined in B.6 can also be used to find the ground state of the GPE under a Wick rotation on the time coordinate, i.e., $\tau \to -i\tau'$.

Appendix C

Two-Level System

Given a two-level atomic system

$$\hat{H}_0 = \hbar\omega_g|g\rangle\langle g| + \hbar\omega_e|e\rangle\langle e|, \tag{C.1}$$

where $|g\rangle$ and $|e\rangle$ are the ground and excited states respectively, and an electric field $\mathbf{E} = \mathbf{E}_0 \cos\omega\tau$ that induces on the atom a dipole moment $\mathbf{d} = -e\mathbf{r}$. The oscillatory electric field couples both energy levels through the interaction Hamiltonian

$$\hat{H}_1 = \hbar\Omega \cos\omega\tau\, |e\rangle\langle g| + \hbar\Omega^* \cos\omega\tau\, |g\rangle\langle e| \tag{C.2}$$

where

$$\Omega = -\langle e|\hat{\mathbf{d}} \cdot \mathbf{E}_0|g\rangle/\hbar \tag{C.3}$$

is the Rabi rate. Under the ansatz $|\psi\rangle = c_g(\tau)|g\rangle + c_e(\tau)|e\rangle$, the Schrödinger equation reads

$$i\hbar\frac{d}{d\tau}\begin{pmatrix} c_g \\ c_e \end{pmatrix} = \hbar\begin{pmatrix} \omega_g & \Omega^*\cos\omega\tau \\ \Omega\cos\omega\tau & \omega_e \end{pmatrix}\begin{pmatrix} c_g \\ c_e \end{pmatrix} \tag{C.4}$$

It is evident that the Hamiltonian on the right hand side is equivalent to

$$H = \frac{\hbar}{2}\begin{pmatrix} \bar{\omega} & 0 \\ 0 & \bar{\omega} \end{pmatrix} + \frac{\hbar}{2}\begin{pmatrix} -\omega_0 & 2\Omega^*\cos\omega\tau \\ 2\Omega\cos\omega\tau & \omega_0 \end{pmatrix}, \tag{C.5}$$

where $\omega_0 = \omega_e - \omega_g$ and $\bar{\omega} = (\omega_g + \omega_e)/2$. The diagonal matrix corresponds to an overall shift in energy and it will be ignore in the following calculation.

To eliminate the time dependence in the matrix, we switch to a co-rotating frame through the unitary transformation $|\tilde{\psi}\rangle = U^\dagger|\psi\rangle$, where

$$U = \begin{pmatrix} e^{i\omega\tau/2} & 0 \\ 0 & e^{-i\omega\tau/2} \end{pmatrix}, \tag{C.6}$$

where the Hamiltonian transforms as $\tilde{H} = U^\dagger H U - i\hbar U^\dagger \partial U/\partial\tau$. The new Schrödinger equation reads

$$i\hbar\frac{d}{d\tau}\begin{pmatrix}\tilde{c}_g\\ \tilde{c}_e\end{pmatrix} = \frac{\hbar}{2}\begin{pmatrix}\delta & \Omega^*\left(1+e^{-i2\omega\tau}\right)\\ \Omega\left(1+e^{i2\omega\tau}\right) & -\delta\end{pmatrix}\begin{pmatrix}\tilde{c}_g\\ \tilde{c}_e\end{pmatrix} \tag{C.7}$$

where $\delta = \omega - \omega_0$.

The time evolution of Eq. C.7 has three different time scales: $|\delta|$, 2ω, and $|\Omega|$, and usually 2ω is much larger than $|\delta|$ and $|\Omega|$. Consequently, the fast oscillating term in Eq. C.7 can be averaged out under a rotating-wave approximation (RWA) [117], which results in

$$i\hbar\frac{d}{d\tau}\begin{pmatrix}\tilde{c}_g\\ \tilde{c}_e\end{pmatrix} = \frac{\hbar}{2}\begin{pmatrix}\delta & \Omega^*\\ \Omega & -\delta\end{pmatrix}\begin{pmatrix}\tilde{c}_g\\ \tilde{c}_e\end{pmatrix}. \tag{C.8}$$

Alternative approaches that include the counter-rotating terms are presented in Ref. [71, 260, 261].

The eigenenergies of Eq. C.8 are

$$E_\pm = \pm\frac{\hbar}{2}\sqrt{\delta^2 + |\Omega|^2}, \tag{C.9}$$

and the respective (unnormalized) eigenvectors are

$$v_\pm = \begin{pmatrix}\delta \pm \sqrt{|\Omega|^2+\delta^2}\\ \Omega\end{pmatrix}. \tag{C.10}$$

If we assume that the system is initially in the ground state, i.e., $c_g(0) = 1$ and $c_e(0) = 0$, the explicit time evolution of the system is

$$\begin{pmatrix}\tilde{c}_g\\ \tilde{c}_e\end{pmatrix} = \begin{pmatrix}\cos\left(\sqrt{|\Omega|^2+\delta^2}\frac{\tau}{2}\right) - \frac{i\delta}{\sqrt{|\Omega|^2+\delta^2}}\sin\left(\sqrt{|\Omega|^2+\delta^2}\frac{\tau}{2}\right)\\ -\frac{i\Omega}{\sqrt{|\Omega|^2+\delta^2}}\sin\left(\sqrt{|\Omega|^2+\delta^2}\frac{\tau}{2}\right)\end{pmatrix}, \tag{C.11}$$

and the wavefunction evolves in time as

$$|\psi\rangle = U|\tilde{\psi}\rangle = \tilde{c}_g(\tau)e^{i\omega\tau/2}|g\rangle + \tilde{c}_e(\tau)e^{-i\omega\tau/2}|e\rangle. \tag{C.12}$$

Appendix D

Semiclassical Thermodynamics

We present details of the thermodynamic model used in Chapters 3 and 4 for estimating the temperature, entropy, and energy of a non-interacting gas trapped in a lattice potential. We first derive the tight-binding energy of a single particle in the lattice. We then calculate the quasimomentum distribution of a non-interacting atomic ensemble and we use it as a starting point for deriving thermodynamic quantities. Semiclassical thermodynamics in optical lattices have previously been used for studying thermometry and bandmapping in ultracold gases [77, 85]. A thorough discussion on the validity of the tigh-binding model and the semiclassical approximation can be found in Ref. [72]. Exact quantum Monte Carlos simulations for a bosonic gas in the superfluid regime of the Bose-Hubbard model have been performed in Ref. [262, 263].

D.1 Tight-Binding Approximation

The Hamiltonian of a particle with mass m confined in a simple cubic lattice potential with lattice spacing d and an overall harmonic potential with frequency ω is

$$\hat{H} = \frac{\hat{\mathbf{p}}^2}{2m} + s \sum_{i=x,y,z} \cos^2\left(\pi \hat{x}_i/d\right) + \frac{1}{2} m\omega^2 \sum_{i=x,y,z} \hat{x}_i^2, \tag{D.1}$$

where s is the lattice potential depth. Eq. D.1 is diagonalizable using Bloch wavefunctions in the form

$$\phi_q(x) = \frac{1}{\sqrt{N_s}} \sum_j e^{\frac{i}{\hbar} qjd} w(x - jd), \tag{D.2}$$

where q is quasimomentum, N_s is the number of lattice sites and $w(x)$ represents a localized Wannier function about the origin. In 1D we obtain

$$\begin{aligned} \epsilon(q,x) &= \int dx'\, \phi_q^*(x') H_0(x') \phi_q(x') + \frac{1}{2} m\omega^2 x^2 \\ &= \frac{1}{N_s} \sum_{j,j'} e^{\frac{i}{\hbar} q(j-j')d} \int dx'\, w^*(x' - jd) H_0(x') w(x' - j'd) + \frac{1}{2} m\omega^2 x^2, \end{aligned} \tag{D.3}$$

where $H_0(x) = -(\hbar^2/2m)\nabla^2 + s\cos^2(\pi x/d)$ is periodic in x with period d. In the tight-binding approximation, the sum over j' is truncated to the nearest-neighbor terms, i.e., $j' = j, j \pm 1$. In practice, this is a good approximation once the lattice depth $s \gtrsim 4\ \mathrm{E_R}$ (see Chapter 2.3 in Ref. [72], for example).

If we define the offset energy as

$$\epsilon_0 = \int dx'\, w^*(x') H_0(x') w(x') \tag{D.4}$$

and the tunneling energy as

$$t = -\int dx'\, w^*(x') H_0(x') w(x' - d), \tag{D.5}$$

then we obtain

$$\begin{aligned}\epsilon(q, x) &= \frac{1}{N_s}\sum_j \left(\epsilon_0 - te^{-\frac{i}{\hbar}qd} - te^{\frac{i}{\hbar}qd}\right) + \frac{1}{2}m\omega^2 x^2 \\ &= 2t\left[1 - \cos\left(qd/\hbar\right)\right] + \frac{1}{2}m\omega^2 x^2,\end{aligned} \tag{D.6}$$

where, without loss of generality, we have chosen $\epsilon_0 = 2t$. Finally, we extend the result to a cubic lattice as

$$\epsilon(q_x, q_y, q_z, x, y, z) = 2t \sum_{i=x,y,z} \left[1 - \cos\left(\pi q_i/q_B\right)\right] + \frac{1}{2}m\omega^2 \sum_{i=x,y,x} x_i^2, \tag{D.7}$$

where q_i is quasimomentum in the lattice direction i and $q_B = \hbar\pi/d$.

D.2 Quasimomentum distribution

In this section, the quasimomentum distribution of the gas is derived using the grand canonical ensemble with the eigenenergies found in Eq. D.7. To evaluate sums over the quantum states (i.e., quasimomentum and position), we use a semiclassical approximation in which states are "coarse-grained" and sums over states are approximated by integrals [71]. In order for the semiclassical approximation to remain valid, the quantum states have to be densely populated. Such condition is satisfied in the context of a gas in a harmonic-plus-lattice confinement when $k_B T \gg \hbar^2\pi^2/(2mL^2)$ (for quasimomentum) and $k_B T \gg \hbar\omega$ (for position) or, equivalently, when the thermal wavelength $\lambda_T = h/\sqrt{2\pi m k_B T}$ is much smaller than the linear size of the system L and the length scale over which the trapping potential varies significantly, $a = \sqrt{\hbar/(m\omega)}$. In our experiments, λ_T is typically a few hundred of nm, while a and L are tens of μm.

The quasimomentum distribution of a non-interacting gas in a harmonic-plus-cubic-lattice potential is

calculated as

$$n(q_x,q_y,q_z) = \frac{1}{h^3}\int d^3r\,\frac{1}{z^{-1}e^{\beta E(q_x,q_y,q_z,x,y,z)}\mp 1} = \frac{4\pi}{h^3}\int_0^\infty dr\,r^2\frac{1}{z^{-1}e^{2\beta t\sum_i[1-\cos(\pi q_i/q_B)]}e^{\frac{1}{2}\beta m\omega^2 r^2}\mp 1}, \tag{D.8}$$

where $z=e^{\beta\mu}$ is fugacity, $\beta=(k_BT)^{-1}$ and the $-/+$ sign corresponds to bosons/ fermions. After making the change of variables $u=\beta m\omega^2 r^2/2$, the quasimomentum distribution becomes

$$n(q_x,q_y,q_z) = \frac{2\pi}{h^3}\left(\frac{2}{\beta m\omega^2}\right)^{3/2}\int_0^\infty du\,\frac{\sqrt{u}}{z^{-1}e^{2\beta t\sum_i[1-\cos(\pi q_i/q_B)]}e^u\mp 1}. \tag{D.9}$$

The integral is equal to $\pm 2^{-1}\sqrt{\pi}\,\mathrm{Li}_{3/2}(\pm ze^{-2\beta t\sum_i[1-\cos(\pi q_i/q_B)]})$, where $\mathrm{Li}_{3/2}$ is the polylogarithm function[1]. Therefore,

$$n(q_x,q_y,q_z) = \pm\frac{1}{\hbar^3(2\pi\beta m\omega^2)^{3/2}}\mathrm{Li}_{3/2}(\pm ze^{-2\beta t\sum_i[1-\cos(\pi q_i/q_B)]}) = \pm\left(\frac{a^2}{\hbar\lambda_T}\right)^3\mathrm{Li}_{3/2}(\pm ze^{-2\beta t\sum_i[1-\cos(\pi q_i/q_B)]}). \tag{D.10}$$

D.3 Non-condensed atom number

Integration of Eq. D.10 over the first Brillouin zone results in the total atom number of the non-condensed gas (the integral does not properly take into account the condensate), namely

$$N = \pm\left(\frac{a^2}{\hbar\lambda_T}\right)^3\int d^3q\,\mathrm{Li}_{3/2}(\pm ze^{-2\beta t\sum_i[1-\cos(\pi q_i/q_B)]}). \tag{D.11}$$

The polylogarithm function can be expressed as an infinite series[2], which leads to

$$N = \pm\left(\frac{a^2}{\hbar\lambda_T}\right)^3\sum_{j=1}^\infty\frac{(\pm z)^j e^{-6\beta tj}}{j^{3/2}}\left(\int_{-q_B}^{q_B}dq\,e^{2\beta tj\cos(\pi q/q_B)}\right)^3. \tag{D.12}$$

[1] $\mathrm{Li}_s(\pm z)=\pm\frac{1}{\Gamma(s)}\int_0^\infty du\,\frac{u^{s-1}}{z^{-1}e^u\mp 1}$

[2] $\mathrm{Li}_s(z)=\sum_{j=1}^\infty\frac{z^j}{j^s}$

Under the change of variables $\theta = \pi q/q_B$, the integral between parentheses becomes $2q_B/\pi \int_0^\pi d\theta\, e^{2\beta t j\cos\theta}$ and it can be expressed in terms of modified Bessel functions of the first kind[3]. We find

$$N = \pm 8\pi^3 \left(\frac{a^2}{\lambda_T\, d}\right)^3 \sum_{j=1}^{\infty} \frac{(\pm z)^j e^{-6\beta t j} I_0^3(2\beta t j)}{j^{3/2}}. \tag{D.13}$$

D.4 Kinetic and Potential Energy

The average potential energy is given by

$$\begin{aligned} V &= \frac{2\pi m\omega^2}{h^3} \int d^3q \int_0^\infty dr\, r^4 \frac{1}{z^{-1}e^{2\beta t\sum_i [1-\cos(\pi q_i/q_B)]} e^{\beta m\omega^2 r^2/2} \mp 1} \\ &= \frac{\pi m\omega^2}{h^3} \left(\frac{2}{\beta m\omega^2}\right)^{5/2} \int d^3q \int_0^\infty du\, \frac{u^{3/2}}{z^{-1}e^{2\beta t\sum_i [1-\cos(\pi q_i/q_B)]} e^{u} \mp 1} \\ &= \pm \frac{6(2\pi)^{3/2} m\omega^2}{4h^3} \left(\frac{1}{\beta m\omega^2}\right)^{5/2} \int d^3q\, \mathrm{Li}_{5/2}(\pm z e^{-2\beta t\sum_i [1-\cos(\pi q_i/q_B)]}) \\ &= \pm \frac{12\pi^3}{\beta} \left(\frac{a^2}{\lambda_T\, d}\right)^3 \sum_{j=1}^{\infty} \frac{(\pm z)^j e^{-6\beta t j} I_0^3(2\beta t j)}{j^{5/2}}. \end{aligned} \tag{D.14}$$

On the other hand, the average kinetic energy is given by

$$\begin{aligned} K &= \int d^3q\, 2t \sum_{i=x,y,z} [1-\cos(\pi q_i/q_B)]\, n(q_x,q_y,q_z) \\ &= 6tN - 6t \int dq^3\, \cos(\pi q_x/q_B)\, n(q_x,q_y,q_z), \end{aligned} \tag{D.15}$$

where the last integral is equal to

$$\begin{aligned} \int dq^3\, \cos(\pi q_x/q_B)\, n(q_x,q_y,q_z) \quad &\pm \frac{1}{(2\pi\beta m\omega^2)^{3/2}\hbar^3} \int d^3q\, \cos(\pi q_x/q_B)\, \mathrm{Li}_{3/2}(\pm z e^{-2\beta t\sum_i [1-\cos(\pi q_i/q_B)]}) \\ &= \pm \frac{1}{(2\pi\beta m\omega^2)^{3/2}\hbar^3} \sum_{j=1}^{\infty} \frac{(\pm z)^j e^{-6\beta t j}}{j^{3/2}} \left(\int dq\, e^{2\beta t j\cos(\pi q_i/q_B)}\right)^2 \times \\ &\quad \times \int dq\, \cos(\pi q/q_B)\, e^{2\beta t j\cos(\pi q/q_B)} \\ &= \pm \frac{8q_B^3}{(2\pi\beta m\omega)^{3/2}\hbar^3} \sum_{j=1}^{\infty} \frac{(\pm z)^j e^{-6\beta t j} I_1(2\beta t j) I_0^2(2\beta t j)}{j^{3/2}}. \end{aligned} \tag{D.16}$$

Therefore,

$$\mathrm{K} = \pm 48\, t \left(\frac{a^2}{\lambda_T\, d}\right)^3 \sum_{j=1}^{\infty} \frac{(\pm z)^j e^{-6\beta t j} I_0^2(2\beta t j)\, [I_0(2\beta t j) - I_1(2\beta t j)]}{j^{3/2}}. \tag{D.17}$$

[3] $I_j(z) = \frac{1}{\pi}\int_0^\pi d\theta\, e^{z\cos\theta}\cos j\theta$

D.5 Grand potential

The grand potential is

$$\begin{aligned}\Omega &= \pm\frac{1}{\beta h^3}\int d^3r\int d^3q\,\ln\left(1\mp ze^{-\beta E(q_x,q_y,q_z,x,y,z)}\right)\\ &= \pm\frac{4\pi}{\beta h^3}\int_0^\infty dr\,r^2\int d^3q\,\ln\left(1\mp ze^{-2\beta t\sum_i[1-\cos(\pi q_i/q_B)]-\frac{1}{2}\beta m\omega^2 r^2}\right).\end{aligned} \tag{D.18}$$

Expansion of the natural logarithm as an infinite series[4] leads to

$$\Omega = \mp\frac{4\pi}{\beta h^3}\sum_{j=1}^{\infty}\frac{(\pm z)^j e^{-6\beta tj}}{j}\int_0^\infty dr\,r^2 e^{-\frac{j\beta m\omega^2 r^2}{2}}\int d^3q\,e^{2\beta tj\sum_i\cos(\pi q_i/q_B)}. \tag{D.19}$$

The first and second integrals are equal to $\sqrt{2\pi}(2(j\beta m\omega^2)^{3/2})^{-1}$ and $8q_B^3 I_0^3(2\beta tj)$, respectively. Therefore,

$$\Omega = \mp\frac{8\pi^3}{\beta}\left(\frac{a^2}{\lambda_T\,d}\right)^3\sum_{j=1}^{\infty}\frac{(\pm z)^j e^{-6\beta tj}I_0^3(2\beta tj)}{j^{5/2}}. \tag{D.20}$$

D.6 Entropy

In the grand canonical ensemble, the gas entropy is expressed by the formula

$$S = -\frac{\partial\Omega}{\partial T} = \frac{E-\mu N-\Omega}{T}, \tag{D.21}$$

where N is the total particle number given by Eq. D.13, Ω is the grand potential given by Eq. D.20, and $E = K + V$ is the total energy with K and V given by Eq. D.17 and Eq. D.14, respectively.

[4] $\ln(1+x) = \sum_{j=1}^{\infty}\frac{(-1)^{j+1}x^j}{j}$ for $-1 < x \leq 1$

Appendix E

Quasimomentum Distribution: Projection onto the Imaging Plane

In Chapter 5, we have fit a model of the quasimomentum distribution of the lattice gas projected onto the imaging plane to the TOF absorption images. In the present Appendix, we derive an analytical expression for this model.

The quasimomentum distribution of a 3D non-interacting bosonic gas confined in a 3D cubic lattice potential is (see Appendix D)

$$n\left(q_x, q_y, q_z\right) \propto \mathrm{Li}_{3/2}\left(z e^{-2\beta t \sum_{i=x,y,z}(1-\cos(\pi q_i/q_B))}\right), \tag{E.1}$$

where Li is the polylogarithm function[1], z is fugacity, t is the tight-binding tunneling energy, $\beta = 1/k_B T$ $q_B = \hbar\pi/d$, d is the lattice spacing, and q_x, q_y, q_z are quasimomenta in the lattice directions $\hat{x}, \hat{y}, \hat{z}$, respectively. In our imaging system, none of the three lattice directions are parallel to the imaging axis. In order to project $n(q_x, q_y, q_z)$ onto the imaging plane, we define the coordinates q_1, q_2, and q_3 in the basis $\{\hat{x}_1, \hat{x}_2, \hat{x}_3\}$ defined in Section 1.1.1, where $\hat{x}_1$ is parallel to the imaging axis, as shown in Figs. 1.2, 1.5 and E.1. Both sets of coordinates are mutually related via the transformation

$$\begin{aligned} q_x &= -\frac{q_1}{\sqrt{2}} - \frac{q_2}{2} + \frac{q_3}{2} \\ q_y &= \frac{q_1}{\sqrt{2}} - \frac{q_2}{2} + \frac{q_3}{2} \\ q_z &= \frac{q_2}{\sqrt{2}} + \frac{q_3}{\sqrt{2}} \end{aligned} \tag{E.2}$$

Eqs. E.2 are determined by the spatial configuration of the lattice beams and the imaging system in our apparatus.

Projection of the gas onto the imaging plane is computed as the column integration of Eq. E.1 along $\hat{x}_1$, namely

$$n\left(q_2, q_3\right) = \int dq_1\, n\left(q_x, q_y, q_z\right) \tag{E.3}$$

[1] The polylogarithm function is defined as $\mathrm{Li}_s\left(z\right) = \sum_{j=1}^{\infty} \frac{z^j}{j^s}$.

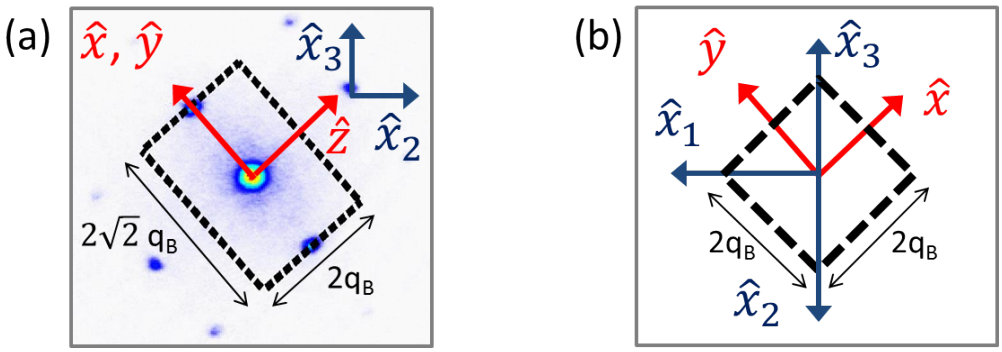

Figure E.1: Spatial configuration of the lattice wavevectors $\hat{x}, \hat{y}, \hat{z}$ and the coordinates $\hat{x}_1, \hat{x}_2, \hat{x}_3$ defined in Section 1.1.1 (we follow the right-hand rule convention). The first BZ in both figures is delimited by the dashed lines. (a) The first BZ as seen through the camera. The dots in the image indicate the reciprocal lattice. (b) The first BZ viewed from a different angle. Projection of the gas onto the imaging plane occurs along $\hat{x}_1$.

with q_x, q_y, and q_z given by Eq. E.2.

The series expansion of the polylogarithm function leads to

$$n\left(q_2, q_3\right) \propto \sum_{j=1}^{\infty} \frac{e^{-2j\beta t[3-\cos(\pi q_z/q_B)]} z^j}{j^{3/2}} \int dq_1\, e^{2j\beta t[\cos(\pi q_x/q_B)+\cos(\pi q_y/q_B)]}, \tag{E.4}$$

where the integral can be written as[2]

$$\mathcal{I} = \int dq_1\, e^{4j\beta t \cos\left(\frac{\pi}{2}\frac{q_3-q_2}{q_B}\right)\cos\left(\frac{\pi}{\sqrt{2}}\frac{q_1}{q_B}\right)}. \tag{E.5}$$

We need to express the limits of integration of $\mathcal{I}$ in terms of q_2 and q_3. The upper limit is set by the two planes $q_x = -q_B$ and $q_y = q_B$, as shown in (b) of Fig. E.1. Substitution into Eq. E.2 leads to

$$q_x = -q_B \implies q_1 = \sqrt{2}q_B - \frac{q_2}{\sqrt{2}} + \frac{q_3}{\sqrt{2}} \tag{E.6}$$

$$q_y = +q_B \implies q_1 = \sqrt{2}q_B + \frac{q_2}{\sqrt{2}} - \frac{q_3}{\sqrt{2}} \tag{E.7}$$

When $q_3 \geq q_2$, the upper limit of integration is set by Eq. E.7 (dashed line in the bottom-left of (b) of Fig. E.1). Analogously, when $q_3 \leq q_2$, the upper limit is set by Eq. E.6 (dashed line in the top-left of (b) of Fig. E.1). Both cases can be combined as $q_1^* = \sqrt{2}q_B - |q_3 - q_2|/\sqrt{2}$. On the other hand, because of

[2] We have used the identity $\cos A + \cos B = 2\cos\frac{A+B}{2}\cos\frac{A-B}{2}$.

symmetry, the lower limit of integration of Eq. E.5 is $-q_1^*$. Eq. E.5 therefore becomes

$$\mathcal{I} = \int_{-q_1^*}^{q_1^*} dq_1 \, e^{4j\beta t \cos\left(\frac{\pi}{2}\frac{q_3-q_2}{q_B}\right)\cos\left(\frac{\pi}{\sqrt{2}}\frac{q_1}{q_B}\right)}. \tag{E.8}$$

Under the change of variables $\theta = \pi q_1/(\sqrt{2}q_B)$ and the definition of two new variables: $a = \pi|q_3 - q_2|/(2q_B)$ and $\alpha_j = 4j\beta t \cos a$, the integral is equal to

$$\begin{aligned}
\mathcal{I} &\propto \int_0^{\pi-a} d\theta \, e^{\alpha_j \cos\theta} \\
&= \int_0^{\pi-a} d\theta \, \left[I_0(\alpha_j) + 2\sum_{l=0}^{\infty} I_l(\alpha_j)\cos(l\theta) \right] \\
&= (\pi - a) I_0(\alpha_j) + 2\sum_{l=0}^{\infty} I_l(\alpha_j) \frac{\sin l(\pi - a)}{l},
\end{aligned} \tag{E.9}$$

where we have expressed the exponential function in terms of modified Bessel functions of the first kind[3]. Finally, substitution of Eq. E.9 into Eq. E.4 results in

$$n\left(q_2, q_3\right) = A\sum_{j=1}^{\infty} \frac{e^{-2j\beta t(3-\cos b)} z^j}{j^{3/2}} \cdot \left[(\pi - a) I_0(\alpha_j) + 2\sum_{l=1}^{\infty} I_l(\alpha_j) \frac{\sin l(\pi - a)}{l} \right] \tag{E.10}$$

where $a = \pi|q_2 - q_3|/(2q_B)$, $b = \pi(q_2 + q_3)/(\sqrt{2}q_B)$, $\alpha_j = 4j\beta t \cos a$,and A is a fitting constant.

[3] $e^{z\cos\theta} = I_0(z) + 2\sum_{l=0}^{\infty} I_l(z)\cos(l\theta)$

Appendix F

Site-Decoupled Mean-Field Theory

Throughout this thesis, we have calculated a series of observables in the Bose-Hubbard model (Eq. 1.12) using a site-decoupled mean-field calculation. More details on this topic can be found in Ref. [75,221,264,265] and references therein.

The creation and annihilation operators in the Bose-Hubbard Hamiltonian can be separated into a mean field plus a small deviation, namely, $\hat{a}_j = \langle \hat{a}_j \rangle + (\hat{a}_j - \langle \hat{a}_j \rangle)$ and $\hat{a}_i^\dagger = \langle \hat{a}_i^\dagger \rangle + (\hat{a}_i^\dagger - \langle \hat{a}_i^\dagger \rangle)$, from which the number operator $\hat{n}_i = \hat{a}_i^\dagger \hat{a}_j$ can be expressed as

$$\hat{a}_i^\dagger \hat{a}_j = \langle \hat{a}_j \rangle \hat{a}_i^\dagger + \langle \hat{a}_i^\dagger \rangle \hat{a}_j - \langle \hat{a}_i^\dagger \rangle \langle \hat{a}_j \rangle + (\hat{a}_i^\dagger - \langle \hat{a}_i^\dagger \rangle)(\hat{a}_j - \langle \hat{a}_j \rangle). \tag{F.1}$$

The last term in Eq. F.1 is neglected under a mean-field approximation, since it represents fluctuations about a mean field. Consequently, the Bose-Hubbard Hamiltonian can be decoupled into sub-Hamiltonians at each lattice site i in the form

$$\hat{H}_i^{\mathrm{MF}} = -t\mathbb{z}\left(\psi_i\, \hat{a}_i^\dagger + \psi_i^*\, \hat{a}_i - |\psi_i|^2\right) + \frac{U}{2}\hat{n}_i\,(\hat{n}_i - 1) - \tilde{\mu}_i \hat{n}_i, \tag{F.2}$$

where $\mathbb{z}$ is the coordination number of the lattice ($\mathbb{z} = 6$ for a cubic lattice),

$$\tilde{\mu}_i = \mu - \varepsilon_i \tag{F.3}$$

is the local chemical potential under the LDA, and $\psi_i = \langle \hat{a}_i \rangle$ is the expected value of the annihilation operator, which is interpreted as the order parameter of the system [266].

In the occupation-number basis $\{|n\rangle\}_{n=0}^{\infty}$, the system of equations in Eq. F.2 forms a tridiagonal matrix, where the diagonal terms is

$$\langle m|H_i^{\mathrm{MF}}|n\rangle = \left(\frac{U}{2}n(n-1) - \tilde{\mu}_i n + t\mathbb{z}|\psi_i|^2\right)\delta_{m,n} - t\mathbb{z}\psi_i\sqrt{n+1}\,\delta_{m,n+1} - t\mathbb{z}\psi_i^*\sqrt{n}\,\delta_{m,n-1} \tag{F.4}$$

In practice, the basis is truncated for a large enough occupation number n.

The solution to Eq. F.4 leads to a set of energies $\{\epsilon_\nu\}_\nu$ and eigenstates $\{|\phi_\nu\rangle\}_\nu$ associated with each lattice site i. For sake of clarity, the lattice-site index i is omitted from ϵ_ν and $|\phi_\nu\rangle$. Each eigenvector is expressed as a linear combination of number states, namely, $|\phi_\nu\rangle = \sum_{n=0}^{\infty} f_\nu^n |n\rangle$, where ν indexes the energies and eigenstates.

The order parameter is obtained by calculating the ensemble average self-consistently. The canonical partition function is used as opposed to the grand canonical because the number of particles in each eigenstate is fixed. The order parameter is given by

$$\begin{aligned}\psi(\tilde{\mu}_i, T) &= \langle \hat{a}_i \rangle \\ &= \frac{1}{Z} \operatorname{tr}\left(\sum_\nu e^{-\beta\epsilon_\nu} |\phi_\nu\rangle\langle\phi_\nu| \hat{a}_i \right) \\ &= \frac{1}{Z} \sum_\nu e^{-\beta\epsilon_\nu} \sum_n f_\nu^{*n-1} f_\nu^n \sqrt{n},\end{aligned} \tag{F.5}$$

where $Z(\tilde{\mu}_i, T) = \sum_\nu e^{-\beta\epsilon_\nu}$ is the canonical partition function.

The average occupation number at each lattice site i is

$$\begin{aligned}n(\tilde{\mu}_i, T) &= \langle \hat{n}_i \rangle \\ &= \frac{1}{Z} \operatorname{tr}\left(\sum_\nu e^{-\beta\epsilon_\nu} |\phi_\nu\rangle\langle\phi_\nu| \hat{a}_i^\dagger \hat{a}_i \right) \\ &= \frac{1}{Z} \sum_\nu e^{-\beta\epsilon_\nu} \sum_n n \cdot |f_\nu^n|^2,\end{aligned} \tag{F.6}$$

and the energy is

$$\epsilon(\tilde{\mu}_i, T) = \frac{1}{Z} \sum_\nu \epsilon_\nu e^{-\beta\epsilon_\nu}. \tag{F.7}$$

The entropy is determined from the Helmholtz free energy $F = -k_B T \log Z$ via $F = E - TS$, namely

$$s(\tilde{\mu}_i, T) = \frac{\epsilon(\tilde{\mu}_i, T)}{T} + k_B \log Z(\tilde{\mu}_i, T) \tag{F.8}$$

When an three-dimensional isotropic harmonic confinement is present, the local chemical potential in Eq. F.3 takes the particular form $\tilde{\mu}_i = \mu - \frac{1}{2} m\omega^2 r^2$, where ω is the trap frequency. The total gas entropy and atom number results from integrating the number and entropy densities $n(\tilde{\mu}_i, T)/d^3$ and $s(\tilde{\mu}_i, T)/d^3$

across the parabolic potential, namely,

$$N(\mu, T) = \frac{4\pi}{d^3} \int dr\, r^2 n(\mu - \frac{1}{2} m\omega^2 r^2, T) \tag{F.9}$$

and

$$S(\mu, T) = \frac{4\pi}{d^3} \int dr\, r^2 s(\mu - \frac{1}{2} m\omega^2 r^2, T), \tag{F.10}$$

where d is the lattice spacing. Furthermore, the total particle number in the condensate is given by

$$N_0(\mu, T) = \frac{4\pi}{d^3} \int dr\, r^2 \left| \psi(\mu - \frac{1}{2} m\omega^2 r^2, T) \right|^2, \tag{F.11}$$

and therefore, the condensate fraction is $N_0(\mu, T)/N(\mu, T)$.

Appendix G

Quasimomentum Relaxation via FGR

We present the derivation of the predicted quasimomentum relaxation rate introduced in Section 5.4.3.

We consider a 3D thermal gas confined in a uniform cubic lattice potential (i.e., without a harmonic confinement). After removing all the atoms with $\mathbf{q} = \mathbf{0}$ from the gas, we expect an exponential relaxation of the quasimomentum distribution $\mathbb{n}_0$ to the equilibrium value $\mathbb{n}_0^{\mathrm{eq}} = e^{-\beta(\epsilon_{\mathbf{0}}-\mu)}$ (with $\beta = 1/k_B T$). In other words, we expect $\mathbb{n}_0$ to relax as $\mathbb{n}_0(\tau) = \mathbb{n}_0^{\mathrm{eq}}(1 - e^{-\tau/\tau_0}) \approx \mathbb{n}_0^{\mathrm{eq}}\,\tau/\tau_0$. Therefore, the relaxation time τ_0 is determined by the formula

$$\frac{1}{\tau_0} = \frac{1}{\mathbb{n}_0^{\mathrm{eq}}}\frac{\partial \mathbb{n}_0}{\partial \tau}, \tag{G.1}$$

where $\partial \mathbb{n}_0/\partial\tau$ is given by Fermi's golden rule

$$\frac{\partial \mathbb{n}_0}{\partial \tau} = \sum_{\mathbf{q}_1\mathbf{q}_2\mathbf{q}_3} |\langle \mathbf{q}_3, \mathbf{0}|\hat{H}_{\mathrm{int}}|\mathbf{q}_1, \mathbf{q}_2\rangle|^2 \mathbb{n}_{\mathbf{q}_1}\,\mathbb{n}_{\mathbf{q}_2}(1+\mathbb{n}_{\mathbf{q}_3})(1+\mathbb{n}_0)\delta(\epsilon_{\mathbf{q}_1} + \epsilon_{\mathbf{q}_2} - \epsilon_{\mathbf{q}_3} - \epsilon_{\mathbf{0}}). \tag{G.2}$$

In the subsequent calculations, we will ignore quantum statistics by considering a classical gas with $\mathbb{n}_{\mathbf{q}_1}$, $\mathbb{n}_{\mathbf{q}_2}$, $\mathbb{n}_{\mathbf{q}_3}$, $\mathbb{n}_0 \ll 1$. The interaction Hamiltonian $\hat{H}_{\mathrm{int}}$ is given by

$$\hat{H}_{\mathrm{int}} = \frac{U}{2}\sum_j \hat{a}_j^\dagger \hat{a}_j^\dagger \hat{a}_j \hat{a}_j, \tag{G.3}$$

where U is the Hubbard interaction energy, and $\hat{a}_j^\dagger$ ($\hat{a}_j$) creates (annihilates) a particle at the lattice site j.

In order to determine $\langle \mathbf{q}_3, \mathbf{0}|\hat{H}_{\mathrm{int}}|\mathbf{q}_1, \mathbf{q}_2\rangle$, we construct the initial and final states as

$$|\mathbf{q}_1, \mathbf{q}_2\rangle = \hat{a}_{\mathbf{q}_1}\hat{a}_{\mathbf{q}_2}|\mathrm{gnd}\rangle \quad \text{and} \quad |\mathbf{q}_3, \mathbf{0}\rangle = \hat{a}_{\mathbf{0}}^\dagger\,\hat{a}_{\mathbf{q}_3}^\dagger|\mathrm{gnd}\rangle, \tag{G.4}$$

where $\hat{a}_{\mathbf{q}}^\dagger$ ($\hat{a}_{\mathbf{q}}$) creates (annihilates) a quasiparticle with quasimomentum $\mathbf{q}$, $|\mathrm{gnd}\rangle$ is the referential state

$$|\mathrm{gnd}\rangle = \prod_{\mathbf{q}} \frac{(\hat{a}_{\mathbf{q}}^\dagger)^{n_{\mathbf{q}}^i}}{(n_{\mathbf{q}}^i!)^{1/2}}|\mathrm{vac}\rangle, \tag{G.5}$$

and $n^i_{\mathbf{q}}$ is the initial occupation number, which is either 0 or 1 in the classical regime. The initial and final states are properly normalized if we consider $n^i_{\mathbf{0}} = n^i_{\mathbf{q}_1+\mathbf{q}_2} = 0$ and $n^i_{\mathbf{q}_1} = n^i_{\mathbf{q}_2} = 1$.

Using the transformation

$$\hat{a}_j = \frac{1}{\sqrt{N_s}} \sum_{\mathbf{q}} e^{\frac{i}{\hbar}\mathbf{q}\cdot\mathbf{r}_j} \hat{a}_{\mathbf{q}}, \tag{G.6}$$

We convert the Hamiltonian in Eq. G.3 into the quasimomentum space, where N_s is the number of lattice sites and the sum extends over the first BZ. The matrix element is therefore

$$\begin{aligned}\langle \mathbf{q}_3, \mathbf{0}|\hat{H}|\mathbf{q}_1, \mathbf{q}_2\rangle &= \frac{U}{2N_s^2} \sum_{\mathbf{q}\,\mathbf{q}'\mathbf{q}''\mathbf{q}'''} \langle \mathbf{q}_3, \mathbf{0}|\hat{a}^\dagger_{\mathbf{q}}\hat{a}^\dagger_{\mathbf{q}'}\hat{a}_{\mathbf{q}''}\hat{a}_{\mathbf{q}'''}|\mathbf{q}_1, \mathbf{q}_2\rangle \sum_j e^{\frac{i}{\hbar}(\mathbf{q}+\mathbf{q}'-\mathbf{q}''-\mathbf{q}''')\cdot r_j} \\ &= \frac{U}{2N_s} \sum_{\mathbf{q}\,\mathbf{q}'\mathbf{q}''\mathbf{q}'''} \langle \mathbf{q}_3, \mathbf{0}|\hat{a}^\dagger_{\mathbf{q}}\hat{a}^\dagger_{\mathbf{q}'}\hat{a}_{\mathbf{q}''}\hat{a}_{\mathbf{q}'''}|\mathbf{q}_1, \mathbf{q}_2\rangle \tilde{\delta}_{\mathbf{q}+\mathbf{q}',\mathbf{q}''+\mathbf{q}'''},\end{aligned} \tag{G.7}$$

where $\tilde{\delta}_{\mathbf{q},\mathbf{q}'}$ is the periodic Kronecker delta[1]. Because the final state $|\mathbf{q}_3, \mathbf{0}\rangle$ has the operator $\hat{a}^\dagger_{\mathbf{0}}$, the sum over $\mathbf{q}$ and $\mathbf{q}'$ results in only two nonzero terms: one term with $\mathbf{q} = \mathbf{0}$ and $\mathbf{q}' = \mathbf{q}'' + \mathbf{q}'''$, and another with $\mathbf{q}' = \mathbf{0}$ and $\mathbf{q} = \mathbf{q}'' + \mathbf{q}'''$. Therefore

$$\langle \mathbf{q}_3, \mathbf{0}|\hat{H}_{\text{int}}|\mathbf{q}_1, \mathbf{q}_2\rangle = \frac{U}{N_s} \sum_{\mathbf{q}''\mathbf{q}'''} \langle \mathbf{q}_3, \mathbf{0}|\hat{a}^\dagger_0\hat{a}^\dagger_{\mathbf{q}''+\mathbf{q}'''}\hat{a}_{\mathbf{q}''}\hat{a}_{\mathbf{q}'''}|\mathbf{q}_1, \mathbf{q}_2\rangle. \tag{G.8}$$

Similarly, the sum over $\mathbf{q}''$ and $\mathbf{q}''$ leads to a term with $\mathbf{q}'' = \mathbf{q}_1$ and $\mathbf{q}''' = \mathbf{q}_2$, and another with $\mathbf{q}'' = \mathbf{q}_2$ and $\mathbf{q}''' = \mathbf{q}_1$. Moreover, Eq. G.8 is zero unless $\mathbf{q}_3 = \mathbf{q}_1 + \mathbf{q}_2$. Therefore

$$\langle \mathbf{q}_3, \mathbf{0}|\hat{H}_{\text{int}}|\mathbf{q}_1, \mathbf{q}_2\rangle = \frac{2U}{N_s} \tilde{\delta}_{\mathbf{q}_3,\mathbf{q}_1+\mathbf{q}_2}. \tag{G.9}$$

The total rate is then given by

$$\frac{\partial \mathbb{n}_0}{\partial \tau} = \frac{1}{2} \sum_{\mathbf{q}_1\mathbf{q}_2} \mathbb{n}^{\text{eq}}_{\mathbf{q}_1} \mathbb{n}^{\text{eq}}_{\mathbf{q}_2} \frac{2\pi}{\hbar} \left(\frac{2U}{N_s}\right)^2 \delta(\epsilon_{\mathbf{q}_1} + \epsilon_{\mathbf{q}_2} - \epsilon_{\mathbf{q}_1+\mathbf{q}_2} - \epsilon_{\mathbf{0}}), \tag{G.10}$$

where we have divided by 2 to account for double counting, $\epsilon_{\mathbf{q}}$ is the ground-band dispersion relation $\epsilon_{\mathbf{q}} = 2t \sum_{i=x,y,z}[1-\cos(q_i/q_B)]$ in the tight-binding approximation (notice that $\epsilon_{\mathbf{0}} = 0$) and $\mathbb{n}^{\text{eq}}_{\mathbf{q}} = e^{-\beta(\epsilon_{\mathbf{q}}-\mu)}$.

After transforming sums into integrals $\sum_{\mathbf{q}} \to N_s \int \frac{d^3q}{(2\pi)^3}$ (we consider q dimensionless to preserve the correct units), Eq. G.3 becomes

$$\frac{1}{\tau_0} = \frac{2U^2}{\hbar} \frac{\int \frac{d^3q_1}{(2\pi)^3} \frac{d^3q_2}{(2\pi)^3} e^{-\beta(\epsilon_{\mathbf{q}_1}+\epsilon_{\mathbf{q}_2}-2\mu)} 2\pi\delta(\epsilon_{\mathbf{q}_1} + \epsilon_{\mathbf{q}_2} - \epsilon_{\mathbf{q}_1+\mathbf{q}_2})}{e^{\beta\mu}} \tag{G.11}$$

[1]The periodic Kronecker delta satisfies $\tilde{\delta}_{\mathbf{q},\mathbf{q}'} = 1$ if $\mathbf{q} - \mathbf{q}'$ is a reciprocal lattice vector; $\tilde{\delta}_{\mathbf{q},\mathbf{q}'} = 0$ otherwise.

Dividing both sides by the lattice filing $\mathbb{n} = \int \frac{d^3q}{(2\pi)^3} e^{-\beta(\epsilon_{\mathbf{q}}-\mu)}$, and defining $C(\mathbf{q}) = \sum_{i=x,y,z}(1-\cos q_i)$ results in

$$\frac{1}{\tau_0} = \frac{2}{\hbar}\,\mathbb{n}\,F\left(\frac{t}{k_BT}\right)\frac{U^2}{t} \tag{G.12}$$

where

$$F(x) = \frac{\int \frac{d^3q_1}{(2\pi)^3}\frac{d^3q_2}{(2\pi)^3} e^{-2x[C(\mathbf{q}_1)+C(\mathbf{q}_2)]} 2\pi\delta(2C(\mathbf{q}_1)+2C(\mathbf{q}_2)-2C(\mathbf{q}_1+\mathbf{q}_2))}{\int \frac{d^3q}{(2\pi)^3} e^{-2xC(\mathbf{q})}}. \tag{G.13}$$

Notice that the equilibration rate in Eq. 5.11 has an additional factor of 2 because we predict the relaxation time of the squared quasimomentum distribution.

In the experiments carried out in Chapter 5, $\mathbb{n}$ varies across the trap because of the overall harmonically confinement. In order to compare the experimental measurements with the theoretical predictions, we average $\mathbb{n}$ in Eq. G.12 across the gas using $\langle \mathbb{n} \rangle = \int d^3r\, n(\mathbf{r})\, \mathbb{n}(\mathbf{r})/\mathrm{N}$, where N is the atom number,

$$n(\mathbf{r}) = N\left(\frac{\beta m\omega^2}{2\pi}\right)^{3/2} e^{-\frac{\beta}{2}m\omega^2\mathbf{r}^2} \tag{G.14}$$

is the gas density, and the lattice filling is $\mathbb{n}(\mathbf{r}) = n(\mathbf{r})d^3$. Therefore, the density-weighted filling is

$$\langle \mathbb{n} \rangle = N\left(\frac{\beta m\omega^2 d^2}{4\pi}\right)^{3/2} \tag{G.15}$$

Appendix H

Experimental Data Index

All the experimental data are located at:

\\phyfalle.physics.uiuc.edu\data share\lattice\

Data for Chapter 3

- 8/21/10 – $\log^2$ ramp
- 8/30/10 – Linear ramp

Data for Chapter 4

- 11/6/12 – Band decay in a 13.5 E_R lattice
- 12/2/12, 12/6/12, 12/18/12 –Band decay in a 16.2 E_R lattice
- 11/17/12, 12/8/12 – Band decay in a 18 E_R lattice

Data for Chapter 5

- 12/21/13 – Cooling in a 4 E_R lattice
- 6/15/14 – Relaxation in 4 E_R and 8 E_R lattices
- 7/30/14 – Relaxation in a 6 E_R lattice
- 8/17/14 – Relaxation in a 5 E_R lattice

References

[1] D. Chen, M. White, C. Borries, and B. DeMarco, "Quantum quench of an atomic Mott insulator," *Phys. Rev. Lett.*, vol. 106, p. 235304, Jun 2011. ii, 48

[2] D. Chen, C. Meldgin, and B. DeMarco, "Bath-induced band decay of a Hubbard lattice gas," *Phys. Rev. A*, vol. 90, p. 013602, Jul 2014. ii

[3] D. Chen, C. Meldgin, P. Russ, E. Mueller, and B. DeMarco, "Quasimomentum cooling and relaxation in a strongly correlated optical lattice," *arXiv:1503.07606*, 2015. iii

[4] P. J. Mohr, B. N. Taylor, and D. B. Newell, "Codata recommended values of the fundamental physical constants: 2010," *Rev. Mod. Phys.*, vol. 84, pp. 1527–1605, Nov 2012. x

[5] E. G. M. van Kempen, S. J. J. M. F. Kokkelmans, D. J. Heinzen, and B. J. Verhaar, "Interisotope determination of ultracold rubidium interactions from three high-precision experiments," *Phys. Rev. Lett.*, vol. 88, p. 093201, Feb 2002. x

[6] J. Eisert, M. Friesdorf, and C. Gogolin, "Quantum many-body systems out of equilibrium," *Nature Physics*, vol. 11, no. 2, pp. 124–130, 2015. 1, 91

[7] R. Orus, "A practical introduction to tensor networks: Matrix product states and projected entangled pair states," *Annals of Physics*, vol. 349, no. 0, pp. 117 – 158, 2014. 1

[8] E. Dagotto, "Complexity in strongly correlated electronic systems," *Science*, vol. 309, no. 5732, pp. 257–262, 2005. 1

[9] V. Vedral, "Mean-field approximations and multipartite thermal correlations," *New Journal of Physics*, vol. 6, no. 1, p. 22, 2004. 1

[10] U. Schollwöck, "The density-matrix renormalization group in the age of matrix product states," *Annals of Physics*, vol. 326, no. 1, pp. 96 – 192, 2011. January 2011 Special Issue. 1

[11] R. Feynman, "Simulating physics with computers," *International Journal of Theoretical Physics*, vol. 21, no. 6-7, pp. 467–488, 1982. 1

[12] M. Lewenstein, A. Sanpera, V. Ahufinger, B. Damski, A. Sen(De), and U. Sen, "Ultracold atomic gases in optical lattices: mimicking condensed matter physics and beyond," *Advances in Physics*, vol. 56, no. 2, pp. 243–379, 2007. 1

[13] I. Bloch, J. Dalibard, and W. Zwerger, "Many-body physics with ultracold gases," *Rev. Mod. Phys.*, vol. 80, pp. 885–964, Jul 2008. 1, 10

[14] M. Greiner and S. Fölling, "Condensed-matter physics: Optical lattices," *Nature*, vol. 453, no. 7196, pp. 736–738, 2008. 1

[15] J. I. Cirac and P. Zoller, "Goals and opportunities in quantum simulation," *Nature Physics*, vol. 8, no. 4, pp. 264–266, 2012. 1

[16] I. Bloch, J. Dalibard, and S. Nascimbène, "Quantum simulations with ultracold quantum gases," *Nature Physics*, vol. 8, no. 4, pp. 267–276, 2012. 1

[17] T. Esslinger, "Fermi-Hubbard physics with atoms in an optical lattice," *Annu. Rev. Condens. Matter Phys.*, vol. 1, pp. 129–152, Aug 2010. 1

[18] A. Auerbach, *Interacting electrons and quantum magnetism*. Springer, 1994. 1, 2, 10

[19] M. Greiner, *Ultracold quantum gases in three-dimensional optical lattice potentials*. PhD thesis, Universität München, 2003. 1, 10, 11, 13

[20] U. Schneider, L. Hackermller, S. Will, T. Best, I. Bloch, T. A. Costi, R. W. Helmes, D. Rasch, and A. Rosch, "Metallic and insulating phases of repulsively interacting fermions in a 3D optical lattice," *Science*, vol. 322, no. 5907, pp. 1520–1525, 2008. 1

[21] R. Jördens, N. Strohmaier, K. Günter, H. Moritz, and T. Esslinger, "A Mott insulator of fermionic atoms in an optical lattice," *Nature*, vol. 455, no. 7210, pp. 204–207, 2008. 1

[22] S. S. Kondov, W. R. McGehee, J. J. Zirbel, and B. DeMarco, "Three-dimensional Anderson localization of ultracold matter," *Science*, vol. 334, no. 6052, pp. 66–68, 2011. 1

[23] M. Schreiber, S. S. Hodgman, P. Bordia, H. P. Lüschen, M. H. Fischer, R. Vosk, E. Altman, U. Schneider, and I. Bloch, "Observation of many-body localization of interacting fermions in a quasi-random optical lattice," *arXiv:1501.05661*, 2015. 1

[24] T. Best, S. Will, U. Schneider, L. Hackermüller, D. van Oosten, I. Bloch, and D.-S. Lühmann, "Role of interactions in ^{87}Rb $-^{40}$ K Bose-Fermi mixtures in a 3D optical lattice," *Phys. Rev. Lett.*, vol. 102, p. 030408, Jan 2009. 1

[25] J. Simon, W. S. Bakr, R. Ma, M. E. Tai, P. M. Preiss, and M. Greiner, "Quantum simulation of antiferromagnetic spin chains in an optical lattice," *Nature*, vol. 472, no. 7343, pp. 307–312, 2011. 1

[26] D. Greif, T. Uehlinger, G. Jotzu, L. Tarruell, and T. Esslinger, "Short-range quantum magnetism of ultracold fermions in an optical lattice," *Science*, vol. 340, no. 6138, pp. 1307–1310, 2013. 1

[27] R. A. Hart, P. M. Duarte, T.-L. Yang, X. Liu, T. Paiva, E. Khatami, R. T. Scalettar, N. Trivedi, D. A. Huse, and R. G. Hulet, "Observation of antiferromagnetic correlations in the Hubbard model with ultracold atoms," *Nature*, vol. 519, no. 7542, pp. 211–214, 2015. 2, 15, 71

[28] X. Zhang, C.-L. Hung, S.-K. Tung, N. Gemelke, and C. Chin, "Exploring quantum criticality based on ultracold atoms in optical lattices," *New Journal of Physics*, vol. 13, no. 4, p. 045011, 2011. 2, 53

[29] X. Zhang, C.-L. Hung, S.-K. Tung, and C. Chin, "Observation of quantum criticality with ultracold atoms in optical lattices," *Science*, vol. 335, no. 6072, pp. 1070–1072, 2012. 2

[30] J. Dziarmaga, "Dynamics of a quantum phase transition and relaxation to a steady state," *Advances in Physics*, vol. 59, no. 6, pp. 1063–1189, 2010. 2, 33, 34, 35, 36, 48, 52

[31] R. Schützhold and G. Schaller, "Adiabatic quantum algorithms as quantum phase transitions: First versus second order," *Phys. Rev. A*, vol. 74, p. 060304, Dec 2006. 2, 33, 53

[32] T. W. B. Kibble, "Topology of cosmic domains and strings," *Journal of Physics A: Mathematical and General*, vol. 9, no. 8, p. 1387, 1976. 2, 33

[33] T. Kibble, "Some implications of a cosmological phase transition," *Physics Reports*, vol. 67, no. 1, pp. 183 – 199, 1980. 2

[34] W. Zurek, "Cosmological experiments in superfluid helium?," *Nature*, vol. 317, no. 6037, pp. 505–508, 1985. 2, 33

[35] W. Zurek, "Cosmological experiments in condensed matter systems," *Physics Reports*, vol. 276, no. 4, pp. 177 – 221, 1996. 2

[36] S. Trotzky, Y.-A. Chen, A. Flesch, I. P. McCulloch, U. Schollwöck, J. Eisert, and I. Bloch, "Probing the relaxation towards equilibrium in an isolated strongly correlated one-dimensional Bose gas," *Nature Physics*, vol. 8, no. 4, pp. 325–330, 2012. 2

[37] M. Cheneau, P. Barmettler, D. Poletti, M. Endres, P. Schauß, T. Fukuhara, C. Gross, I. Bloch, C. Kollath, and S. Kuhr, "Light-cone-like spreading of correlations in a quantum many-body system," *Nature*, vol. 481, no. 7382, pp. 484–487, 2012. 2

[38] F. Meinert, M. J. Mark, E. Kirilov, K. Lauber, P. Weinmann, A. J. Daley, and H. C. Nägerl, "Quantum quench in an atomic one-dimensional ising chain," *Phys. Rev. Lett.*, vol. 111, p. 053003, Jul 2013. 2

[39] F. Meinert, M. J. Mark, E. Kirilov, K. Lauber, P. Weinmann, M. Gröbner, A. J. Daley, and H.-C. Nägerl, "Observation of many-body dynamics in long-range tunneling after a quantum quench," *Science*, vol. 344, no. 6189, pp. 1259–1262, 2014. 2

[40] U. Schneider, L. Hackermüller, J. P. Ronzheimer, S. Will, S. Braun, T. Best, I. Bloch, E. Demler, S. Mandt, D. Rasch, *et al.*, "Fermionic transport and out-of-equilibrium dynamics in a homogeneous Hubbard model with ultracold atoms," *Nature Physics*, vol. 8, no. 3, pp. 213–218, 2012. 2

[41] J. P. Ronzheimer, M. Schreiber, S. Braun, S. S. Hodgman, S. Langer, I. P. McCulloch, F. Heidrich-Meisner, I. Bloch, and U. Schneider, "Expansion dynamics of interacting bosons in homogeneous lattices in one and two dimensions," *Phys. Rev. Lett.*, vol. 110, p. 205301, May 2013. 2

[42] R. Hill, C. Proust, L. Taillefer, P. Fournier, and R. Greene, "Breakdown of Fermi-liquid theory in a copper-oxide superconductor," *Nature*, vol. 414, no. 6865, pp. 711–715, 2001. 2

[43] A. J. Leggett, "What do we know about high tc?," *Nature Physics*, vol. 2, no. 3, pp. 134–136, 2006. 2

[44] B. Keimer, S. Kivelson, M. Norman, S. Uchida, and J. Zaanen, "From quantum matter to high-temperature superconductivity in copper oxides," *Nature*, vol. 518, no. 7538, pp. 179–186, 2015. 2

[45] P. A. Lee, N. Nagaosa, and X.-G. Wen, "Doping a Mott insulator: Physics of high-temperature superconductivity," *Rev. Mod. Phys.*, vol. 78, pp. 17–85, Jan 2006. 2

[46] A. M. Rey, R. Sensarma, S. Fölling, M. Greiner, E. Demler, and M. D. Lukin, "Controlled preparation and detection of d-wave superfluidity in two-dimensional optical superlattices," *Europhysics Letters (EPL)*, vol. 87, no. 6, p. 60001, 2009. 2

[47] T.-L. Ho and Q. Zhou, "Intrinsic heating and cooling in adiabatic processes for bosons in optical lattices," *Phys. Rev. Lett.*, vol. 99, p. 120404, Sep 2007. 2

[48] R. Jördens, L. Tarruell, D. Greif, T. Uehlinger, N. Strohmaier, H. Moritz, T. Esslinger, L. De Leo, C. Kollath, A. Georges, V. Scarola, L. Pollet, E. Burovski, E. Kozik, and M. Troyer, "Quantitative determination of temperature in the approach to magnetic order of ultracold fermions in an optical lattice," *Phys. Rev. Lett.*, vol. 104, p. 180401, May 2010. 2

[49] P. Rabl, A. J. Daley, P. O. Fedichev, J. I. Cirac, and P. Zoller, "Defect-suppressed atomic crystals in an optical lattice," *Phys. Rev. Lett.*, vol. 91, p. 110403, Sep 2003. 3, 71

[50] F. Heidrich-Meisner, S. R. Manmana, M. Rigol, A. Muramatsu, A. E. Feiguin, and E. Dagotto, "Quantum distillation: Dynamical generation of low-entropy states of strongly correlated fermions in an optical lattice," *Phys. Rev. A*, vol. 80, p. 041603, Oct 2009. 3, 71

[51] J.-S. Bernier, C. Kollath, A. Georges, L. De Leo, F. Gerbier, C. Salomon, and M. Köhl, "Cooling fermionic atoms in optical lattices by shaping the confinement," *Phys. Rev. A*, vol. 79, p. 061601, Jun 2009. 3, 71

[52] T.-L. Ho and Q. Zhou, "Universal cooling scheme for quantum simulation," *ArXiv:0911.5506*, Nov. 2009. 3, 71

[53] J. R. Williams, J. H. Huckans, R. W. Stites, E. L. Hazlett, and K. M. O'Hara, "Preparing a highly degenerate Fermi gas in an optical lattice," *Phys. Rev. A*, vol. 82, p. 011610, Jul 2010. 3, 71

[54] M. Popp, J.-J. García-Ripoll, K. G. H. Vollbrecht, and J. I. Cirac, "Cooling toolbox for atoms in optical lattices," *New Journal of Physics*, vol. 8, no. 8, p. 164, 2006. 3, 71

[55] M. Popp, J.-J. García-Ripoll, K. G. Vollbrecht, and J. I. Cirac, "Ground-state cooling of atoms in optical lattices," *Phys. Rev. A*, vol. 74, p. 013622, Jul 2006. 3, 71

[56] W. S. Bakr, P. M. Preiss, M. E. Tai, R. Ma, J. Simon, and M. Greiner, "Orbital excitation blockade and algorithmic cooling in quantum gases," *Nature*, vol. 480, no. 7378, pp. 500–503, 2011. 3, 71

[57] P. Medley, D. Weld, H. Miyake, D. Pritchard, and W. Ketterle, "Spin gradient demagnetization cooling of ultracold atoms," *Phys. Rev. Lett.*, vol. 106, p. 195301, May 2011. 3, 71

[58] A. Griessner, A. J. Daley, S. R. Clark, D. Jaksch, and P. Zoller, "Dark-state cooling of atoms by superfluid immersion," *Phys. Rev. Lett.*, vol. 97, p. 220403, Nov 2006. 3, 55, 69

[59] A. Griessner, A. J. Daley, S. R. Clark, D. Jaksch, and P. Zoller, "Dissipative dynamics of atomic Hubbard models coupled to a phonon bath: dark state cooling of atoms within a Bloch band of an optical lattice," *New Journal of Physics*, vol. 9, no. 2, p. 44, 2007. 3, 55

[60] M. Hermele and V. Gurarie, "Topological liquids and valence cluster states in two-dimensional SU(N) magnets," *Phys. Rev. B*, vol. 84, p. 174441, Nov 2011. 3, 91

[61] C. Wu, "Quantum gases: Mott made easy," *Nature Physics*, vol. 8, no. 11, pp. 784–785, 2012. 3

[62] Z. Cai, H.-H. Hung, L. Wang, and C. Wu, "Quantum magnetic properties of the SU(2N) Hubbard model in the square lattice: A quantum monte carlo study," *Phys. Rev. B*, vol. 88, p. 125108, Sep 2013. 3, 91

[63] F. Hébert, Z. Cai, V. G. Rousseau, C. Wu, R. T. Scalettar, and G. G. Batrouni, "Exotic phases of interacting p-band bosons," *Phys. Rev. B*, vol. 87, p. 224505, Jun 2013. 3, 70

[64] S. Braun, J. P. Ronzheimer, M. Schreiber, S. S. Hodgman, T. Rom, I. Bloch, and U. Schneider, "Negative absolute temperature for motional degrees of freedom," *Science*, vol. 339, no. 6115, pp. 52–55, 2013. 3

[65] F. Pinheiro, J.-P. Martikainen, and J. Larson, "Phases of d-orbital bosons in optical lattices," *ArXiv:1501.03514*, jan 2015. 3, 70

[66] M. White, *Ultracold Atoms in A Disordered Optical Lattice*. PhD thesis, University of Illinois at Urbana-Champaign, 2009. 3, 6, 7, 8, 10, 12, 30

[67] Y.-J. Lin, A. R. Perry, R. L. Compton, I. B. Spielman, and J. V. Porto, "Rapid production of ^{87}Rb Bose-Einstein condensates in a combined magnetic and optical potential," *Phys. Rev. A*, vol. 79, p. 063631, Jun 2009. 4, 87

[68] H. Metcalf and P. van der Straten, *Laser Cooling and Trapping*. Graduate Texts in Contemporary Physics, Springer New York, 1999. 4

[69] R. Grimm, M. Weidemüller, and Y. B. Ovchinnikov, "Optical dipole traps for neutral atoms," *Advances in atomic, molecular, and optical physics*, vol. 42, pp. 95–170, 2000. 4

[70] C. Foot, *Atomic Physics*. Oxford University Press, 2005. 4

[71] C. J. Pethick and H. Smith, *Bose-Einstein Condensation in Dilute Gases*. Cambridge University Press, second ed., 2008. 4, 12, 41, 42, 43, 50, 60, 92, 97, 99

[72] D. McKay, *Quantum Simulation in Strongly Correlated Optical Lattices*. PhD thesis, University of Illinois at Urbana-Champaign, 2012. 4, 7, 8, 10, 11, 12, 98, 99

[73] D. Steck, "Rubidium 87 d line data." http://steck.us/alkalidata/, 2001. 5, 20, 74

[74] E. Majorana, "Majorana flops," *Nuovo Cimento*, vol. 9, p. 43, 1932. 7

[75] M. Pasienski, *Transport Properties of Ultracold Atoms in a Disordered Optical Lattice*. PhD thesis, University of Illinois at Urbana-Champaign, 2011. 7, 106

[76] G. Breit and I. I. Rabi, "Measurement of nuclear spin," *Phys. Rev.*, vol. 38, pp. 2082–2083, Dec 1931. 7

[77] D. McKay and B. DeMarco, "Thermometry with spin-dependent lattices," *New Journal of Physics*, vol. 12, no. 5, p. 055013, 2010. 9, 56, 65, 98

[78] H. Pichler, A. J. Daley, and P. Zoller, "Nonequilibrium dynamics of bosonic atoms in optical lattices: Decoherence of many-body states due to spontaneous emission," *Phys. Rev. A*, vol. 82, p. 063605, Dec 2010. 9

[79] N. W. Ashcroft and N. D. Mermin, *Solid State Physics*. Saunders College, 1976. 10

[80] M. Lewenstein, A. Sanpera, and V. Ahufinger, *Ultracold Atoms in Optical Lattices: Simulating quantum many-body systems*. Oxford University Press, 2012. 10, 71

[81] N. Marzari, A. A. Mostofi, J. R. Yates, I. Souza, and D. Vanderbilt, "Maximally localized Wannier functions: Theory and applications," *Rev. Mod. Phys.*, vol. 84, pp. 1419–1475, Oct 2012. 11

[82] Y. Castin and R. Dum, "Bose-Einstein condensates in time dependent traps," *Phys. Rev. Lett.*, vol. 77, pp. 5315–5319, Dec 1996. 12

[83] R. Shankar, R. Shankar, and R. Shankar, *Principles of quantum mechanics*, vol. 233. Plenum Press New York, 1994. 13

[84] S. Fölling, F. Gerbier, A. Widera, O. Mandel, T. Gericke, and I. Bloch, "Spatial quantum noise interferometry in expanding ultracold atom clouds," *Nature*, vol. 434, no. 7032, pp. 481–484, 2005. 13

[85] D. McKay, M. White, and B. DeMarco, "Lattice thermodynamics for ultracold atoms," *Phys. Rev. A*, vol. 79, p. 063605, Jun 2009. 13, 57, 87, 98

[86] S. S. Natu, D. C. McKay, B. DeMarco, and E. J. Mueller, "Evolution of condensate fraction during rapid lattice ramps," *Phys. Rev. A*, vol. 85, p. 061601, Jun 2012. 13, 78

[87] M. Kasevich and S. Chu, "Laser cooling below a photon recoil with three-level atoms," *Phys. Rev. Lett.*, vol. 69, pp. 1741–1744, Sep 1992. 15

[88] S. E. Hamann, D. L. Haycock, G. Klose, P. H. Pax, I. H. Deutsch, and P. S. Jessen, "Resolved-sideband Raman cooling to the ground state of an optical lattice," *Phys. Rev. Lett.*, vol. 80, pp. 4149–4152, May 1998. 15

[89] A. J. Kerman, V. Vuletić, C. Chin, and S. Chu, "Beyond optical molasses: 3D Raman sideband cooling of atomic cesium to high phase-space density," *Phys. Rev. Lett.*, vol. 84, pp. 439–442, Jan 2000. 15

[90] F. Gerbier, J. H. Thywissen, S. Richard, M. Hugbart, P. Bouyer, and A. Aspect, "Experimental study of the thermodynamics of an interacting trapped Bose-Einstein condensed gas," *Phys. Rev. A*, vol. 70, p. 013607, Jul 2004. 15

[91] P. T. Ernst, S. Götze, J. S. Krauser, K. Pyka, D.-S. Lühmann, D. Pfannkuche, and K. Sengstock, "Probing superfluids in optical lattices by momentum-resolved Bragg spectroscopy," *Nature Physics*, vol. 6, no. 1, pp. 56–61, 2009. 15

[92] T. Müller, S. Fölling, A. Widera, and I. Bloch, "State preparation and dynamics of ultracold atoms in higher lattice orbitals," *Phys. Rev. Lett.*, vol. 99, p. 200405, Nov 2007. 15, 58

[93] T. A. Corcovilos, S. K. Baur, J. M. Hitchcock, E. J. Mueller, and R. G. Hulet, "Detecting antiferromagnetism of atoms in an optical lattice via optical Bragg scattering," *Phys. Rev. A*, vol. 81, p. 013415, Jan 2010. 15

[94] Y.-J. Lin, R. L. Compton, K. Jiménez-García, J. V. Porto, and I. B. Spielman, "Synthetic magnetic fields for ultracold neutral atoms," *Nature*, vol. 462, no. 7273, pp. 628–632, 2009. 15

[95] Y.-J. Lin, R. L. Compton, K. Jiménez-García, W. D. Phillips, J. V. Porto, and I. B. Spielman, "A synthetic electric force acting on neutral atoms," *Nature Physics*, vol. 7, no. 7, pp. 531–534, 2011. 15

[96] M. Aidelsburger, M. Atala, S. Nascimbène, S. Trotzky, Y.-A. Chen, and I. Bloch, "Experimental realization of strong effective magnetic fields in an optical lattice," *Phys. Rev. Lett.*, vol. 107, p. 255301, Dec 2011. 15

[97] N. Goldman, G. Juzeliūnas, P. Öhberg, and I. B. Spielman, "Light-induced gauge fields for ultracold atoms," *Reports on Progress in Physics*, vol. 77, no. 12, p. 126401, 2014. 15

[98] J. Dalibard, "Introduction to the physics of artificial gauge fields," *arXiv:1504.05520*, 2015. 15

[99] Y.-J. Lin, K. Jiménez-García, and I. B. Spielman, "Spin-orbit-coupled Bose-Einstein condensates," *Nature*, vol. 471, no. 7336, pp. 83–86, 2011. 15

[100] P. Wang, Z.-Q. Yu, Z. Fu, J. Miao, L. Huang, S. Chai, H. Zhai, and J. Zhang, "Spin-orbit coupled degenerate Fermi gases," *Physical review letters*, vol. 109, no. 9, p. 095301, 2012. 15

[101] V. Galitski and I. B. Spielman, "Spin-orbit coupling in quantum gases," *Nature*, vol. 494, no. 7435, pp. 49–54, 2013. 15

[102] L. J. LeBlanc, K. Jiménez-García, R. A. Williams, M. C. Beeler, A. R. Perry, W. D. Phillips, and I. B. Spielman, "Observation of a superfluid Hall effect," *Proceedings of the National Academy of Sciences*, vol. 109, no. 27, pp. 10811–10814, 2012. 15

[103] M. Beeler, R. Williams, K. Jiménez-García, L. LeBlanc, A. Perry, and I. Spielman, "The spin Hall effect in a quantum gas," *Nature*, vol. 498, no. 7453, pp. 201–204, 2013. 15

[104] M. Aidelsburger, M. Atala, M. Lohse, J. T. Barreiro, B. Paredes, and I. Bloch, "Realization of the Hofstadter Hamiltonian with ultracold atoms in optical lattices," *Phys. Rev. Lett.*, vol. 111, p. 185301, Oct 2013. 15

[105] H. Miyake, G. A. Siviloglou, C. J. Kennedy, W. C. Burton, and W. Ketterle, "Realizing the Harper Hamiltonian with laser-assisted tunneling in optical lattices," *Phys. Rev. Lett.*, vol. 111, p. 185302, Oct 2013. 15

[106] G. Jotzu, M. Messer, R. Desbuquois, M. Lebrat, T. Uehlinger, D. Greif, and T. Esslinger, "Experimental realization of the topological Haldane model with ultracold fermions," *Nature*, vol. 515, no. 7526, pp. 237–240, 2014. 15

[107] L. Mazza, A. Bermudez, N. Goldman, M. Rizzi, M. A. Martin-Delgado, and M. Lewenstein, "An optical-lattice-based quantum simulator for relativistic field theories and topological insulators," *New Journal of Physics*, vol. 14, no. 1, p. 015007, 2012. 15

[108] N. Goldman, J. Beugnon, and F. Gerbier, "Detecting chiral edge states in the Hofstadter optical lattice," *Phys. Rev. Lett.*, vol. 108, p. 255303, Jun 2012. 15

[109] N. Goldman, E. Anisimovas, F. Gerbier, P. Öberg, I. B. Spielman, and G. Juzeliūnas, "Measuring topology in a laser-coupled honeycomb lattice: from Chern insulators to topological semi-metals," *New Journal of Physics*, vol. 15, no. 1, p. 013025, 2013. 15

[110] N. Goldman, J. Dalibard, A. Dauphin, F. Gerbier, M. Lewenstein, P. Zoller, and I. B. Spielman, "Direct imaging of topological edge states in cold-atom systems," *Proceedings of the National Academy of Sciences*, vol. 110, no. 17, pp. 6736–6741, 2013. 15

[111] I. B. Spielman, "Detection of topological matter with quantum gases," *Annalen der Physik*, vol. 525, no. 10-11, pp. 797–807, 2013. 15

[112] S.-T. Wang, D.-L. Deng, and L.-M. Duan, "Probe of three-dimensional chiral topological insulators in an optical lattice," *Phys. Rev. Lett.*, vol. 113, p. 033002, Jul 2014. 15

[113] W. Li, L. Chen, Z. Chen, Y. Hu, Z. Zhang, and Z. Liang, "Probing the flat band of optically trapped spin-orbital-coupled Bose gases using Bragg spectroscopy," *Phys. Rev. A*, vol. 91, p. 023629, Feb 2015. 15

[114] J. J. Sakurai, *Modern Quantum Mechanics*. Addison-Wesley, 1993. 16

[115] L. Mandel and E. Wolf, *Optical coherence and quantum optics*. Cambridge university press, 1995. 16

[116] C. Cohen-Tannoudji, J. Dupont-Roc, and G. Grynberg, *Photons and atoms: introduction to quantum electrodynamics*. Wiley, 1997. 16

[117] B. W. Shore, *The Theory of Coherent Atomic Excitation*. Wiley-VCH, 1990. 17, 97

[118] M. Fewell, B. Shore, and K. Bergmann, "Coherent population transfer among three states: Full algebraic solutions and the relevance of non adiabatic processes to transfer by delayed pulses," *Australian journal of physics*, vol. 50, no. 2, pp. 281–308, 1997. 18

[119] E. Brion, L. H. Pedersen, and K. Mølmer, "Adiabatic elimination in a lambda system," *Journal of Physics A: Mathematical and Theoretical*, vol. 40, no. 5, p. 1033, 2007. 18

[120] R. Han, H. Khoon Ng, and B.-G. Englert, "Raman transitions without adiabatic elimination: a simple and accurate treatment," *Journal of Modern Optics*, vol. 60, no. 4, pp. 255–265, 2013. 18

[121] M. Kasevich and S. Chu, "Measurement of the gravitational acceleration of an atom with a light-pulse atom interferometer," *Applied Physics B*, vol. 54, no. 5, pp. 321–332, 1992. 18, 21, 23

[122] J. Bateman, A. Xuereb, and T. Freegarde, "Stimulated Raman transitions via multiple atomic levels," *Phys. Rev. A*, vol. 81, p. 043808, Apr 2010. 18, 19

[123] D. Budker, D. F. Kimball, and D. P. DeMille, *Atomic Physics*. Oxford Univ. Press, 2008. 20

[124] D. Wineland and W. Itano, "Laser cooling of atoms," *Phys. Rev. A*, vol. 20, pp. 1521–1540, Oct 1979. 21, 24

[125] P. F. Bernath, *Spectra of atoms and molecules*. Oxford University Press, 2005. 24

[126] D. J. Wineland, C. Monroe, W. Itano, D. Leibfried, B. King, and D. Meekhof, "Experimental issues in coherent quantum-state manipulation of trapped atomic ions," *J. Res. Natl. Inst. Stand. Technol*, vol. 103, p. 259, 1998. 24

[127] L. Förster, M. Karski, J.-M. Choi, A. Steffen, W. Alt, D. Meschede, A. Widera, E. Montano, J. H. Lee, W. Rakreungdet, and P. S. Jessen, "Microwave control of atomic motion in optical lattices," *Phys. Rev. Lett.*, vol. 103, p. 233001, Dec 2009. 24

[128] N. Belmechri, L. Frster, W. Alt, A. Widera, D. Meschede, and A. Alberti, "Microwave control of atomic motional states in a spin-dependent optical lattice," *Journal of Physics B: Atomic, Molecular and Optical Physics*, vol. 46, no. 10, p. 104006, 2013. 24

[129] B. E. A. Saleh and M. C. Teich, *Fundamentals of Photonics*. Wiley-Interscience, second ed., 2007. 26

[130] P. Laguna and W. H. Zurek, "Density of kinks after a quench: When symmetry breaks, how big are the pieces?," *Phys. Rev. Lett.*, vol. 78, pp. 2519–2522, Mar 1997. 33

[131] A. Yates and W. H. Zurek, "Vortex formation in two dimensions: When symmetry breaks, how big are the pieces?," *Phys. Rev. Lett.*, vol. 80, pp. 5477–5480, Jun 1998. 33

[132] J. Dziarmaga, "Density of Bloch waves after a quench," *Phys. Rev. Lett.*, vol. 81, pp. 5485–5488, Dec 1998. 33

[133] G. J. Stephens, E. A. Calzetta, B. L. Hu, and S. A. Ramsey, "Defect formation and critical dynamics in the early universe," *Phys. Rev. D*, vol. 59, p. 045009, Jan 1999. 33

[134] N. D. Antunes, L. M. A. Bettencourt, and W. H. Zurek, "Vortex string formation in a 3D U(1) temperature quench," *Phys. Rev. Lett.*, vol. 82, pp. 2824–2827, Apr 1999. 33

[135] J. Dziarmaga, P. Laguna, and W. H. Zurek, "Symmetry breaking with a slant: Topological defects after an inhomogeneous quench," *Phys. Rev. Lett.*, vol. 82, pp. 4749–4752, Jun 1999. 33

[136] M. Hindmarsh and A. Rajantie, "Defect formation and local gauge invariance," *Phys. Rev. Lett.*, vol. 85, pp. 4660–4663, Nov 2000. 33

[137] G. J. Stephens, L. M. A. Bettencourt, and W. H. Zurek, "Critical dynamics of gauge systems: Spontaneous vortex formation in 2D superconductors," *Phys. Rev. Lett.*, vol. 88, p. 137004, Mar 2002. 33

[138] I. Chuang, R. Durrer, N. Turok, and B. Yurke, "Cosmology in the laboratory: Defect dynamics in liquid crystals," *Science*, vol. 251, no. 4999, pp. 1336–1342, 1991. 33

[139] V. Ruutu, V. Eltsov, A. Gill, T. Kibble, M. Krusius, Y. G. Makhlin, B. Placais, G. Volovik, and W. Xu, "Vortex formation in neutron-irradiated superfluid 3He as an analogue of cosmological defect formation," *Nature*, vol. 382, pp. 334–336, 1996. 33

[140] C. Bauerle, Y. M. Bunkov, S. Fisher, H. Godfrin, and G. Pickett, "Laboratory simulation of cosmic-string formation in the early universe using superfluid ^{3}He," *Nature*, vol. 382, no. 6589, pp. 332–334, 1996. 33

[141] R. Monaco, J. Mygind, R. J. Rivers, and V. P. Koshelets, "Spontaneous fluxoid formation in superconducting loops," *Phys. Rev. B*, vol. 80, p. 180501, Nov 2009. 33

[142] D. Golubchik, E. Polturak, and G. Koren, "Evidence for long-range correlations within arrays of spontaneously created magnetic vortices in a nb thin-film superconductor," *Phys. Rev. Lett.*, vol. 104, p. 247002, Jun 2010. 33

[143] S. Casado, W. González-Viñas, S. Boccaletti, P. L. Ramazza, and H. Mancini, "The birth of defects in pattern formation: Testing of the Kibble-Zurek mechanism," *The European Physical Journal Special Topics*, vol. 146, no. 1, pp. 87–98, 2007. 33

[144] M. A. Miranda, J. Burguete, H. Mancini, and W. González-Viñas, "Frozen dynamics and synchronization through a secondary symmetry-breaking bifurcation," *Phys. Rev. E*, vol. 87, p. 032902, Mar 2013. 33

[145] C. N. Weiler, T. W. Neely, D. R. Scherer, A. S. Bradley, M. J. Davis, and B. P. Anderson, "Spontaneous vortices in the formation of Bose-Einstein condensates," *Nature*, vol. 455, no. 7215, pp. 948–951, 2008. 33

[146] G. Ferrari, "Spontaneous creation of Kibble-Zurek solitons in a Bose-Einstein condensate," *Bulletin of the American Physical Society*, vol. 59, 2014. 33

[147] R. Schützhold, M. Uhlmann, Y. Xu, and U. R. Fischer, "Sweeping from the superfluid to the Mott phase in the Bose-Hubbard model," *Phys. Rev. Lett.*, vol. 97, p. 200601, Nov 2006. 33

[148] F. M. Cucchietti, B. Damski, J. Dziarmaga, and W. H. Zurek, "Dynamics of the Bose-Hubbard model: Transition from a Mott insulator to a superfluid," *Phys. Rev. A*, vol. 75, p. 023603, Feb 2007. 33

[149] J. Dziarmaga, J. Meisner, and W. H. Zurek, "Winding up of the wave-function phase by an insulator-to-superfluid transition in a ring of coupled Bose-Einstein condensates," *Phys. Rev. Lett.*, vol. 101, p. 115701, Sep 2008. 33

[150] C. De Grandi, V. Gritsev, and A. Polkovnikov, "Quench dynamics near a quantum critical point: Application to the sine-gordon model," *Phys. Rev. B*, vol. 81, p. 224301, Jun 2010. 33, 50

[151] G. Roux, "Finite-size effects in global quantum quenches: Examples from free bosons in an harmonic trap and the one-dimensional Bose-Hubbard model," *Phys. Rev. A*, vol. 81, p. 053604, May 2010. 33, 50

[152] L. Mathey and A. Polkovnikov, "Light cone dynamics and reverse Kibble-Zurek mechanism in two-dimensional superfluids following a quantum quench," *Phys. Rev. A*, vol. 81, p. 033605, Mar 2010. 33

[153] C. De Grandi and A. Polkovnikov, "Quantum quenching, annealing and computation," *Eds. A. Das, A. Chandra and BK Chakrabarti, Lect. Notes in Phys*, vol. 802, 2010. 33

[154] M. Snoek, "Rigorous mean-field dynamics of lattice bosons: Quenches from the Mott insulator," *Europhysics Letters (EPL)*, vol. 95, no. 3, p. 30006, 2011. 33

[155] C. Trefzger and K. Sengupta, "Nonequilibrium dynamics of the Bose-Hubbard model: A projection-operator approach," *Phys. Rev. Lett.*, vol. 106, p. 095702, Feb 2011. 33

[156] M. Schiró and M. Fabrizio, "Quantum quenches in the Hubbard model: Time-dependent mean-field theory and the role of quantum fluctuations," *Phys. Rev. B*, vol. 83, p. 165105, Apr 2011. 33

[157] J. Dziarmaga, M. Tylutki, and W. H. Zurek, "Quench from Mott insulator to superfluid," *Phys. Rev. B*, vol. 86, p. 144521, Oct 2012. 33, 48, 50, 51, 52

[158] J. Dziarmaga and W. Zurek, "Quench in the 1D Bose-Hubbard model: Topological defects and excitations from the Kosterlitz-Thouless phase transition dynamics," *Scientific Reports*, vol. 4, p. 5950, August - 2014. 33, 52

[159] A. Polkovnikov, K. Sengupta, A. Silva, and M. Vengalattore, "*Colloquium*: Nonequilibrium dynamics of closed interacting quantum systems," *Rev. Mod. Phys.*, vol. 83, pp. 863–883, Aug 2011. 33

[160] A. Chandran, A. Erez, S. S. Gubser, and S. L. Sondhi, "Kibble-Zurek problem: Universality and the scaling limit," *Phys. Rev. B*, vol. 86, p. 064304, Aug 2012. 33

[161] A. Lamacraft and J. Moore, "Potential insights into non-equilibrium behavior from atomic physics," in *Ultracold Bosonic and Fermionic Gases* (K. Levin, A. Fetter, and D. Stamper-Kurn, eds.), vol. 5, Elsevier, 2012. 33

[162] A. del Campo and W. H. Zurek, "Universality of phase transition dynamics: Topological defects from symmetry breaking," *International Journal of Modern Physics A*, vol. 29, no. 08, p. 1430018, 2014. 33

[163] S. Sachdev, *Quantum phase transitions*. Wiley Online Library, 2007. 33, 34, 41, 48, 50

[164] N. Goldenfeld, *Lectures on phase transitions and the renormalization group*. Addison-Wesley, Advanced Book Program, Reading, 1992. 33, 34

[165] L. Sadler, J. Higbie, S. Leslie, M. Vengalattore, and D. Stamper-Kurn, "Spontaneous symmetry breaking in a quenched ferromagnetic spinor Bose-Einstein condensate," *Nature*, vol. 443, no. 7109, pp. 312–315, 2006. 36

[166] S. Braun, M. Friesdorf, S. S. Hodgman, M. Schreiber, J. P. Ronzheimer, A. Riera, M. del Rey, I. Bloch, J. Eisert, and U. Schneider, "Emergence of coherence and the dynamics of quantum phase transitions," *Proceedings of the National Academy of Sciences*, vol. 112, no. 12, pp. 3641–3646, 2015. 36

[167] M. Greiner, O. Mandel, T. Esslinger, T. W. Hänsch, and I. Bloch, "Quantum phase transition from a superfluid to a Mott insulator in a gas of ultracold atoms," *Nature*, vol. 415, no. 6867, pp. 39–44, 2002. 37

[168] W. S. Bakr, A. Peng, M. E. Tai, R. Ma, J. Simon, J. I. Gillen, S. Fölling, L. Pollet, and M. Greiner, "Probing the superfluid-to-Mott insulator transition at the single-atom level," *Science*, vol. 329, no. 5991, pp. 547–550, 2010. 37, 53

[169] M. P. A. Fisher, P. B. Weichman, G. Grinstein, and D. S. Fisher, "Boson localization and the superfluid-insulator transition," *Phys. Rev. B*, vol. 40, pp. 546–570, Jul 1989. 37, 41, 48, 50

[170] B. DeMarco, C. Lannert, S. Vishveshwara, and T.-C. Wei, "Structure and stability of Mott-insulator shells of bosons trapped in an optical lattice," *Phys. Rev. A*, vol. 71, p. 063601, Jun 2005. 37, 45

[171] W. Zwerger, "Mott-Hubbard transition of cold atoms in optical lattices," *Journal of Optics B: Quantum and Semiclassical Optics*, vol. 5, no. 2, p. S9, 2003. 39

[172] S. Dettmer, D. Hellweg, P. Ryytty, J. J. Arlt, W. Ertmer, K. Sengstock, D. S. Petrov, G. V. Shlyapnikov, H. Kreutzmann, L. Santos, and M. Lewenstein, "Observation of phase fluctuations in elongated Bose-Einstein condensates," *Phys. Rev. Lett.*, vol. 87, p. 160406, Oct 2001. 39

[173] D. S. Petrov, G. V. Shlyapnikov, and J. T. M. Walraven, "Phase-fluctuating 3D Bose-Einstein condensates in elongated traps," *Phys. Rev. Lett.*, vol. 87, p. 050404, Jul 2001. 39

[174] D. Hellweg, S. Dettmer, P. Ryytty, J. Arlt, W. Ertmer, K. Sengstock, D. Petrov, G. Shlyapnikov, H. Kreutzmann, L. Santos, and M. Lewenstein, "Phase fluctuations in Bose-Einstein condensates," *Applied Physics B*, vol. 73, no. 8, pp. 781–789, 2001. 39

[175] K. W. Madison, F. Chevy, W. Wohlleben, and J. Dalibard, "Vortex formation in a stirred Bose-Einstein condensate," *Phys. Rev. Lett.*, vol. 84, pp. 806–809, Jan 2000. 44

[176] Q. Zhou and T.-L. Ho, "Signature of quantum criticality in the density profiles of cold atom systems," *Phys. Rev. Lett.*, vol. 105, p. 245702, Dec 2010. 48, 53

[177] K. R. A. Hazzard and E. J. Mueller, "Techniques to measure quantum criticality in cold atoms," *Phys. Rev. A*, vol. 84, p. 013604, Jul 2011. 48, 53

[178] A. del Campo, A. Retzker, and M. B. Plenio, "The inhomogeneous Kibble-Zurek mechanism: vortex nucleation during Bose-Einstein condensation," *New Journal of Physics*, vol. 13, no. 8, p. 083022, 2011. 48

[179] A. del Campo, T. W. B. Kibble, and W. H. Zurek, "Causality and non-equilibrium second-order phase transitions in inhomogeneous systems," *Journal of Physics: Condensed Matter*, vol. 25, no. 40, p. 404210, 2013. 48

[180] V. Schweikhard, S. Tung, and E. A. Cornell, "Vortex proliferation in the Berezinskii-Kosterlitz-Thouless regime on a two-dimensional lattice of Bose-Einstein condensates," *Phys. Rev. Lett.*, vol. 99, p. 030401, Jul 2007. 50

[181] A. Sinatra, C. Lobo, and Y. Castin, "The truncated Wigner method for Bose-condensed gases: limits of validity and applications," *Journal of Physics B: Atomic, Molecular and Optical Physics*, vol. 35, no. 17, p. 3599, 2002. 50

[182] A. Polkovnikov, "Quantum corrections to the dynamics of interacting bosons: Beyond the truncated Wigner approximation," *Phys. Rev. A*, vol. 68, p. 053604, Nov 2003. 50

[183] P. Blakie, A. Bradley, M. Davis, R. Ballagh, and C. Gardiner, "Dynamics and statistical mechanics of ultra-cold Bose gases using c-field techniques," *Advances in Physics*, vol. 57, no. 5, pp. 363–455, 2008. 50

[184] A. Polkovnikov, "Phase space representation of quantum dynamics," *Annals of Physics*, vol. 325, no. 8, pp. 1790 – 1852, 2010. 50

[185] M. Tylutki, *Dynamics of a quantum phase transition in systems of cold atoms*. PhD thesis, Jagiellonian University, 2013. 50

[186] A. Polkovnikov, S. Sachdev, and S. M. Girvin, "Nonequilibrium Gross-Pitaevskii dynamics of boson lattice models," *Phys. Rev. A*, vol. 66, p. 053607, Nov 2002. 50

[187] J.-S. Bernier, G. Roux, and C. Kollath, "Slow quench dynamics of a one-dimensional Bose gas confined to an optical lattice," *Phys. Rev. Lett.*, vol. 106, p. 200601, May 2011. 51

[188] E. Altman and A. Auerbach, "Oscillating superfluidity of bosons in optical lattices," *Phys. Rev. Lett.*, vol. 89, p. 250404, Dec 2002. 52

[189] S. Fang, C.-M. Chung, P. N. Ma, P. Chen, and D.-W. Wang, "Quantum criticality from in situ density imaging," *Phys. Rev. A*, vol. 83, p. 031605, Mar 2011. 53

[190] N. Gemelke, X. Zhang, C.-L. Hung, and C. Chin, "In situ observation of incompressible Mott-insulating domains in ultracold atomic gases," *Nature*, vol. 460, no. 7258, pp. 995–998, 2009. 53

[191] W. S. Bakr, J. I. Gillen, A. Peng, S. Fölling, and M. Greiner, "A quantum gas microscope for detecting single atoms in a Hubbard-regime optical lattice," *Nature*, vol. 462, no. 7269, pp. 74–77, 2009. 53

[192] J. F. Sherson, C. Weitenberg, M. Endres, M. Cheneau, I. Bloch, and S. Kuhr, "Single-atom-resolved fluorescence imaging of an atomic Mott insulator," *Nature*, vol. 467, no. 7311, pp. 68–72, 2010. 53

[193] C. Weitenberg, M. Endres, J. F. Sherson, M. Cheneau, P. Schauß, T. Fukuhara, I. Bloch, and S. Kuhr, "Single-spin addressing in an atomic Mott insulator," *Nature*, vol. 471, no. 7338, pp. 319–324, 2011. 53

[194] B. Zimmermann, T. Müller, J. Meineke, T. Esslinger, and H. Moritz, "High-resolution imaging of ultracold fermions in microscopically tailored optical potentials," *New Journal of Physics*, vol. 13, no. 4, p. 043007, 2011. 53

[195] C.-L. Hung and C. Chin, "In situ imaging of atomic quantum gases," *arXiv:1312.0498*, 2013. 53

[196] M. Miranda, R. Inoue, Y. Okuyama, and M. Kozuma, "Site-resolved imaging of ytterbium atoms in a two-dimensional optical lattice," *arXiv:1410.5189*, 2014. 53

[197] L. W. Cheuk, M. A. Nichols, M. Okan, T. Gersdorf, V. V. Ramasesh, W. S. Bakr, T. Lompe, and M. W. Zwierlein, "A quantum gas microscope for fermionic atoms," *arXiv:1503.02648*, 2015. 53

[198] D. C. McKay and B. DeMarco, "Cooling in strongly correlated optical lattices: prospects and challenges," *Reports on Progress in Physics*, vol. 74, no. 5, p. 054401, 2011. 53, 71

[199] W. H. Zurek, "Decoherence, einselection, and the quantum origins of the classical," *Rev. Mod. Phys.*, vol. 75, pp. 715–775, May 2003. 54

[200] M. Schlosshauer, "Decoherence, the measurement problem, and interpretations of quantum mechanics," *Rev. Mod. Phys.*, vol. 76, pp. 1267–1305, Feb 2005. 54

[201] G. M. Palma, K.-A. Suominen, and A. K. Ekert, "Quantum computers and dissipation," *Proceedings of the Royal Society of London. Series A: Mathematical, Physical and Engineering Sciences*, vol. 452, no. 1946, pp. 567–584, 1996. 54

[202] S. Diehl, A. Micheli, A. Kantian, B. Kraus, H. Büchler, and P. Zoller, "Quantum states and phases in driven open quantum systems with cold atoms," *Nature Physics*, vol. 4, no. 11, pp. 878–883, 2008. 54, 70

[203] H. Weimer, M. Müller, I. Lesanovsky, P. Zoller, and H. P. Büchler, "A Rydberg quantum simulator," *Nature Physics*, vol. 6, no. 5, pp. 382–388, 2010. 54

[204] S. Diehl, E. Rico, M. A. Baranov, and P. Zoller, "Topology by dissipation in atomic quantum wires," *Nature Physics*, vol. 7, no. 12, pp. 971–977, 2011. 54

[205] H. Krauter, C. A. Muschik, K. Jensen, W. Wasilewski, J. M. Petersen, J. I. Cirac, and E. S. Polzik, "Entanglement generated by dissipation and steady state entanglement of two macroscopic objects," *Phys. Rev. Lett.*, vol. 107, p. 080503, Aug 2011. 54

[206] J. T. Barreiro, M. Müller, P. Schindler, D. Nigg, T. Monz, M. Chwalla, M. Hennrich, C. F. Roos, P. Zoller, and R. Blatt, "An open-system quantum simulator with trapped ions," *Nature*, vol. 470, no. 7335, pp. 486–491, 2011. 54

[207] G. Kordas, S. Wimberger, and D. Witthaut, "Dissipation-induced macroscopic entanglement in an open optical lattice," *Europhysics Letters (EPL)*, vol. 100, no. 3, p. 30007, 2012. 54

[208] K. Stannigel, P. Rabl, and P. Zoller, "Driven-dissipative preparation of entangled states in cascaded quantum-optical networks," *New Journal of Physics*, vol. 14, no. 6, p. 063014, 2012. 54

[209] M. Müller, S. Diehl, G. Pupillo, and P. Zoller, "Engineered open systems and quantum simulations with atoms and ions," in *Advances in Atomic, Molecular, and Optical Physics* (E. A. Paul Berman and C. Lin, eds.), vol. 61 of *Advances In Atomic, Molecular, and Optical Physics*, pp. 1 – 80, Academic Press, 2012. 54

[210] Y. Lin, J. Gaebler, F. Reiter, T. Tan, R. Bowler, A. Sørensen, D. Leibfried, and D. Wineland, "Dissipative production of a maximally entangled steady state of two quantum bits," *Nature*, vol. 504, no. 7480, pp. 415–418, 2013. 54

[211] J. C. Budich, P. Zoller, and S. Diehl, "Dissipative Chern Insulators," *ArXiv:1409.6341*, sep 2014. 54

[212] F. Verstraete, M. M. Wolf, and J. I. Cirac, "Quantum computation and quantum-state engineering driven by dissipation," *Nature Physics*, vol. 5, no. 9, pp. 633–636, 2009. 54

[213] N. Syassen, D. M. Bauer, M. Lettner, T. Volz, D. Dietze, J. J. García-Ripoll, J. I. Cirac, G. Rempe, and S. Dürr, "Strong dissipation inhibits losses and induces correlations in cold molecular gases," *Science*, vol. 320, no. 5881, pp. 1329–1331, 2008. 54, 70

[214] Z. Cai, U. Schollwöck, and L. Pollet, "Identifying a bath-induced Bose liquid in interacting spin-boson models," *Phys. Rev. Lett.*, vol. 113, p. 260403, Dec 2014. 54

[215] J. Catani, G. Barontini, G. Lamporesi, F. Rabatti, G. Thalhammer, F. Minardi, S. Stringari, and M. Inguscio, "Entropy exchange in a mixture of ultracold atoms," *Phys. Rev. Lett.*, vol. 103, p. 140401, Sep 2009. 54

[216] R. Scelle, T. Rentrop, A. Trautmann, T. Schuster, and M. K. Oberthaler, "Motional coherence of fermions immersed in a Bose gas," *Phys. Rev. Lett.*, vol. 111, p. 070401, Aug 2013. 54

[217] T. Pfau, S. Spälter, C. Kurtsiefer, C. R. Ekstrom, and J. Mlynek, "Loss of spatial coherence by a single spontaneous emission," *Phys. Rev. Lett.*, vol. 73, pp. 1223–1226, Aug 1994. 54

[218] M. Brune, E. Hagley, J. Dreyer, X. Maître, A. Maali, C. Wunderlich, J. M. Raimond, and S. Haroche, "Observing the progressive decoherence of the "meter" in a quantum measurement," *Phys. Rev. Lett.*, vol. 77, pp. 4887–4890, Dec 1996. 54

[219] C. J. Myatt, B. E. King, Q. A. Turchette, C. A. Sackett, D. Kielpinski, W. M. Itano, C. Monroe, and D. J. Wineland, "Decoherence of quantum superpositions through coupling to engineered reservoirs," *Nature*, vol. 403, no. 6767, pp. 269–273, 2000. 54

[220] M. Brune, F. Schmidt-Kaler, A. Maali, J. Dreyer, E. Hagley, J. M. Raimond, and S. Haroche, "Quantum Rabi oscillation: A direct test of field quantization in a cavity," *Phys. Rev. Lett.*, vol. 76, pp. 1800–1803, Mar 1996. 55

[221] D. Jaksch, C. Bruder, J. I. Cirac, C. W. Gardiner, and P. Zoller, "Cold bosonic atoms in optical lattices," *Phys. Rev. Lett.*, vol. 81, pp. 3108–3111, Oct 1998. 56, 72, 106

[222] D. C. McKay, C. Meldgin, D. Chen, and B. DeMarco, "Slow thermalization between a lattice and free Bose gas," *Phys. Rev. Lett.*, vol. 111, p. 063002, Aug 2013. 56, 59

[223] B. Gadway, D. Pertot, J. Reeves, M. Vogt, and D. Schneble, "Glassy behavior in a binary atomic mixture," *Phys. Rev. Lett.*, vol. 107, p. 145306, Sep 2011. 56

[224] J. Catani, G. Lamporesi, D. Naik, M. Gring, M. Inguscio, F. Minardi, A. Kantian, and T. Giamarchi, "Quantum dynamics of impurities in a one-dimensional Bose gas," *Phys. Rev. A*, vol. 85, p. 023623, Feb 2012. 56

[225] B. Gadway, D. Pertot, J. Reeves, and D. Schneble, "Probing an ultracold-atom crystal with matter waves," *Nature Physics*, vol. 8, no. 7, pp. 544–549, 2012. 56

[226] G. Lamporesi, J. Catani, G. Barontini, Y. Nishida, M. Inguscio, and F. Minardi, "Scattering in mixed dimensions with ultracold gases," *Phys. Rev. Lett.*, vol. 104, p. 153202, Apr 2010. 56

[227] B. Gadway, D. Pertot, R. Reimann, and D. Schneble, "Superfluidity of interacting bosonic mixtures in optical lattices," *Phys. Rev. Lett.*, vol. 105, p. 045303, Jul 2010. 56

[228] Y. Zhai, X. Yue, Y. Wu, X. Chen, P. Zhang, and X. Zhou, "Effective preparation and collisional decay of atomic condensates in excited bands of an optical lattice," *Phys. Rev. A*, vol. 87, p. 063638, Jun 2013. 58

[229] A. Moerdijk, H. Boesten, and B. Verhaar, "Decay of trapped ultracold alkali atoms by recombination," *Physical Review A*, vol. 53, no. 2, p. 916, 1996. 65

[230] O. Luiten, M. Reynolds, and J. Walraven, "Kinetic theory of the evaporative cooling of a trapped gas," *Phys. Rev. A*, vol. 53, pp. 381–389, Jan 1996. 65, 71, 83

[231] R. Cline, J. Miller, M. Matthews, and D. Heinzen, "Spin relaxation of optically trapped atoms by light scattering," *Optics letters*, vol. 19, no. 3, pp. 207–209, 1994. 65

[232] R. Ozeri, C. Langer, J. D. Jost, B. DeMarco, A. Ben-Kish, B. R. Blakestad, J. Britton, J. Chiaverini, W. M. Itano, D. B. Hume, D. Leibfried, T. Rosenband, P. O. Schmidt, and D. J. Wineland, "Hyperfine coherence in the presence of spontaneous photon scattering," *Phys. Rev. Lett.*, vol. 95, p. 030403, Jul 2005. 65

[233] E. Timmermans and R. Côté, "Superfluidity in sympathetic cooling with atomic Bose-Einstein condensates," *Phys. Rev. Lett.*, vol. 80, pp. 3419–3423, Apr 1998. 68

[234] F. Zambelli, L. Pitaevskii, D. M. Stamper-Kurn, and S. Stringari, "Dynamic structure factor and momentum distribution of a trapped Bose gas," *Phys. Rev. A*, vol. 61, p. 063608, May 2000. 68

[235] E. Jeckelmann, "Dynamical density-matrix renormalization-group method," *Phys. Rev. B*, vol. 66, p. 045114, Jul 2002. 69

[236] C. Chin, R. Grimm, P. Julienne, and E. Tiesinga, "Feshbach resonances in ultracold gases," *Rev. Mod. Phys.*, vol. 82, pp. 1225–1286, Apr 2010. 69

[237] J.-P. Martikainen, "Dynamical instability and loss of p-band bosons in optical lattices," *Phys. Rev. A*, vol. 83, p. 013610, Jan 2011. 70

[238] S. Paul and E. Tiesinga, "Formation and decay of Bose-Einstein condensates in an excited band of a double-well optical lattice," *Phys. Rev. A*, vol. 88, p. 033615, Sep 2013. 70

[239] A. Isacsson and S. M. Girvin, "Multiflavor bosonic Hubbard models in the first excited Bloch band of an optical lattice," *Phys. Rev. A*, vol. 72, p. 053604, Nov 2005. 70

[240] A. Collin, J. Larson, and J. P. Martikainen, "Quantum states of p-band bosons in optical lattices," *Phys. Rev. A*, vol. 81, p. 023605, Feb 2010. 70

[241] G. Wirth, M. Ölschläger, and A. Hemmerich, "Evidence for orbital superfluidity in the p-band of a bipartite optical square lattice," *Nature Physics*, vol. 7, no. 2, pp. 147–153, 2011. 70

[242] X. Li, E. Zhao, and W. V. Liu, "Effective action approach to the p-band Mott insulator and superfluid transition," *Phys. Rev. A*, vol. 83, p. 063626, Jun 2011. 70

[243] P. Soltan-Panahi, D.-S. Lühmann, J. Struck, P. Windpassinger, and K. Sengstock, "Quantum phase transition to unconventional multi-orbital superfluidity in optical lattices," *Nature Physics*, vol. 8, no. 1, pp. 71–75, 2012. 70

[244] E. Dagotto, "Correlated electrons in high-temperature superconductors," *Rev. Mod. Phys.*, vol. 66, pp. 763–840, Jul 1994. 71

[245] A. Griessner, A. J. Daley, S. R. Clark, D. Jaksch, and P. Zoller, "Dissipative dynamics of atomic Hubbard models coupled to a phonon bath: dark state cooling of atoms within a Bloch band of an optical lattice," *New Journal of Physics*, vol. 9, no. 2, p. 44, 2007. 71, 74

[246] M. Rigol, V. Dunjko, and M. Olshanii, "Thermalization and its mechanism for generic isolated quantum systems," *Nature*, vol. 452, no. 7189, pp. 854–858, 2008. 71, 91

[247] B. DeMarco, *Quantum Behavior of an Atomic Fermi Gas*. PhD thesis, University of Colorado, 2001. 80

[248] S. Koller, A. Groot, R. Duine, H. Stoff, and P. van der Straten, "Spin drag in a Bose gas," *arXiv:1204.6143*, 2012. 81

[249] O. Gunnarsson, M. Calandra, and J. E. Han, "*Colloquium*: Saturation of electrical resistivity," *Rev. Mod. Phys.*, vol. 75, pp. 1085–1099, Oct 2003. 82, 91

[250] M. Y. Kagan, *Modern trends in superconductivity and superfluidity*. Springer, 2013. 83

[251] C.-L. Hung, X. Zhang, N. Gemelke, and C. Chin, "Accelerating evaporative cooling of atoms into Bose-Einstein condensation in optical traps," *Phys. Rev. A*, vol. 78, p. 011604, Jul 2008. 87

[252] A. J. Olson, R. J. Niffenegger, and Y. P. Chen, "Optimizing the efficiency of evaporative cooling in optical dipole traps," *Phys. Rev. A*, vol. 87, p. 053613, May 2013. 87

[253] J. Gordon and A. Ashkin, "Motion of atoms in a radiation trap," *Phys. Rev. A*, vol. 21, pp. 1606–1617, May 1980. 87

[254] B. DeMarco, S. Papp, and D. Jin, "Pauli blocking of collisions in a quantum degenerate atomic Fermi gas," *Phys. Rev. Lett.*, vol. 86, pp. 5409–5412, Jun 2001. 89

[255] E. Timmermans, "Degenerate fermion gas heating by hole creation," *Phys. Rev. Lett.*, vol. 87, p. 240403, Nov 2001. 89

[256] T. Kinoshita, T. Wenger, and D. S. Weiss, "A quantum Newton's cradle," *Nature*, vol. 440, no. 7086, pp. 900–903, 2006. 91

[257] G. Carleo, F. Becca, M. Schiró, and M. Fabrizio, "Localization and glassy dynamics of many-body quantum systems," *Scientific reports*, vol. 2, 2012. 91

[258] W. Bao, D. Jaksch, and P. A. Markowich, "Numerical solution of the Gross-Pitaevskii equation for Bose-Einstein condensation," *Journal of Computational Physics*, vol. 187, no. 1, pp. 318 – 342, 2003. 94, 95

[259] G. Strang, "On the construction and comparison of difference schemes," *SIAM Journal on Numerical Analysis*, vol. 5, no. 3, pp. 506–517, 1968. 94

[260] C. Cohen-Tannoudji, J. Dupont-Roc, G. Grynberg, and P. Thickstun, *Atom-photon interactions: basic processes and applications*. Wiley Online Library, 1992. 97

[261] V. E. Lembessis and D. Ellinas, "Optical dipole trapping beyond the rotating wave approximation: the case of large detuning," *Journal of Optics B: Quantum and Semiclassical Optics*, vol. 7, no. 11, p. 319, 2005. 97

[262] U. Ray and D. M. Ceperley, "Revealing the condensate and noncondensate distributions in the inhomogeneous Bose-Hubbard model," *Phys. Rev. A*, vol. 87, p. 051603, May 2013. 98

[263] D. McKay, U. Ray, S. Natu, P. Russ, D. Ceperley, and B. DeMarco, "Metastable Bose-Einstein condensation in a strongly correlated optical lattice," *Phys. Rev. A*, vol. 91, p. 023625, Feb 2015. 98

[264] D. S. Rokhsar and B. G. Kotliar, "Gutzwiller projection for bosons," *Phys. Rev. B*, vol. 44, pp. 10328–10332, Nov 1991. 106

[265] K. Sheshadri, H. R. Krishnamurthy, R. Pandit, and T. V. Ramakrishnan, "Superfluid and insulating phases in an interacting-boson model: Mean-field theory and the RPA," *Europhysics Letters (EPL)*, vol. 22, no. 4, p. 257, 1993. 106

[266] O. Penrose and L. Onsager, "Bose-Einstein condensation and liquid helium," *Phys. Rev.*, vol. 104, pp. 576–584, Nov 1956. 106